A NEW GENERATION OF ZONAL MODELS: DEVELOPMENT, VERIFICATION AND APPLICATION

Teshome Edae Jiru

A Thesis

in

The department

of

Building, Civil and Environmental Engineering

Presented in Partial Fulfillment of the Requirements for the

Degree of Doctor of Philosophy (Building studies)

at

Concordia University

Montreal, Quebec, Canada

April 2006

© Teshome Edae Jiru, 2006

Library and Archives Canada

Published Heritage Branch

395 Wellington Street
Ottawa ON K1A 0N4
Canada

Bibliothèque et Archives Canada

Direction du Patrimoine de l'édition

395, rue Wellington
Ottawa ON K1A 0N4
Canada

Your file Votre référence
ISBN: 978-0-494-16281-1
Our file Notre référence
ISBN: 978-0-494-16281-1

NOTICE:
The author has granted a non-exclusive license allowing Library and Archives Canada to reproduce, publish, archive, preserve, conserve, communicate to the public by telecommunication or on the Internet, loan, distribute and sell theses worldwide, for commercial or non-commercial purposes, in microform, paper, electronic and/or any other formats.

The author retains copyright ownership and moral rights in this thesis. Neither the thesis nor substantial extracts from it may be printed or otherwise reproduced without the author's permission.

AVIS:
L'auteur a accordé une licence non exclusive permettant à la Bibliothèque et Archives Canada de reproduire, publier, archiver, sauvegarder, conserver, transmettre au public par télécommunication ou par l'Internet, prêter, distribuer et vendre des thèses partout dans le monde, à des fins commerciales ou autres, sur support microforme, papier, électronique et/ou autres formats.

L'auteur conserve la propriété du droit d'auteur et des droits moraux qui protège cette thèse. Ni la thèse ni des extraits substantiels de celle-ci ne doivent être imprimés ou autrement reproduits sans son autorisation.

In compliance with the Canadian Privacy Act some supporting forms may have been removed from this thesis.

While these forms may be included in the document page count, their removal does not represent any loss of content from the thesis.

Conformément à la loi canadienne sur la protection de la vie privée, quelques formulaires secondaires ont été enlevés de cette thèse.

Bien que ces formulaires aient inclus dans la pagination, il n'y aura aucun contenu manquant.

Canada

ABSTRACT

A New Generation of Zonal Models: Development, Verification and Application

Teshome Edae Jiru, Ph.D.
Concordia University, 2006

Zonal models are intermediate between CFD and single-zone models. They can generate results faster than CFD and more accurately than single-zone models. They provide global information on the distribution of airflow and temperature in a room and they have been used to predict moisture distribution, thermal comfort, contaminant distribution and personal exposure. The zonal models predict the airflow pattern reasonably well for natural convection since airflow is only due to buoyancy. For forced convection, they provide good prediction only in the specific zone, which indicates that the power-law model (PLM), used in the standard zone, is the main cause of the discrepancies of the zonal approach.

In this study, three methodologies were investigated for improving the prediction capability of the PLM. The first was investigation of the significance of the value of the flow coefficient (K). In this methodology, one K value was used for each cell in the standard zone. Values other than the commonly used value of $K = 0.83$ were considered. The result revealed that for forced convection, the value of K has no impact on the prediction of the PLM. The second method employed CFD generated data to estimate K

value for each cell. Two models were developed using this approach: PLM with variable K (PLMK) and PLM with variable K where K is a function of y/H ($PLMK_{func}$). The PLMK was found to provide better predictions than the $PLMK_{func}$ and the PLM. In the third methodology, the direct and indirect combinations of the PLM and the SDM were explored. The direct combination has provided different zonal models. The indirect combination has resulted in the modified power-law model (MPLM). The comparison of the predictions of the zonal models, for isothermal and non-isothermal room, with experimental data and CFD shows that the MPLM is superior to the other zonal models.

Additionally, zonal approach was applied for the prediction of the temporal and spatial temperature distribution in a mechanically ventilated DSF and good agreement with experimental data was obtained. Since the zonal approach provides global information faster than CFD, potential applications of the zonal approach include the prediction of temperature distribution and contaminant dispersion in whole building. This is very important for protecting building occupants form fire accidents, chemical/biological attacks by terrorists and from natural occurring diseases such as SARS and avian flu.

ACKNOWLEDGEMENTS

I would like to extend my sincere and heart-felt appreciation to my supervisor Dr. Fariborz Haghighat for his valuable comments, suggestions, advice, encouragement and guidance without which this thesis could not have been successful.

I cordially thank the supervisory committee for their valuable comment and suggestions. I would also like to extend my gratitude to Dr. E.Wurtz for the valuable discussions and suggestions; Dr. Marco Perino and his research group at Politecnico Di Torino for their hospitality during my stay in Torino and providing the experimental data for the ventilated double-skin facade; and my friends and students in our group for their unreserved cooperation.

For their love and understanding, my gratitude goes to my mother, Fantaye; my father, the late Edae; and my brothers and sisters, especially my late sister, Liyu. I am also thankful to my mother-in-law, Emebet; my father-in-law, the late Negash; and my sister and brother-in-laws for their love and understanding.

Above all I am always indebted to the love of my life, Roz, for her love, trust, friendship, understanding and perseverance.

TABLE OF CONTENTS

LIST OF FIGURES ..... **XI**

LIST OF TABLES ..... **XVII**

NOMENCLATURE ..... **XVIII**

1 INTRODUCTION **1**

1.1 Background **1**

1.2 Problem statement and objectives **4**

1.3 Organization of thesis **6**

2 LITERATURE REVIEW **8**

2.1 Single-zone and multi-zone models **9**

2.2 Computational fluid dynamics (CFD) **9**

2.2.1 Large eddy simulation (LES) 10

2.2.2 Reynolds-average Navier-Stokes (RANS) turbulence models 11

2.2.3 Discussions 13

2.3 Zonal models **13**

2.3.1 Non-pressure zonal models 15

2.3.2 Pressure zonal models 15

2.3.3 Integrated zonal models 16

2.3.4 Improvements of the zonal models 19

2.3.4.1 Sensitivity of airflow and temperature distribution to K 21

2.3.4.2 The surface-drag flow models (SDM) 21

2.3.4.3 The momentum-zonal model (MZM) 22

2.4 Discussions 23

2.5 Summary 24

3 THE ZONAL METHOD 27

3.1 The airflow equations 28

3.1.1 The standard flow zone 30

3.1.1.1 The power-law model (PLM) 30

3.1.1.2 The surface-drag flow models (SDM) 33

3.1.2 The specific flow zones 36

3.1.2.1 Air jets 36

3.1.2.2 Thermal plumes and boundary layers 37

3.1.3 Numerical solution of the airflow equations 38

3.2 The energy equations 39

3.3 Solution of the airflow and energy equations 43

3.4 Summary 46

4 MODEL DEVELOPMENT AND VERIFICATION 47

4.1 One flow coefficient for all cells 48

4.1.1 Case description 49

4.1.2 Results and discussions 49

4.1.3 Concluding remarks 50

4.2 Different flow coefficients for each cell 52

4.2.1 Case description 52

4.2.2 Verification of CFD predictions 54

4.2.3 Estimation of the flow coefficient 59

4.2.3.1 Discretization of the room and estimation of K 59

4.2.3.2 Results and discussions 60

4.2.3.3 Further on the variability of K_x and K_y 69

4.2.4 Concluding remarks on the flow coefficient 77

4.3 Combining the PLM and the SDM 78

4.3.1 The direct combination 79

4.3.1.1 Case description 81

4.3.1.2 Results and discussions 81

4.3.2 The indirect combination 83

4.4 Verification of the MPLM prediction for an isothermal room 89

4.4.1 Wall inlet 89

4.4.1.1 Influence of the surface-drag exponent, n_2 89

4.4.1.2 Influence of the power-law exponent, n_1 93

4.4.2 Ceiling inlet 94

4.5 Verification of the MPLM prediction for a non-isothermal room 97

4.5.1 Case description 98

4.5.2 Results and discussion 99

4.5.2.1 Air velocity distribution 99

4.5.2.2 Air temperature distribution 101

4.6 Summary 104

5 APPLICATION OF THE ZONAL MODELS FOR DOUBLE-SKIN FAÇADES 106

5.1 Case description 107

5.2 Model verification 110

5.3 Parametric study 114

5.3.1 Inlet airflow rate 115

5.3.2 Height 115

5.3.3 Shading device 115

5.4 Summary 117

6 CONCLUSIONS AND RECOMMENDATIONS 119

6.1 Concluding remarks 120

6.2 Recommendations for future works 122

APPENDIX A: DOUBLE-SKIN FAÇADES 124

A.1 Classification 124

A.2 A review of experimental and numerical studies on DSF 126

A.3 Problem statement and methodology 127

A.4 Thermal models for the DSF system 129

A.4.1 Conduction heat transfer 130

A.4.2 Radiation heat transfer 130

A.4.2.1 Solar radiation 130

A.4.2.2 Long wave radiation 132

A.4.3 Convective heat transfer in the cavities 135

A.4.3.1 The double pane 136

A.4.3.2 The ventilated cavities 137

A.4.3.3 Estimated heat transfer coefficients 140

A.5 Airflow and energy equations for venetian blinds 141

A.6 Solution of airflow and energy equations 142

REFERENCES 143

LIST OF FIGURES

Figure 1.1 Classification of airflow models (Griffith and Chen, 2003)..... 2

Figure 2.1 Zones in a room. Zone 1, 2, and 3 are mixed zones..... 14

Figure 2.2 Prediction of the flow field by zonal model. Jet model was used for specific zone and PLM for standard zone (Mora et al. 2003)..... 20

Figure 2.3 Flow field predicted by CFD using 40x40grids (Mora et al. 2003)..... 20

Figure 2.4 Airflow predicted by SDM. Jet model was used for specific zone and the SDM for standard zone (Mora et al. 2003)..... 22

Figure 3.1 Airflow through the boundaries of cell (i,j)..... 29

Figure 3.2 Airflow rate calculations at a vertical cell interface..... 32

Figure 3.3 The surface-drag momentum balance model (Axley, 2001)..... 33

Figure 3.4 Energy flow through the boundaries of a cell (i,j)..... 40

Figure 3.5 Summary of the solution procedure for zonal airflow and thermal models.... 45

Figure 4.1 Dimensions of the room used for comparing the velocity prediction of different *K* values (Nielsen, 1998)..... 49

Figure 4.2 Comparison of the PLM prediction for the selected *K* values at x = 1m..... 51

Figure 4.3 Comparison of the PLM prediction for the selected *K* values at x = 3m..... 51

Figure 4.4 Case II: Grille diffuser, and outlet at the bottom of one of the walls..... 53

Figure 4.5 Case III: Ceiling diffuser and outlet at the bottom of one of the walls..... 53

Figure 4.6 Flow pattern predicted by CFD for *Re* = 2210, Case I..... 55

Figure 4.7 Flow pattern predicted by CFD for Re = 2210, Case II. 55

Figure 4.8 Flow pattern predicted by CFD for Re = 2210, Case III. 56

Figure 4.9 CFD flow field prediction using indoor zero-equation turbulence model and 20x18 grids (Chen and Xu, 1998). 57

Figure 4.10 CFD flow field prediction using k-ε turbulence model and 50x45 grids (Chen and Xu, 1998). 57

Figure 4.11 Comparison of CFD prediction with experimental data at x = 1m, Case I. .. 58

Figure 4.12 Comparison of CFD prediction with experimental data at x = 3m, Case I. .. 58

Figure 4.13 Division of the room into 11x11 cells for the estimation of K_x and K_y, Case I. 60

Figure 4.14 Estimation of K_x and K_y for cell j. 60

Figure 4.15 Distribution of K_x for slot inlet at ten vertical positions (VP), Case I. 62

Figure 4.16 Distribution of K_y for slot inlet at eleven vertical positions (VP), Case I. 62

Figure 4.17 Distribution of K_x for grille inlet at eight vertical positions (VP), Case II. ... 63

Figure 4.18 Distribution of K_y for grille inlet, at nine vertical positions (VP), Case II. ... 63

Figure 4.19 Distribution of K_x for ceiling diffuser at ten vertical positions (VP), Case III. 64

Figure 4.20 Distribution of K_y for Ceiling diffuser at eleven vertical positions (VP), Case III. 64

Figure 4.21 Distribution of average K_x for slot inlet, Case I. 66

Figure 4.22 Distribution of average K_y for slot inlet, Case I. 66

Figure 4.23 Distribution of average K_x for grille diffuser, Case II. 67

Figure 4.24 Distribution of average K_y for grille diffuser, Case II. 68

Figure 4.25 Distribution of average K_x for ceiling diffuser; Case III. 68

Figure 4.26 Distribution of average K_y for ceiling diffuser, Case III. 69

Figure 4.27 Division of the room into 6x11 cells for the estimation of K_x and K_y, Case I. 71

Figure 4.28 Distribution of K_x for slot inlet, Case I. 71

Figure 4.29 Distribution of K_y for slot inlet, Case I. 72

Figure 4.30 Average K_x for slot inlet, Case I. 72

Figure 4.31 Average K_y for slot inlet, Case I. 73

Figure 4.32 Comparison of velocity profiles predicted by PLMK, PLM and $PLMK_{func}$ at x = 1m, Case I. 75

Figure 4.33 Comparison of velocity profiles predicted by PLMK, PLM and $PLMK_{func}$ at 76

Figure 4.34 Airflow pattern predicted by the PLM, Case I. 76

Figure 4.35 Airflow pattern predicted by the PLMK, Case I. 77

Figure 4.36 Airflow pattern predicted by the $PLMK_{func}$, Case I. 77

Figure 4.37 Comparison of the zonal models predictions with experiment at x = 1m. 82

Figure 4.38 Comparison of the zonal models predictions with experiment at x = 3m. 83

Figure 4.39 Velocity profile for combined Couette-Poiseuille flow between parallel plates (White, 1990). 84

Figure 4.40 Velocity profile for the second term in Equation 4.8. U_x calculated by Equation 3.21. 87

Figure 4.41 Velocity profile for the second term in Equation 4.8. $U_x = U_0$ 87

Figure 4.42 Airflow pattern predicted by MPLM using the profile in Figure 4.40, Case I. 88

Figure 4.43 Airflow pattern predicted by MPLM using the profile in Figure 4.41, $n_1 = 0.5$ and $n_2 = 2$, Case I. 89

Figure 4.44 Comparison of the MPLM predictions for different values of n_2 with measured data and the PLMK at x = 1m. 90

Figure 4.45 Comparison of the MPLM predictions for different values of n_2 with measured data and the PLMK at x = 3m. 91

Figure 4.46 Airflow pattern predicted by MPLM for $n_1 = 0.5$ and $n_2 = 1/7$, Case I. 92

Figure 4.47 Airflow pattern predicted by MPLM for $n_1 = 0.5$ and $n_2 = 0.5$, Case I. 92

Figure 4.48 Airflow pattern predicted by MPLM for $n_1 = 0.5$ and $n_2 = 1$, Case I. 92

Figure 4.49 Comparison of the MPLM predictions for different values of n_1 and n_2 with measured data at x = 1m. 93

Figure 4.50 Comparison of the MPLM predictions for different values of n_1 and n_2 with measured data at x = 3m. 94

Figure 4.51 Plan view of the test room (Nielsen, 1998). 95

Figure 4.52 Comparison of the MPLM predictions with measure data at x = 1m. 96

Figure 4.53 Comparison of the MPLM predictions with measured data at x = 3m. 96

Figure 4.54 Airflow pattern predicted by the MPLM for 15x3x5 cells. 97

Figure 4.55 Airflow pattern predicted by the MPLM for 15x3x10 cells. 97

Figure 4.56 Geometry of test room (Zhang et al. 1992; Zhao, 2000). 98

Figure 4.57 Airflow pattern measured using PIV technique (Zhao, 2000). 100

Figure 4.58 Airflow pattern predicted by the MPLM. 100

Figure 4.59 Airflow pattern predicted by the PLM. 101

Figure 4.60 Comparison of measured and predicted air velocity at H=1.7m. 101

Figure 4.61 Measured temperature distribution (Zhao, 2000) 103

Figure 4.62 Temperature distribution predicted by the MPLM. 103

Figure 4.63 Temperature distribution predicted by the PLM. 103

Figure 5.1 Mechanically ventilated DSF. L1 is the exterior glass of the double pane; L2 is the interior glass of the double-pane; L3 is the venetian blinds; L4 is the interior glass of the ventilated DSF; Ca1 is the outer cavity; and Ca2 is the inner cavity, T_o is the air temperature at the inlet, T_{ex} is the air temperature at the exit, T_{indoor} is the room air temperature, $T_{outdoor}$ the outside air temperature, q_{sol} is the total solar radiation, q_{trans} is the transmitted solar radiation, ● is thermocouple and ◖ is pyranometer.....108

Figure 5.2 Measured inlet and boundary conditions. 109

Figure 5.3 Comparison of predicted and measured temperature of the air in Ca1 at positions 1, 2, and 3. 112

Figure 5.4 Comparison of predicted and measured temperature of the air in Ca2 at positions 1, 2, and 3. 112

Figure 5.5 Comparison of predicted and measured temperature of the venetian blind at positions 1, 2, and 3. 113

Figure 5.6 Comparison of predicted and measured temperature of inner glass at positions 1, 2, and 3. 113

Figure 5.7 Comparison of predicted and measured temperature of exhaust air. 114

Figure 5.8 Sensitivity of T_{ex}–T_{in} to M_0. 116

Figure 5.9 Sensitivity of T_{ex}–T_{in} to H. 116

Figure 5.10 Sensitivity of $T_{ex} - T_{in}$ to venetian blinds. 117

Figure A.1 Components of ventilated double-glass façade (a) mechanical ventilation (b) natural ventilation. (1) air outlet, (2) interior pane, (3) air inlet (4) air cavity, (5) shading device and (6) outer pane.....125

Figure A.2 Fictitious cavity for calculating the view factors for the layers of a DSF. ... 134

LIST OF TABLES

Table 2.1 Applications of the zonal models 17

Table 4.1 Values of coefficients for Equation 4.3, Case I. 74

Table 4.2 Values of coefficients in Equations 4.4 and 4.5. 80

Table A.1 Average Nusselt number for the outer double pane cavity. 137

Table A.2 Average Nusselt number correlations used for mechanically ventilated cavities (Bejan, 1995) 139

NOMENCLATURE

a, b, c	Coefficients;
A	Area, m^2;
A_{ratio}	Aspect ratio of ventilated cavity;
Ar_0	Archimedes number;
B_j	Element of column vector;
C	Proportionality constant of air jet; dimensionless pressure;
c_p	Specific heat capacity of air, J/Kg.K;
$Ca1, Ca2$	Outer and inner cavities of double skin façade;
D_h	Hydraulic diameter, m;
F	View factor;
g	Gravitational acceleration, m/s^2;
Gr	Grashof number;
h_0	Width of inlet, m;
h	Average heat transfer coefficient, W/m^2K;
H	Room/ cavity height, m;
$J_{i,j}$	Element of Jacobian matrix;
J	Jacobean;
k	Thermal conductivity, W/m.K;
K	Flow coefficient;

l	Width of sub-zone or cells, m;
l_{ch}	Characteristic length, m;
L_P	Air jet penetration length, m;
$L1, L2, L3, L4$	Layers of double-skin façade;
$m_{i,j}$	Mass flow rate, kg/s;
M_o	Inlet mass flow rate, kg/s;
M_x	Airflow rate in the specific zone, kg/s;
N	Number of faces/boundaries of a cell;
Nu	Nusselt number;
n_s	Cell number starting from the nearest cell to the surface
n_1	Power-law exponent;
n_2	Surface-drag exponent;
p	Permeability of the venetian blinds; perimeter of inlet, m;
$P_{i,j}$	Pressure, Pa;
Pr	Prandtl number;
q	Heat flux, W/m^2;
R	Gas constant, J/kg.K;
Ra	Rayleigh number;
Re	Reynolds number;
S	Sum of source/sink in the cell, kg/s;
T,t	Temperature, K;
U	Room air velocity $= (u^2 + v^2 + w^2)^{1/2}$, m/s;
U_0	Average velocity at the inlet, m/s;

U_x	Velocity of air in the specific zone, m/s;
u, v, w	Velocities in the x, y and z directions, m/s;
W	Width of the cavity or room, m;
x	Distance in the horizontal direction, m;
y	Vertical distance in the vertical direction, m;
Y	Characteristic room dimension, m;
Y_{neut}	Height of the neutral plane, m;

Subscripts

a	Air;
b	Bottom;
conv	Convection;
cond	Conduction;
conv-rad	Convection and radiation;
Dh	Hydraulic diameter;
E	East;
eq	Equivalent;
f	Flow;
H	Height;
in	Into the cell;
i,j	Coordinate of cell;
indoor	Indoor/room;
Li	Double skin façade layer;

max	Maximum;
m	Average;
M	Mass;
mech	Forced convection;
nat	Natural convection;
n	Previous iteration step;
n+1	Current iteration step;
N	North;
o	Inlet;
out	Out of the cell;
p	Reference cell;
rad	Radiation;
ref	Reference;
Surf	Surface;
sol	Solar radiation;
sol,D	Direct solar radiation;
sol,d	Diffused solar radiation;
sol,r	Reflected solar radiation;
S	South;
Th	Thermal;
outdoor	Surrounding air;
W	West;
x	Horizontal direction;

y	Vertical direction;

Greek symbols

α	Absorptance; thermal diffusivity, m^2/s;
β	Solar altitude; under-relaxation factor; thermal expansion coefficient, 1/K;
Δ	Difference;
ε	Emissivity;
θ	Incidence angle;
κ	Von Karman constant;
λ	Surface-drag flow coefficient;
μ	Dynamic viscosity, kg/m.s;
μ_e	Eddy viscosity of air, kg/m.s;
ν	Kinematic viscosity, m^2/s;
ρ	Density, kg/m^2;
τ_{xy}	Shear stress, Pa;
φ	Angle the venetian blinds make with the horizontal;
σ	Stefan-Boltzman constant,$W/m^2.K^4$;
Σ	Sum.

Other symbols

$\rightarrow$	Vector;
$\Rightarrow$	Matrix.

1 INTRODUCTION

1.1 Background

Airflow rate, temperature, relative humidity and concentration of pollutants are physical parameters that can affect occupants' perceptions of indoor air quality (IAQ) and thermal comfort. Therefore, to design, operate and maintain ventilation systems for acceptable IAQ and thermal comfort, detailed information regarding these parameters is required. Such information could be acquired through experiment and numerical simulation.

Experimental approaches provide reliable information regarding the above-mentioned parameters. They require measurement of temperature, velocity and contaminant concentration at least at some important locations. Field experiments are not suitable for parametric studies since these factors cannot easily be varied without affecting the activity of occupants. Full-scale laboratory experiments can be designed to control parameters such as ventilation rate and boundary conditions but they are often costly. Scale models can be used to replicate the significant characteristics of real room at less cost. However, all scaling criteria cannot be satisfied simultaneously (Awbi, 2003).

The advantages of numerical modeling and simulation, in addition to saving cost and time, are the ease of manipulating the desired parameters to investigate various possible scenarios and the provision of detailed information. Since the indoor airflow distribution

affects the distribution of contaminants, moisture and temperature, modeling of airflow is particularly important. Apparently, some degrees of simplifications are required in order to obtain airflow models, which can provide reasonable fidelity but at a lower cost of computing resources and time. Thus, depending on the details of information required, models commonly used for predicting and assessing indoor airflow can be developed using integral (macro) or differential (micro) approaches. The integral approach can lead to the development of simplified models such as single-zone, multi-zone and zonal models. The differential approach is commonly referred to as computational fluid dynamics (CFD). Figure 1.1 illustrates the difference between the single-zone, multi-zone, zonal and CFD models.

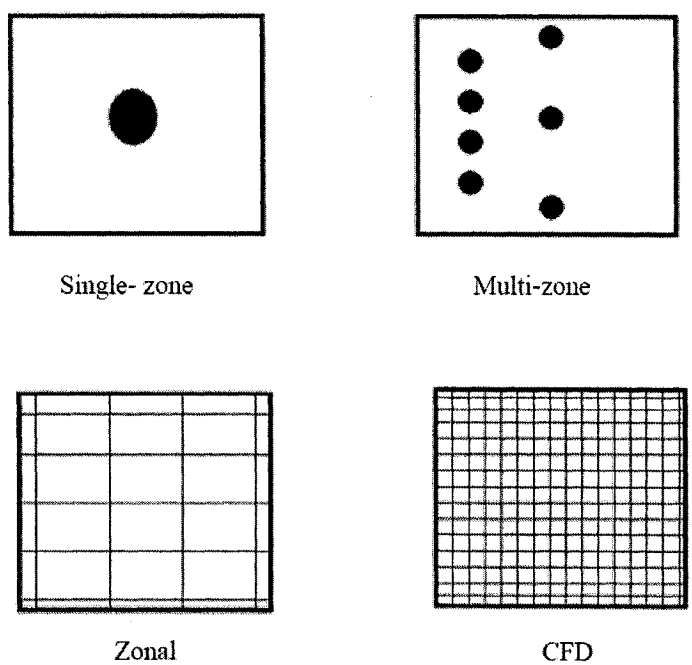

Figure 1.1 Classification of airflow models (Griffith and Chen, 2003).

Single- and multi-zone models are models for predicting air infiltration rates, airflow and contaminant transport. Single-zone models assume that a single, well-mixed zone can describe a building. Multi-zone models are suitable for buildings containing more than one well-mixed zone. Single- and multi-zone models use a network approach and the flow paths are described by relating mass flow with pressure difference using the power law function (Feustel and Dieris, 1992).

In CFD, a set of non-linear partial differential equations, which express the conservation of mass, momentum and energy are used. CFD models have been widely used in the analysis of indoor airflow, temperature, and contaminant distribution (Haghighat et al. 1992). These models have been validated for different flow conditions and geometry (Topp, 1999; Chen and Xu, 1998; Nielsen, 1998). A validated CFD model can provide data, which is difficult to obtain experimentally. For example, it could be difficult to measure the pressure difference between two points in a room experimentally since the difference is very small. Additionally, validated CFD models could be used to calibrate and develop simpler models.

Zonal models are intermediate airflow models between the extremes of single-zone and CFD. They can provide global information on the distribution of airflow and temperature in a room faster than CFD and more accurately than single-zone models. In the zonal approach, a room is divided into a specific and a standard flow zone. Each zone is further divided into a number of sub-zones or cells. The specific flow zones are air jet, plume, heater and boundary layer zones. The standard flow zone is the zone outside of the

specific zones including the occupied region. The airflow in the standard and specific zones has distinct characteristic. Consequently, different zonal models have been used to calculate the airflow rate in each zone. The airflow models used in specific flow zone and standard flow zone are referred to as non-pressure (empirical) and pressure (power-law) zonal models, respectively.

The zonal models have been applied to predict moisture distribution (Mendoca et al. 2002); thermal comfort (Haghighat et al. 2001; Voeltzel et al. 2001); contaminant distribution (Huang, 2003; Stewart and Ren, 2003); and personal exposure (Ren and Stewart, 2005). They have also been integrated with COMIS (COwZ) (Ren, 2002; Stewart and Ren, 2005).

1.2 Problem statement and objectives

The zonal models predict the airflow pattern reasonably well for natural convection (Wurtz et al. 1999a; Haghighat et al. 2001). This is because the airflow in natural convection results mainly due density difference. The airflow rate in the specific zone is well predicted for forced convection since empirical relations are used. But the zonal models have shown pronounced discrepancies in predicting the recirculation in the standard zone for forced convection (Haghighat et al. 2001; Mora et al. 2003). Since the power-law model (PLM) is applied in the standard zone, it is considered as the main cause of the discrepancies of the zonal models.

Some attempts have been made to improve the prediction capability of the zonal models in the standard zone. Wurtz et al. (1999a) investigated the effect of using different values of the flow coefficient (K) on the prediction of the airflow rate and temperature distribution for natural convection. They showed that varying the value of K changes the airflow rate and temperature at some locations in the room. The second improvement was the development of the surface-drag flow model (SDM) by Axley (2001). Mora et al. (2003) showed that the SDM could not make any significant improvement in the prediction of the recirculation compared to the PLM. Griffith and Chen (2003) employed the micro-approach to develop the other alternative model, the momentum-zonal model (MZM). Like the PLM, the MZM is based on the Euler equation. The PLM is the integral (macro) form of the Euler equation but the MZM is three-dimensional Euler equation and it does not categorize the room into a standard flow and a specific flow zone. The MZM gives good prediction of the temperature stratification in buoyancy-dominated flows such as natural convection, displacement ventilation and convective heating.

In summary, changing the value of K for natural convection changes the airflow rate at some location in the room. But the significance of using the same value of K for all cells and different values of K for each cell has not been investigated for forced convection. For forced convection, independent application of the PLM and the SDM has resulted in discrepancy of the airflow rate prediction. Nevertheless, no attempt was made to combine or modify these models to improve their prediction capability. Moreover, the approach pursued to obtain the MZM was micro but the macro approach is proposed in this research so as to apply the categorization employed in the zonal approach and

concentrate on improving the zonal models in the zone where discrepancy occurs. This approach makes the future integration of the new zonal models and their application in simulation codes such as COwZ possible. The integration of the improved zonal models will increase the accuracy of COwZ prediction of airflow, temperature, and contaminant dispersion in a building and its surroundings. This is very important for protecting building occupants form fire accident, chemical/biological attacks by terrorists and natural occurring diseases such as SARS and avian flu, and to study the effect of urban heat island on heating and cooling load of a building.

Therefore, the main objective of this research was to improve the prediction capability of the PLM in the standard zone using new methodologies such as investigation of the use of the same K in the standard zone, estimation of K in the standard zone using CFD generated data, and combination of the PLM and the SDM. Furthermore, the zonal approach was applied for predicting the temperature distribution of a mechanically ventilated DSF with venetian blinds.

1.3 Organization of thesis

Chapter 2 presents a review of the single-zone, multi-zone, CFD, and zonal models. It also includes the research methodologies and related discussions.

In Chapter 3, the formulations of the airflow models used in the standard zone, in the specific zones, and the energy equations are discussed. The Newton-Raphson non-linear

equation solver and the Tri-Diagonal Solution Algorithm (TDMA) used for solving the airflow and thermal models are also presented.

Chapter 4 provides the details of the methodologies for developing new zonal models and their verification. The proposed methodologies include use of the same flow coefficient in the standard zone, estimation of the flow coefficient in the standard zone using CFD and developing parametric equation for the flow coefficient, and combination of the PLM and the SDM using the direct and the indirect approach. For each case, the newly developed models are compared with the existing zonal models and experimental data.

Chapter 5 addresses the verification and application of the zonal models for a mechanically ventilated DSF equipped with venetian blinds. The details of the classification and modeling of a DSF is compiled in Appendix A.

Finally, Chapter 6 outlines the concluding remarks of this research and establishes recommendations for future work.

2 LITERATURE REVIEW

Experimental approaches and numerical models are commonly used to characterize the airflow and temperature distribution in a room. Experimental approaches provide reliable information regarding indoor airflow distribution. Different techniques such as flow visualization and particle imaging velocimetry (PIV) have been used to measure airflow (Zhang, 2004). However, it is difficult to apply experimental approach for every case envisaged. In this regard, various numerical models have been developed to study indoor air and thermal flow. The integral (macro) and differential (micro) are the two approaches for mechanistic modeling of room air and thermal flow. The integral approach can lead to the development of simple models such as single-zone, multi-zone, and zonal models. The differential approach is commonly referred to as computational fluid dynamics (CFD).

This chapter presents a literature review on airflow modeling in Sections 2.1 - 2.3 and a discussion of the proposed methodologies for this study in Section 2.4. Finally, the findings of the literature review and proposed methodologies are summarized in Section 2.5.

2.1 Single-zone and multi-zone models

Single- and multi-zone models are simplified models for predicting air infiltration rates, airflow and contaminant transport. Single-zone models assume that a single, well-mixed zone can describe a building. Consequently, they can only be expected to be suitable for a house and a small building. Multi-zone models are applied for buildings containing more than one well-mixed zone such as large and high-rise buildings. The single- and multi-zone models use a network approach in which flow paths interconnect nodes representing zones of different pressure, temperature and contaminant concentration (Haghighat, 1989). The flow paths are described by the power-law, which relates mass flow rate with pressure difference (Feustel and Dieris, 1992). The two well-known multi-zone codes that are typically used in practice are COMIS (Feustel and Smith, 1997) and CONTAM (Dols and Walton, 2002).

The importance of the single-zone and multi-zone models in this study is their similarity with the power-law zonal model (PLM). This will be used to explain the main causes of discrepancies of the PLM such as the hydrostatic flow field assumption, the model's one-dimensional nature, and its use of a constant flow coefficient.

2.2 Computational fluid dynamics (CFD)

Computational fluid dynamics (CFD) refers to the analysis of processes involving fluid flow, heat transfer and associated phenomena such as chemical reactions by means of a computer-based simulation (Versteeg and Malalasekera, 1995). The governing equations employed to model the transport phenomena are derived from the fundamental laws of

mass, momentum, and energy conservation. The resulting equations, Navier-Stokes and continuity, are coupled nonlinear partial differential equations and can only be solved numerically for most practical problems. Direct numerical simulation (DNS) is the most accurate way of modeling fluid flow numerically. It solves the governing equations for the full range of turbulent flow. This approach yields the complete spatial and temporal state of turbulent flow. Due to the fine grids involved, the most important problem associated with this technique is the requirement of computer resources such as speed and memory.

For indoor airflow and ventilation applications, less costly approaches are commonly used. These approaches model the turbulence fluctuations without directly simulating the small-scale fluctuations (like DNS would do). The two currently available approaches for turbulence modeling are large eddy simulation (LES) and Reynolds-average Navier-Stokes (RANS). These turbulence models are included in general application CFD softwares like CFX and FLUENT. Moreover, due to the increasing application of CFD for indoor airflow analysis, more specialized commercial CFD softwares like FLOVENT, AirPak, and VORTEX have been developed.

2.2.1 Large eddy simulation (LES)

In LES, the small-scale eddies are removed from the turbulent flow via filtering, and only the large-scale eddies are fully resolved. LES has made it possible to obtain a practical number of computational cells in the numerical simulation by filtering with respect to space and modeling the effect of the small-scale eddies on the turbulent flow field. LES

can address a transient solution to the Navier-Stokes equations. Jiang and Chen (2001), Jiang and Chen (2002) and Jiang et al. (2004) employed LES for the analysis of natural ventilation. Hanqing et al. (2005) used LES to predict the distribution of indoor airflow and thermal comfort indices. Tian et al. (2005) have also applied LES to model particle dispersion in a room.

2.2.2 Reynolds-average Navier-Stokes (RANS) turbulence models

RANS turbulence models are the most commonly used turbulence models for indoor airflow application. RANS equations are the result of the time averaging of the governing equations. This operation will throw away all details concerning the state of the flow contained in the instantaneous fluctuations (Versteeg and Malalasekera, 1995). Additional unknowns are introduced where all the influences from turbulent fluctuations are contained. These are called Reynolds stresses in the time averaged momentum equations, and Reynolds fluxes in the time averaged scalar transport equations. Hence, the main aim of turbulence modeling is to predict the effect of these Reynolds stresses and fluxes on the mean flow. Towards that end, empirical relations have been introduced to evaluate the turbulence terms and to bring closure to the system of equations.

A number of models are available, which range from closure models based on the eddy viscosity concept to the full second moment closure models (Tennehill et al. 1997). The zero, one and two-equation models are based on the eddy viscosity concept while the Reynolds stress model (RSM) is based on the second moment closure models.

Zero-equation turbulence models are the simplest turbulence models. Chen and Xu (1998) developed a zero-equation turbulence model for indoor airflow simulation. There are different variants of two-equation turbulence models: standard k-ε, low Reynolds number (LRN) k-ε, renormalization group (RNG) k-ε, and realizable k-ε. The standard k-ε model is the most widely used turbulence model for the prediction of room airflow. Xue and Shu (1998) employed the k-ε model to predict temperature, velocity and turbulence kinetic energy in an air-conditioned room. Huo et al. (2000) also used the standard k-ε model for developing model for air terminal device. Since the standard k-ε model is valid only for fully developed turbulent flows, in cases like pollutant emission from surfaces where the influence of local airflow is important, the LRN k-ε is employed. Zhang and Haghighat (1997), Topp (1999) and Topp et al. (2001) have applied the LRN k-ε model to study emission from solid building materials. Djunaedy and Cheong (2002) developed a diffuser modeling technique that uses the RNG k-ε model. Of all the k-ε models, the realizable k-ε model provides the best performance for separated flows and flows with complex secondary flow (Zhang, 2004).

In the case of the RSM, equations for Reynolds stresses are derived from Reynolds averaging and various assumptions are made to relate these Reynolds stresses. Such models account for the effect of anisotropy, which is particularly important for streamline curvature, rotation and rapid changes in strain rate. Due to the additional equations, the RSM requires more computing effort compared to all other versions of the k-ε model. Chen (1996) used the RSM to study the flow pattern of natural, forced and mixed convection in a room and an impinging jet flow. Clifford et al. (1997) applied the RSM

for a naturally ventilated building. Nielsen (2004) showed that the k-ε model is an acceptable model in many cases of indoor airflow, but the three-dimensional wall jet behavior can be predicted with a higher accuracy using the RSM.

2.2.3 Discussions

CFD provides a wealth of information pertaining to the distribution of parameters such as temperature, airflow, contaminant distribution. Furthermore, a validated CFD model can be used to develop and calibrate simpler models and to provide additional data, which is difficult to obtain experimentally. For example, it is difficult to measure the pressure difference between two points in a room experimentally since the difference is very small. Hence, the purpose of applying CFD in this study is to generate data for the estimation of the flow coefficient (K) and vector plots for qualitative comparison of the predictions of the zonal models.

2.3 Zonal models

Zonal models are intermediate models between single-zone and CFD. They provide information on airflow, temperature, and contaminant distribution in a room faster than CFD and more accurately and in more detail than single-zone models. The basic idea of zonal approach is to divide a flow field into a number of zones with distinct flow characteristics. These zones are categorized as either a specific or a standard flow zone. The specific flow zones include jets, plumes, and boundary layer zones. A jet is created due to the air supplied by diffusers. Thermal plumes are created above hot surfaces, heaters and occupants. A thermal boundary layer develops on a wall when there is

temperature difference between the wall and the local room air. The standard flow zone includes the regions outside of the specific zones such as the occupied region. As shown in Figure 2.1, the standard zone represents a large region of relatively weak airflow and a specific flow zone represents zones with a driving airflow. For the implementation of the zonal method, each zone is subdivided into cells or sub-zones, which are usually larger than the grids normally used in CFD applications. The zones that have the characteristics of the standard and the nearby specific zone are called mixed zones. Zones 1 - 3 in Figure 2.1 are mixed zones.

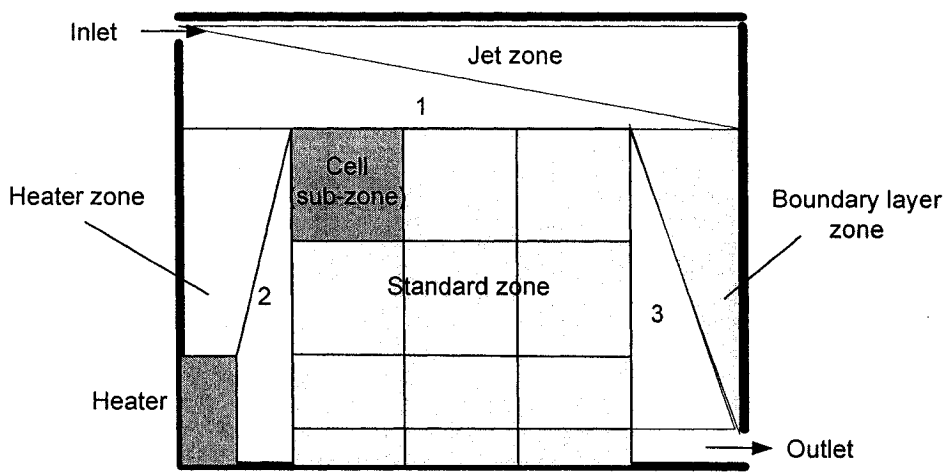

Figure 2.1 Zones in a room. Zone 1, 2, and 3 are mixed zones.

The distinct character of each airflow zone has made it necessary to use different models to describe the air and thermal flow in each zone. Non-pressure, pressure, and integration of pressure and non-pressure models have been used to describe room air and thermal flow (Teshome and Haghighat, 2004). Three generations of zonal models have evolved

over the years, which have employed the non-pressure, the pressure, and integration of the pressure and the non-pressure models (Megri et al. 2005).

2.3.1 Non-pressure zonal models

The non-pressure zonal models were applied in the first-generation zonal models. They were mostly employed to model the temperature stratification in a room. Empirical equations were used to describe thermal plumes, jets and boundary layers.

Different authors have applied the non-pressure zonal models with varying degree of detail. Howarth (1980), Heine and Mogens (1990), Inard and During (1994), Manzoni and Rongere (1996), and Shilkrot and Zhivov (1996) applied steady state non-pressure models to predict the temperature stratification in a room. Togari el al. (1993) and Gschwind et al (1996) integrated one-dimensional conduction through surfaces in the non-pressure approach. Inard et al. (1997) also employed non-pressure model to study energy consumption and thermal comfort in rooms.

2.3.2 Pressure zonal models

The pressure zonal models are the second-generation zonal models. Their application is limited to the standard zone, a zone in which the air velocity is relatively low. The power-law model (PLM) has been used to relate the airflow rate between cells with the corresponding pressure difference (Inard et al. 1996a; Inard et al. 1996b; Cocora, 1996). The PLM can be given as:

$$m_{i,j} = KA\rho\left(\frac{2\Delta P_{i,j}}{\rho}\right)^{1/2} \tag{2.1}$$

where

$m_{i,j}$ is the mass flow rate, kg/s;

A is the area of a cell, m^2;

ρ is the density of air, kg/m^3;

$\Delta P_{i,j}$ is the pressure difference, Pa;

K is the flow coefficient (usually assigned a constant value of 0.83).

Inard et al. (1996a) and Musy et al. (2002) have shown the limitations of the pressure zonal models for predicting airflow in specific zones.

2.3.3 Integrated zonal models

The integrated zonal models are the third-generation models that use the pressure zonal models for standard zones and the non-pressure models for the specific zones. These models have been implemented for the prediction of indoor airflow, temperature, and contaminant distribution. Table 2.1 presents the summary of the applications of the integrated zonal models.

Table 2.1 Applications of the zonal models.

Integrated specific flow model	Cases considered	References
Wall non-isothermal jet Wall thermal plume Thermal boundary layer	Three-dimensional natural and mixed convection. Simulations results were compared with experiment data and CFD.	Inard et al. (1996a)
Wall non-isothermal jet Wall thermal plume Thermal boundary layer	Three-dimensional natural and mixed convection. Simulation results were compared with CFD and experimental data.	Inard et al. (1996b)
No specific flow model	Two- and three-dimensional natural convection. Simulation results were compared with CFD and experimental data.	Wurtz et al. (1999a)
Wall non-isothermal jet Wall thermal plume Thermal boundary layer	Three-dimensional natural and forced convection. Simulation results were compared with experimental data. Further, the model was applied to four-room building.	Wurtz et al. (1999b)
No specific flow model	Coupled zonal model with an envelope module to calculate conductive and radiative heat transfer in the building.	Voeltzel et al. (2001)
Wall isothermal jet	Three-dimensional natural and mixed convection. Integrated with thermal comfort model. Simulation results were compared with CFD and experimental data.	Haghighat et al. (2001)
Wall thermal plume	Three-dimensional natural convection. Simulation results were compared with experimental data.	Musy et al. (2001)
Isothermal free jet Non-isothermal free jet Isothermal wall jet Non-isothermal wall jet Wall thermal plume Thermal boundary layer	Their objective was to setup a database with qualitative knowledge about elementary flows encountered.	Gagneau and Allard (2001)

Table 2.1 continued.

Integrated specific flow model	Cases considered	References
Thermal boundary layer Isothermal wall jet Wall thermal plume	Three-dimensional forced convection. Simulation results were compared with experimental data and CFD. They demonstrated multi-room application of zonal model.	Musy et al. (2002)
No specific flow model	Three-dimensional forced convection with the integration of moisture transfer model.	Mendoca et al. (2002)
No specific flow model	Three-dimensional forced convection with the integration of multi-zone model.	Mora et al. (2002)
Isothermal wall jet	Two-dimensional forced convection. Results were compared with CFD and experiment.	Mora et al. (2003)
Isothermal wall jet	Integrated with emission model. Three-dimensional natural and forced convection. Simulation results were compared with CFD and experiment.	Huang (2003)
Isothermal jet	Integrated with emission model.	Huang et al. (2002)
Wall non-isothermal jet Wall thermal plume Thermal boundary layer	Integrated with COMIS. Three-dimensional forced convection with pollutant dispersion. Simulation results were compared with experimental data.	Stewart and Ren (2003)
Wall non-isothermal jet Wall thermal plume Thermal boundary layer	Integrated with COMIS. Three-dimensional forced and natural convection. Simulation results were compared with experimental data.	Ren and Stewart (2003)
No specific flow model	Three-dimensional forced convection. Simulation results were compared with experimental data.	Gharbi et al. (2004)
Wall non-isothermal jet	Three-dimensional forced convection with personal exposure model. Simulation results were compared with experimental data.	Ren and Stewart (2005)

2.3.4 Improvements of the zonal models

Accurate prediction of the airflow rate is a vital step since the predictions of the other physical parameters such as moisture, temperature and contaminant distribution are highly dependent on it. Nevertheless, the zonal models discussed thus far have limitations in predicting the airflow distribution.

The non-pressures zonal were developed only for the specific zones. Moreover, these models require prior knowledge of the airflow pattern in the room, which makes them specific to the cases considered and difficult to apply to other configurations.

The integrated zonal models have given good predictions in the specific zones since well-developed empirical relations such as air jet models were used. The PLM, which is used in the standard zones, has been able to predict the flow field reasonably well only for natural convection (Haghighat et al. 2001; Gharbi et al. 2004). However, it has shown discrepancies in predicting the recirculation in the standard zone for the case of forced convection.

Mora et al. (2003) used isothermal room to demonstrate the discrepancies of the PLM. Figures 2.2 and 2.3 show the airflow pattern predicted by the zonal and CFD models, respectively. Comparison of the two figures shows that the zonal model is unable to predict the recirculation in the standard zone. Haghighat et al. (2001) have also shown the discrepancies of the PLM for an isothermal room with ceiling inlet.

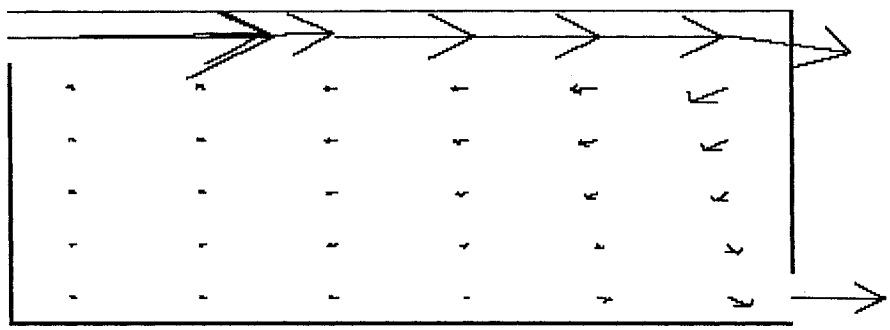

Figure 2.2 Prediction of the flow field by zonal model. Jet model was used for specific zone and PLM for standard zone (Mora et al. 2003).

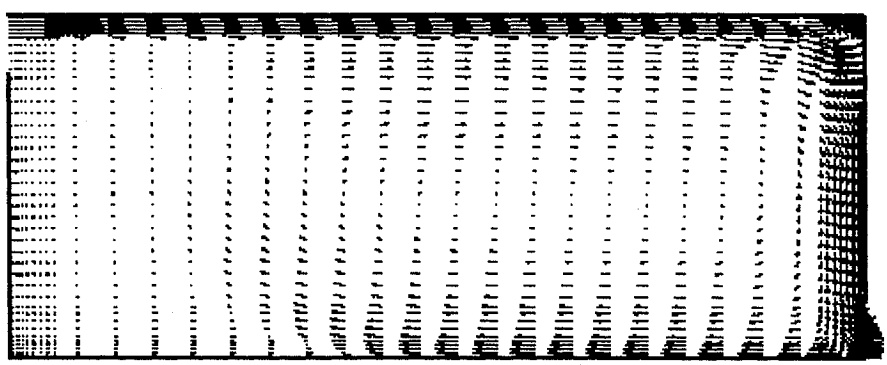

Figure 2.3 Flow field predicted by CFD using 40x40grids (Mora et al. 2003).

Three attempts were made to alleviate the mentioned limitations and hence to improve the prediction capability of the zonal models in the standard zone:

- The investigation of the sensitivity of the magnitude of airflow to the power-law flow coefficient (Wurtz et al. 1999a);
- The development of the surface-drag flow model (SDM) (Axley, 2001); and

- The development of the momentum-zonal model (MZM) (Griffith and Chen, 2003).

2.3.4.1 Sensitivity of airflow and temperature distribution to *K*

Wurtz et al. (1999a) examined the sensitivity of airflow and temperature predictions to the variation of *K*. Five values of *K* were used (0.1, 0.5, 0.7, 0.83, and 1.0); 0.83 being the commonly used value of *K*. Comparison of the zonal models air velocity and temperature prediction for the five *K* values with CFD has shown that the variation of *K* affects the magnitude of the velocity and temperature. The predictions were better at some specific locations (cells) than others, which revealed that no single value of *K* could improve the prediction of the PLM for all cells in the standard zone.

2.3.4.2 The surface-drag flow models (SDM)

Axley (2001) proposed the surface-drag flow model (SDM) to improve the prediction of zonal models in the standard zone. One of the variants of SDM, which has been considered to be better than the PLM, can be given as:

$$\Delta P_{i,j} = \frac{2\lambda\kappa^2 a^3 \Delta x}{\rho A^2 \Delta y} m_{i,j}^2 \tag{2.2}$$

where

$\Delta P_{i,j}$ is the pressure difference, Pa;

κ is the Von Karman constant;

$a = 1/7$;

Δx and Δy are the length of a cell in the x and y directions, respectively, m;

$m_{i,j}$ is the mass flow rate, kg/s;

ρ is the density of air, kg/m^3;

A is the area of a cell, m^2;

$$\lambda \approx \frac{2}{2n_s - 1};$$

n_s is the cell number = 1,2,3,... starting from the nearest cell to the surface;

Axley (2001) compared the predictions of the SDM with CFD using the same isothermal room employed by Mora et al. (2003). Figure 2.4 depicts the flow field prediction by the SDM. Comparing the flow field prediction in Figure 2.4 with Figure 2.3, it can be discerned that the SDM, like the PLM, has difficulty in predicting the formation of recirculation in the standard zone.

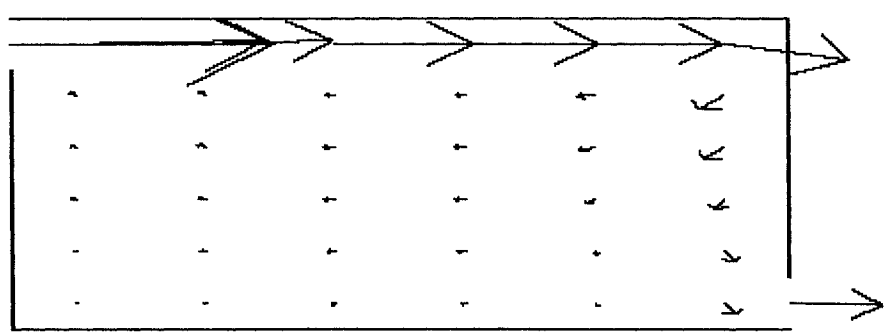

Figure 2.4 Airflow predicted by SDM. Jet model was used for specific zone and the SDM for standard zone (Mora et al. 2003).

2.3.4.3 The momentum-zonal model (MZM)

Griffith and Chen (2003) developed the MZM as an improvement to the PLM. Like the PLM, the MZM is based on the Euler equation. The PLM is the integral (macro) form of the Euler equation while the MZM is the three-dimensional Euler equation. The MZM

predicts well the temperature stratification in buoyancy-dominated flows such as natural convection, displacement ventilation and convective heating. The MZM treats all the cells in the same manner without categorizing them as part of a specific or a standard flow zone.

2.4 Discussions

The PLM has pronounced discrepancies in predicting the recirculation in the standard zone for forced convection. In this regard, attempts were made to improve the PLM predictions in the standard zone. The first revealed that as long as the same value of K is used for all cells, the prediction capability of the PLM in the standard zone could not be improved for all cells. But the significance of using the same value of K for all cells was not investigated for forced convection.

The second (SDM) used the parameter λ to adjust the prediction. Rearranging Equation 2.2 yields

$$m_{i,j} = \frac{1}{2\kappa}\left(\frac{\Delta y}{\lambda a^3 \Delta x}\right)^{1/2} \rho A \left(\frac{2\Delta P_{i,j}}{\rho}\right)^{1/2} \tag{2.3}$$

Comparing Equation 2.3 with Equation 2.1 shows that the SDM is similar to the PLM except the former has a variable coefficient due to the parameter λ. Although adjustment was made to the SDM using λ, the SDM (like the PLM) was unable to predict recirculation for forced convection. This may not be due to the physical implausibility of the use of variable parameter like λ; it could rather be due to the methodology employed. The problem with the values used for λ was that they were not consistent with the flow

pattern expected in indoor airflow. The flow coefficient, K in Equation 2.2 should have been estimated using pressure and velocity data so that physically consistent values are obtained. The velocity and temperature distribution in a room can be measured but measuring pressure distribution could be difficult due to the small pressure difference between cells in a room. Obtaining the pressure and velocity numerically using CFD is therefore a reasonable approach, which will be pursued in this study.

Moreover, since the independent application of the PLM and the SDM has resulted in discrepancies in predicting the recirculation for forced convection, the other possible way of improving the prediction of the PLM, which will be explored in this study, is combining the PLM with the SDM.

The MZM was obtained using the micro approach but the macro approach is proposed in this research. The macro approach preserves the categorization employed in the implementation of the zonal models and concentrates on improving the prediction in the zone where discrepancy occurs. Furthermore, this approach makes the future integration of the new zonal models and their application in simulation codes such as COwZ (Ren, 2002; Stewart and Ren, 2005) possible.

2.5 Summary

This chapter presented a review of indoor airflow modeling. The airflow models were categorized depending on the level of detail of information they provide as either integral (macro) or differential (micro) approaches. The integral approach includes models such

as single-zone, multi-zone (network) and zonal models. The differential approach is commonly called computational fluid dynamics (CFD).

The zonal approach divides a flow field into a number of zones with distinct flow characteristics. These zones are categorized as either a standard or a specific flow zone. The standard flow zone includes the regions outside of the specific zones such as the occupied region. The specific flow zones include jets, plumes, and boundary layer zones. The distinct characteristic of each flow zone has made it necessary to use different models to describe the airflow rate in each zone.

Different generations of zonal models have evolved over the years. These models can be categorized as first, second and third generation. These three generations of zonal models have applied non-pressure, pressure, and integration of pressure and non-pressure models to describe room air and thermal flow, respectively. The non-pressure zonal models cannot be applied for the prediction of the airflow distribution in the standard zone and they require prior knowledge of the airflow pattern in the room. The application of pressure zonal models is limited to the standard zone due to the inability of the pressure zonal models for predicting driving (specific) flows. Integrated zonal models use the pressure zonal models for standard zones and the non-pressure (empirical) models for the specific zones. These models have been implemented for predicting indoor airflow, temperature, and contaminant distribution.

The PLM, which is used in the standard zones, has been able to predict the flow field reasonably well only for natural convection. For the case of forced convection, the PLM has shown some discrepancies in predicting the recirculation in the standard zones. Hence, attempts were made to improve the prediction capability of the zonal models: the investigation of the sensitivity of the airflow rate and temperature to the flow coefficient; the development of the surface-drag flow model (SDM); and the development of the momentum-zonal model (MZM). The first revealed that as long as the same value of K is used for all cells, the prediction capability of the PLM in the standard zone could not be improved for all cells. The SDM, like the PLM, is unable to predict recirculation for forced convection. The MZM was obtained by using the micro approach but the macro approach, which gives the zonal models, is used in this research.

Finally, the new methodologies proposed for improving the zonal models are:

- Investigating the significance of using single value of K for all cells;
- Using data generated from CFD simulation for the estimation of K; and
- Combining the PLM with the SDM.

3 THE ZONAL METHOD

The three commonly used models for the prediction of airflow in a room: single-zone, CFD, and zonal, were discussed in Chapter 2. In the zonal approach, a zone is categorized as a standard or a specific flow zones. The non-pressure zonal models, which are mostly empirical, have been used to describe the airflow rate for cells in the specific zones. The pressure zonal models, such as the PLM and the SDM have been applied to calculate the airflow in the standard zone.

The advantage of the zonal approach is that the resulting systems of equations are relatively small and easier to solve. The systems of equations are the result of the application of the conservation equations for each cell, which can be written as follows:

$$\frac{(Quantity)_{t+1} - (Quantitiy)_t}{\Delta t} = (Quantity)_{in} - (Quantity)_{out} + Generation \tag{3.1}$$

where

Quantity refers to mass, energy, and momentum;

t is time, s.

The solution of Equation 3.1 provides the distribution of variables such as airflow rates, temperature, and pressure. In order to solve Equation 3.1, using existing numerical algorithms, the mass and energy flow into and out of each cell should be formulated in terms of these variables.

The existing zonal models will be used as a basis for developing a new generation of zonal models in Chapter 4 and the solution algorithms are also applicable to the new zonal models. Consequently, this chapter addresses the airflow equations in Section 3.1, the energy equations in Section 3.2 and the methodologies applied to solve the airflow and energy equations in Section 3.3. Finally, the points discussed in this chapter are summarized in Section 3.4.

3.1 The airflow equations

The form of Equation 3.1, for mass balance with no accumulation (steady state), can be written as:

$$\sum m_{i,j} + S_M = 0 \tag{3.2}$$

where

S_M is the sum of the mass source or sink in a cell, kg/s;

$\sum m_{i,j}$ is the sum of the airflow rates through the boundaries of a cell (i,j), kg/s.

For two-dimensional airflow:

$$\sum m_{i,j} = m_{x(i,j)} + m_{x(i-1,j)} + m_{y(i,j)} + m_{y(i,j-1)} \tag{3.3}$$

where

$m_{x(i,j)}$, $m_{x(i-1,j)}$, $m_{y(i,j)}$, and $m_{y(i,j-1)}$ are the airflow rates through the boundaries of cell (i,j), as shown in Figure 3.1, kg/s.

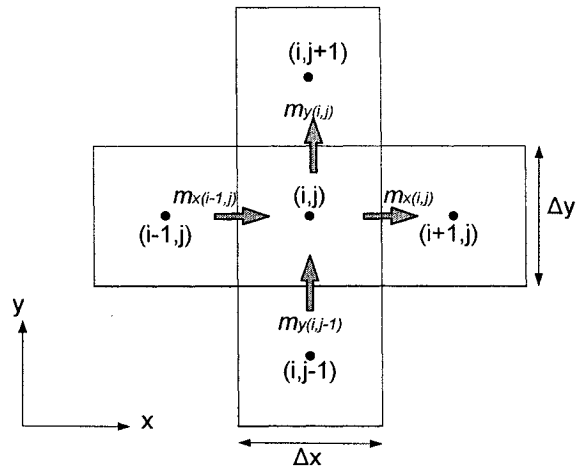

Figure 3.1 Airflow through the boundaries of cell (i,j).

The zonal airflow models express the airflow rate in terms of pressure difference for cells in the standard zone; and in terms of inlet airflow rate, inlet width and distance from the inlet for cells in the air jet zone. For cells in the mixed zone, which are combination of standard and specific flows, the standard cell equations are applied for the sub-cell that contains the flow outside of the specific flow zone; whereas the specific flow equations are used for the sub-cell that contains the specific flow part. The total mass flow rate for the mixed cell is therefore the sum of the mass flow rate through the two sub-cells (Haghighat et al. 2001; Musy et al. 2002; Ren, 2002).

The airflow models for the standard and specific flow zones and their solution procedure are discussed in the following subsections.

3.1.1 The standard flow zone

The pressure zonal models, the PLM and the SDM, are employed to calculate the airflow rate between two neighboring cells in the standard zone. This subsection, therefore, presents the basic features of the PLM and the SDM, which are pivotal in the subsequent development of the new zonal models.

3.1.1.1 The power-law model (PLM)

The PLM, which is used to calculate the airflow rate between cells in standard zone, is based on methods used for airflow through cracks, orifices and large openings. The PLM describes the airflow rate through the boundaries of cell (i,j), shown in Figure 3.1, using the following relations:

$$m_{x(i,j)} = K\Delta y l\left(2\rho_{i,j}(P_{i,j} - P_{i+1,j})\right)^{1/2} \tag{3.4}$$

$$m_{y(i,j)} = K\Delta x l\left(2\rho_{i,j}(P_{i,j} - P_{i,j+1})\right)^{1/2} \tag{3.5}$$

where

l is the width of the cells, m;

$P_{i,j}$, $P_{i+1,j}$, and $P_{i,j+1}$ are the pressures at the center of cells (i,j), (i+1,j) and (i,j+1), Pa;

K is the flow coefficient = 0.83;

$\rho_{i,j}$ is density of air in cell(i,j), kg/m^3.

The density of air in cell (i,j) is calculated using the ideal gas equation:

$$\rho_{i,j} = \frac{P_{i,j}}{RT_{i,j}} \tag{3.6}$$

where

$T_{i,j}$ is temperature of cell (i,j), K;

R is the gas constant for air = 287.055 J/kg.K.

The pressure $P_{i,j}$ for a cell is calculated by using the hydrostatic relation:

$$P_{i,j} = P_{ref} + g\rho_{i,j} y_{i,j} \tag{3.7}$$

where

P_{ref} is the reference pressure in the room, Pa;

g is the gravitational acceleration, m/s^2;

$y_{i,j}$ is the vertical distance of the cell (i,j) from the zone floor, m.

The calculation of the pressure difference depends on the flow direction. For vertical flow through horizontal interfaces of neighboring cells, the pressure difference is uniform at the location of the interface and the airflow is either in the positive or in the negative y-direction. For horizontal flow through vertical interfaces, however, the airflow can be in the positive and negative x-direction, Figure 3.2 (Haghighat et al. 2001; Wurtz et al. 1999a; Ren, 2002). This shows that the airflow can be reversed below a certain height from the horizontal interface and the pressure difference at this height is zero. This height is called the neutral height, which can be given as (Haghighat et al. 2001):

$$Y_{neut} = \frac{P_{(i,j)b} - P_{(i,j+1)b}}{(\rho_{i,j} - \rho_{i+1,j})g} \tag{3.8}$$

where

Y_{neut} is the height of the neutral plane, m;

$P_{(i,j)b}$ and $P_{(i+1,j)b}$ are the pressures at the bottom of cells (i,j) and (i+1,j), Pa.

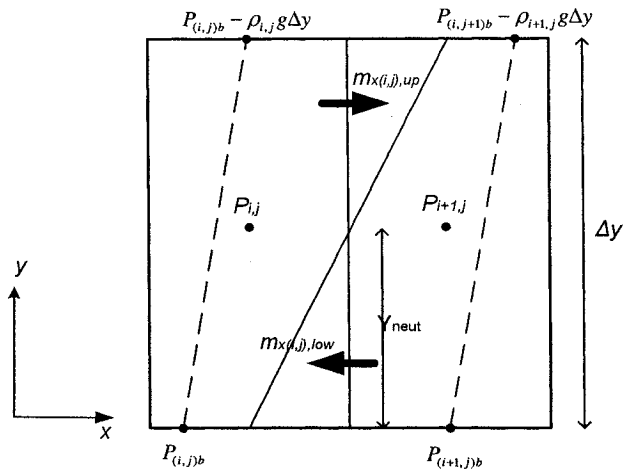

Figure 3.2 Airflow rate calculations at a vertical cell interface.

As shown in Figure 3.2, the airflow through the vertical interface is divided into two parts: the upper and the lower part. The airflow rates for the lower and the upper part are evaluated by (Haghighat et al. 2001):

$$m_{x(i,j),low} = Kl\left|2\rho_{i+1,j}\Delta\rho g\right|^{0.5}\frac{\left|Y_{neut}\right|^{1.5}}{1.5} \tag{3.9}$$

$$m_{x(i,j),up} = Kl\left|2\rho_{i,j}\Delta\rho g\right|^{0.5}\frac{\left|Y_{neut}-\Delta y\right|^{1.5}}{1.5} \tag{3.10}$$

where

$m_{(i+1,j),low}$ is the airflow rate below the neutral plane, kg/s;

$m_{(i,j),up}$ is the airflow rate above the neutral plane, kg/s.

Therefore, for the horizontal flow, the mass flow rate crossing the vertical boundary is the sum of the mass flow rates above and below Y_{neut} (Haghighat et al. 2001):

$$m_{x(i,j)} = m_{x(i,j),low} + m_{x(i+1,j),up} \tag{3.11}$$

3.1.1.2 The surface-drag flow models (SDM)

The SDM is one of the models proposed for improving the prediction capability of the PLM in the standard zone. Axley (2001) developed this model by considering the transfer of shear stress near wall surfaces using a momentum balance on a differential flow element linking neighboring zones as shown in Figure 3.3. Basically, he employed a relation similar to the Poiseuille flow equation, which can be given as:

$$\frac{dP}{dx} = \frac{d\tau_{yx}}{dy} \tag{3.12}$$

where

τ_{yx} is the shear stress, Pa.

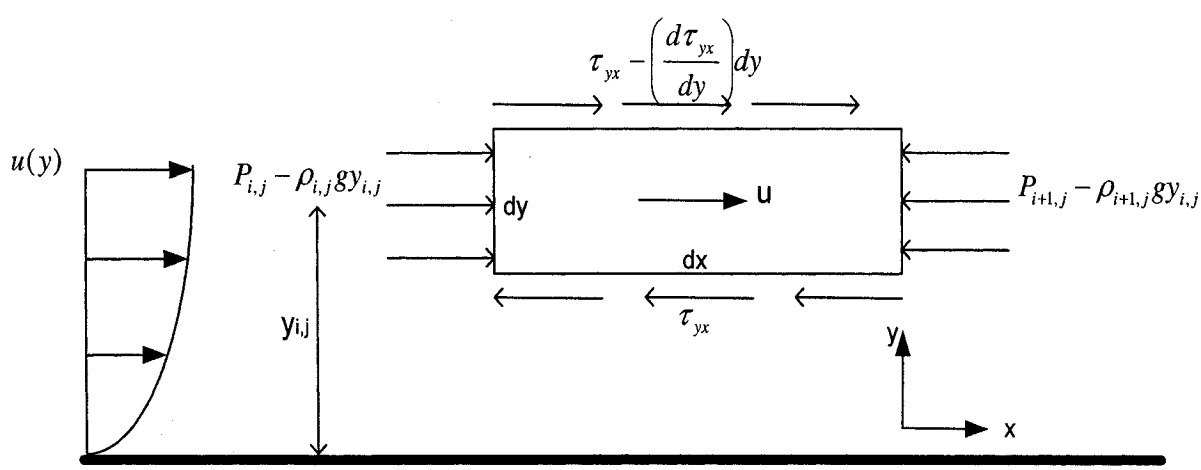

Figure 3.3 The surface-drag momentum balance model (Axley, 2001).

The shear stress is related to the velocity u(y) using fundamental relations for laminar and turbulent flow. For the latter, either eddy viscosity or Prandtl's mixing length approximations can be used (Axley, 2001):

- Eddy viscosity approximation

$$\tau_{yx} \approx -\mu_e \frac{du}{dy} \tag{3.13}$$

- Mixing length approximation

$$\tau_{yx} \approx -\rho\kappa^2 y^2 \left(\frac{du}{dy}\right)^2 \tag{3.14}$$

where

μ_e is the eddy viscosity of air, kg/m.s.

κ is the Von Karman constant = 0.4.

In order to describe the velocity profiles for laminar and turbulent flow the quarter-sine and power-law velocity profiles have been applied (Axley 2001):

- Quarter-sine profile

$$u \approx u_{\max} \sin\left(\frac{\pi y}{2Y}\right) \tag{3.15}$$

- Power-law profile

$$u \approx u_{\max} \left(\frac{y}{2Y}\right)^a \tag{3.16}$$

where

u_{max} is the maximum velocity, m/s;

Y is the characteristic room dimension, which is equal to half the distance between opposite room surfaces, m;

a =1/7.

The relation between mass flow rate and pressure was obtained by first substituting Equations 3.15 and 3.16 into Equations 3.13 and 3.14 and then inserting Equations 3.13 and 3.14 into Equation 3.12 and integrating over the cell height. The form of the final SDM depends on the type of turbulence model and the velocity profile (Axley, 2001):

- Eddy viscosity approximation and quarter sine profile

$$P_{i,j} - P_{i+1,j} = \frac{\mu_e \pi^2 \Delta x}{4\rho Y^2 A} m_{x(i,j)} \tag{3.17}$$

- Mixing length approximation and power-law profile

$$P_{i,j} - P_{i+1,j} = \frac{2\lambda \kappa^2 a^3 \Delta x}{\rho A^2 \Delta y} m_{x(i,j)}^2 \tag{3.18}$$

where

λ is the surface-drag flow coefficient.

Axley (2001) estimated λ for each cell and room average eddy viscosity using the following relations:

$$\lambda \approx \frac{2}{2n_s - 1} \tag{3.19}$$

$$\mu_e \approx 0.025 Y U_m \rho \tag{3.20}$$

where

n_s is the cell number = 1,2,3,... starting from the nearest cell to the surface;

U_m is the characteristic mean velocity of the room air, m/s.

3.1.2 The specific flow zones

The non-pressure zonal models are the earlier zonal models, which employ empirical and analytical relations to express the mass flow rate between cells in specific zones such as air jet, thermal plumes, and boundary layers.

3.1.2.1 Air jets

Turbulent air jets distribute air supplied into a room through inlet devices such as grilles and ceiling diffusers. The maximum or centerline velocity of straight flow isothermal jets can be determined from the following equation (ASHRAE 2001):

$$U_x = \frac{CU_0\sqrt{A_0}}{x} \tag{3.21}$$

where

C is the proportionality constant, which depends on the type of the diffuser;

U_0 is the average velocity at the inlet, m/s;

x is the distance from the supply, m;

U_x is the centerline velocity at distance x, m/s;

A_0 is the core area, m^2;

The trajectory of a non-isothermal horizontal air jet is affected by the Archimedes number, which can be given as:

$$Ar_0 = \frac{gh_0\beta(T_0 - T_{indoor})}{U_0^2} \tag{3.22}$$

where

Ar_0 is the Archimedes number;

h_0 is the width of the diffuser, m;

T_0 is the inlet temperature of the air jet, K;

T_{indoor} is the temperature of the room air, K;

β is the thermal expansion coefficient of the room air, $1/K$.

For slot air inlet, Ar_0 should be less than 0.023 so that the air jet remains attached to the ceiling (Zhang, 1991). The distance from the diffuser to the point where the air jet separates from the ceiling is called the jet penetration length (L_p).

3.1.2.2 Thermal plumes and boundary layers

Thermal plums are created over hot surfaces, heaters and occupants. A concentrated heat source creates a circular plum and a line source creates plane plum. If the heat source is close to a wall it is called a wall plum. When the surface temperature of a wall is different from the local room air, there is always natural convection heat transfer between the wall surface and the room air through the thermal boundary layer. The equations commonly used to calculate airflow in a thermal plum relate the heating capacity of the heat source to the airflow rate. For the thermal boundary layer, empirical equations that relate the air flow rate in the thermal boundary layer to the temperature difference between the room air and wall surface can be obtained. For detailed review of airflow models for specific zone, the reader is referred to Ren (2002) and Stewart and Ren (2005).

3.1.3 Numerical solution of the airflow equations

The numerical procedure used to solve the nonlinear system of equations of pressure is based on the balance of mass flow for each cell. The Newton-Raphson method is used to solve the nonlinear problem by an iterative solution. The solution of these systems of equations is achieved by an iterative mass balance approach in which cell pressures are adjusted until the mass residual of each zone is minimized.

In the Newton-Raphson method, a new estimate of the vector of all cell pressures is computed from the previous estimate of pressures by

$$\vec{P}_{n+1} = \vec{P}_n - \vec{C} \tag{3.23}$$

where

$\vec{P}_n$ and $\vec{P}_{n+1}$ are the pressure vectors for the previous and current estimate, respectively;

$\vec{C}$ is the correction vector computed by

$$\vec{C} = \overset{\Rightarrow}{J}^{-1} \vec{B} \tag{3.24}$$

where

$\vec{B}$ is a column vector with each element B_j given by the mass balance (Equation 3.2) in each cell:

$$B_j = \sum m_{i,j} + S_{M(i,j)} \tag{3.25}$$

$\overset{\Rightarrow}{J}$ is the square Jacobian matrix whose elements $J_{i,j}$ are given by

$$J_{i,j} = \frac{\partial \sum m_{i,j}}{\partial P_{i,j}} \tag{3.26}$$

$\sum m_{i,j}$ and $\frac{\partial \sum m_{i,j}}{\partial P_{i,j}}$ are evaluated using the current estimate of pressure $P_{i,j}$. Numerical tests of the Newton-Raphson method could indicate occasional instances of very slow convergence and the iterations oscillate between two different sets of values. Dols and Walton (2002) and Press et al. (1996) have shown that the use of under-relaxation coefficient β produces a faster and more reliable convergence accelerating process. Thus, Equation 3.23 for the iteration process becomes:

$$\vec{P}_{n+1} = \vec{P}_n - \beta \vec{C} \tag{3.27}$$

A line search and backtracking method can be used to find a proper value of β. The search starts by first trying the full Newton step, $\beta = 1$ (Equation 3.23). If $\vec{P}_{n+1}$ cannot meet the acceptance criteria, backtrack along the Newton direction using a smaller value of β until a suitable point is found. The detail of the criteria for accepting β can be found in Press et al. (1996).

3.2 The energy equations

Air and thermal flows in a room are coupled. Moreover, the local distribution of airflow rates and temperature affect the thermal comfort and building energy consumption. This indicates that the zonal approach, in addition to airflow rate distribution, has to be able to predict the temperature distribution in a room with a reasonable accuracy. Consequently, coupled mass and thermal balance equations for each cell are solved.

For any cell (i,j) shown in Figure 3.4, the thermal energy balance can be written as follows:

$$m_{i,j} c_p \frac{dT_{i,j}}{dt} = \sum q_{i,j} + S_{Th(i,j)} \tag{3.28}$$

where

$m_{i,j}$ is the mass of air in cell (i,j), kg;

c_p is the specific heat capacity of air, J/Kg.K;

$T_{i,j}$ is the temperature of cell (i,j), K;

$\sum q_{i,j}$ is the sum of heat flow through the boundaries of cell (i,j), W;

$S_{Th(i,j)}$ is the heat generated or removed within the cell, W.

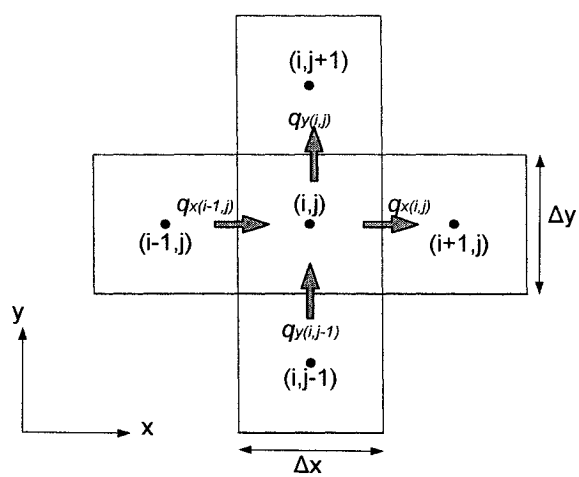

Figure 3.4 Energy flow through the boundaries of a cell (i,j).

For two-dimensional airflow:

$$\sum q_{i,j} = q_{x(i,j)} + q_{x(i-1,j)} + q_{y(i,j)} + q_{y(i,j-1)} \tag{3.29}$$

where

$q_{x(i,j)}$, $q_{x(i-1,j)}$, $q_{y(i,j)}$, and $q_{y(i,j-1)}$ are the energy flows through the boundaries of cell (i,j) as shown in Figure 3.4, W.

The heat exchange of a cell with neighboring cells is the sum of the heat transfer due to advection and diffusion. One of the simplifications in the zonal approach is that the diffusion is considered very small and neglected. Therefore, the heat flow in the x and y directions shown in Figure 3.4 can be calculated as:

$$q_{x(i,j)} = m_{x(i,j)} c_p (T_{i,j} - T_{i+1,j}) \tag{3.30}$$

$$q_{y(i,j)} = m_{y(i,j)} c_p (T_{i,j} - T_{i,j+1}) \tag{3.31}$$

where

$T_{i,j}$, $T_{i+1,j}$ and $T_{i,j+1}$ are the temperatures at the center of cells (i,j), (i+1,j) and (i,j+1), K.

Furthermore, if one or more of the cell boundaries are adjacent to the surfaces (façade, wall, floor and ceiling), the convective heat flux between the wall surfaces and the air in the cell will also be part of $\sum q_{i,j}$ in Equation 3.29 and replaces one or more of the terms in the right side. The heat transferred due to convection (q_{conv}) can be evaluated as:

$$q_{conv} = h_{conv} A_{i,j} (T_{surf} - T_{i,j}) \tag{3.32}$$

where

q_{conv} is the heat transferred due to convection, W;

h_{conv} is the convective heat transfer coefficient, W/m^2.K;

$A_{i,j}$ is the area of the surface, m^2;

T_{surf} is the temperature of the surface boundary, ^{o}C.

For a full description of the thermal flow in a room, the heat transfer coefficient (h_{conv}) and the thermal boundary conditions such as surface temperature or surface heat flux should be known. If the surface temperatures or surface heat fluxes are not known, they should be calculated using the energy balance, Equation 3.28.

The convective heat transfer coefficient (h_{conv}) varies depending on the local airflow pattern and the temperature gradients in a room. In general, there are four methods for evaluating the surface heat transfer coefficient: dimensional analysis combined with experimental data, CFD, approximate boundary layer analysis based on integral techniques, and analogy between heat, mass and momentum transfer (Bejan, 1995). It is difficult to develop and implement models for predicting surface heat transfer coefficients for all possible flow regimes encountered within buildings. Thus empirical relations for the heat transfer coefficient, which have been found to provide reasonable prediction, are normally used in the zonal approach.

For natural convection caused by surface-to-air temperature difference without the use of heating device, constant values or simple relations for vertical and horizontal surfaces are used (ASHRAE, 2001). Other empirical relations used for zonal model application are correlations developed by Alamdari and Hammond (1983). Their correlations for natural convection are specifically developed for building applications. These correlations have been found to give good results (Arnold et al. 1998). Moreover, Ren, (2002) has also employed these correlations for CowZ (COMIS integrated with zonal model).

Fisher (1995) conducted experiments to describe surface heat transfer coefficient for forced convection at internal surfaces of rooms. Fisher's correlations have been applied in Esp-r program (Beausoleil-Morrison, 2000) and in CowZ (Ren, 2002). Awbi and Hatton (2000) have also developed correlations for mixed convection.

3.3 Solution of the airflow and energy equations

The solution procedure selected in this study is commonly used in the zonal approach and was recently implemented by Stewart and Ren (2005) and Gharbi et al. (2004). This procedure solves the thermal balance equations for internal cells and surfaces for a known outside air and inlet temperatures. The convective heat transfer coefficients may have fixed values or can be determined by using empirical equations for natural, forced, and mixed convection. In the case of the former, the energy balance equations become linear and can be solved directly; for the latter, however, the calculation of heat transfer coefficient will be based on the air temperature of the previous iteration.

The energy balance (Equation 3.28) can have the following general form:

$$A_P T_{i,j} = A_W T_{i-1,j} + A_E T_{i+1,j} + A_S T_{i,j-1} + A_N T_{i,j+1} + S_{Th} \tag{3.33}$$

where

$A_W = c_p \max[m_{x(i-1,j)}, 0];$

$A_E = c_p \max[-m_{x(i,j)}, 0];$

$A_S = c_p \max[m_{y(i,j-1)}, 0];$

$A_N = c_p \max[-m_{y(i,j)}, 0];$

$$A_P = A_W + A_E + A_S + A_N + \sum_{0}^{N_{surf}} h_{conv} A_{i,j};$$

$$S_{Th} = \sum_{0}^{N_{surf}} h_{conv} A_{i,j} T_{surf};$$

N_{surf} is the number of surfaces adjacent to cell (i,j).

For the non-isothermal case both airflow and the thermal flow equation should be solved simultaneously in order to get the distribution of airflow rate and temperature. The numerical solution algorithm, Newton-Raphson method, first solved the mass balance equations (Equation 3.2) using known initial and boundary conditions. The calculated airflow rates for each cell were then inserted into Equation 3.33 to calculate the temperature in each cell using the Tri-Diagonal Matrix Algorithm (TDMA). The newly calculated temperatures were used as initial condition for the calculation of airflow rates in the next iteration. The solution procedure is summarized in Figure 3.5.

Furthermore, in order to increase the rate of convergence, the newly calculated temperatures were not used directly for the next iteration step. They were corrected using the temperatures from the previous step:

$$T_{n+1} = T_{n+1} + \beta(T_{n+1} - T_n) \tag{3.34}$$

where

T_{n+1} is the newly calculated cell temperature, °C;

T_n is the cell temperature calculated in the previous iteration step, °C ;

β is the under-relaxation factor, $0 \le \beta \le 1$.

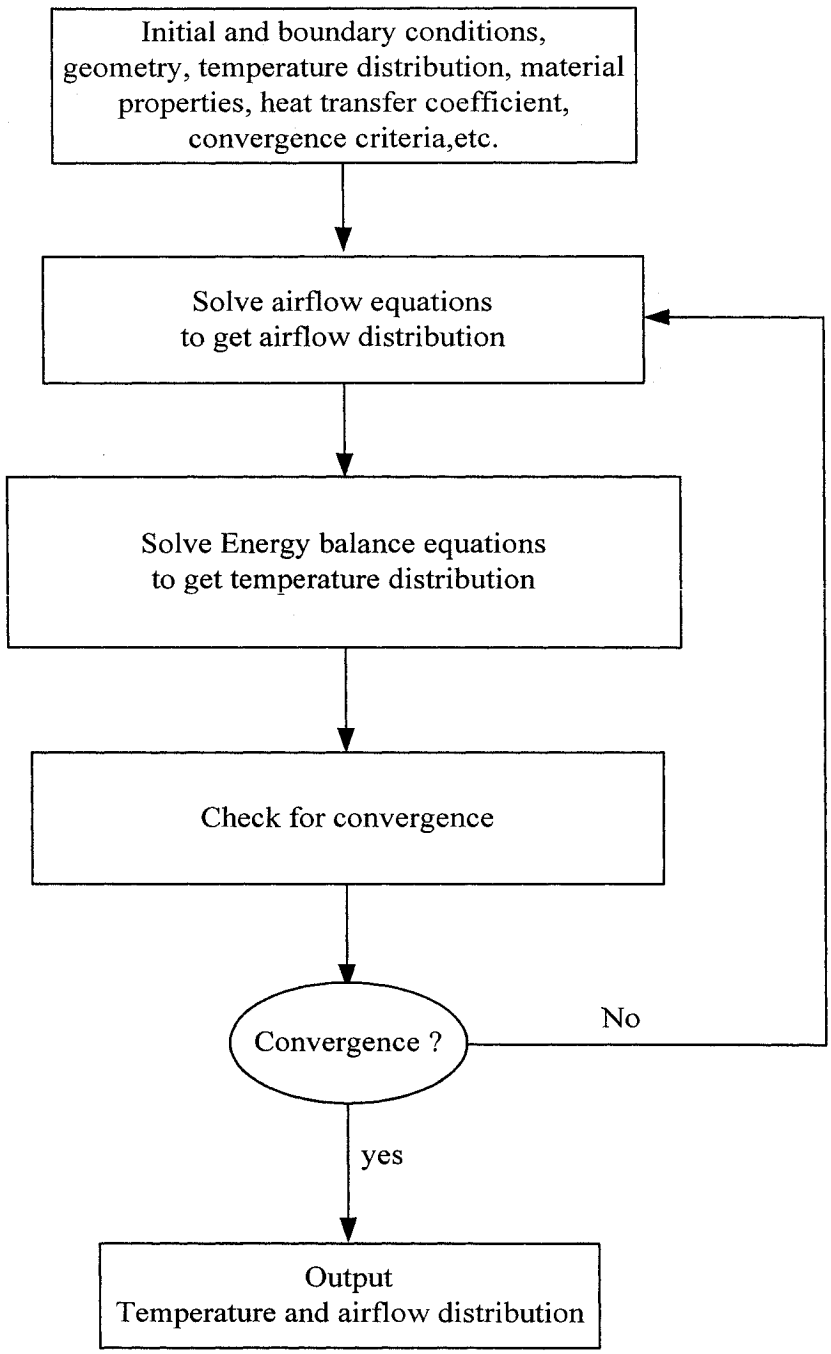

Figure 3.5 Summary of the solution procedure for zonal airflow and thermal models.

3.4 Summary

In this chapter the airflow and energy equations for cells in the standard, specific and mixed zones, and their solution procedure were discussed.

In the zonal approach, the airflow for each cell in the standard zone is evaluated by using either the power-law model (PLM) or surface-drag flow model (SDM). Empirical relations have been used to describe the airflow for cells in the specific zone. Since the cells in the mixed zone are partly standard and partly specific, the PLM or the SDM have been applied for the standard part and the empirical models are used for the specific part.

The numerical procedure for solving the nonlinear system of equations of pressure is based on the balance of mass flow for each cell. The Newton-Raphson method was used to solve the nonlinear problem by an iteration of the solutions of system of equations. For the energy equation, the TDMA has been employed. The solution of a non-isothermal airflow involves the combination of the Newton-Raphson and TDMA procedures.

4 MODEL DEVELOPMENT AND VERIFICATION

It was highlighted in the literature review that the PLM shows discrepancy in predicting the airflow rate in the standard zone. One of the difficulties in obtaining good prediction of the airflow rate is that the PLM is a one-dimensional model and no flow information has been incorporated from the other directions. As can be observed from Equations 3.4 and 3.5, the airflow rate is calculated from the pressure difference, which makes the PLM similar to the orifice equation. In the case of the latter, the values of the pressure difference are obtained from pressures measured at points away from the opening so that the influence of the airflow is negligible. The orifice equation is therefore a reasonable model when the kinetic energy of the air flowing through small openings and cracks is completely dissipated in the static room air (Kato, 2004). This is the hydrostatic field assumption, which has been used for the definition of the discharge coefficient (Sandberg, 2004; Etheridge, 2004). Therefore, the root causes of the discrepancies of the PLM can be traced back to such assumptions used in applying the PLM to describe the airflow in the standard zone.

This Chapter, therefore, addresses the discrepancies of the PLM prediction by employing the proposed methodologies for improving the PLM.

- Wurtz et al. (1999a) have shown the sensitivity of the airflow to the changes of K for only natural convection. This method will be investigated further to explore

the possibility of finding any appropriate K value other than 0.83 for forced convection in Section 4.1.

- Axley (2001) made adjustment to the SDM using the parameter λ. But the problem with the value used for λ is that it could not be consistent with the flow pattern expected in indoor airflow. Hence, the use of variable flow coefficient K for each cell is addressed in Section 4.2.
- The third approach proposed in this study is combining the PLM and the SDM. The two types of combinations, direct and indirect approaches, are presented in Section 4.3.
- The applications of the new zonal models for isothermal and non-isothermal rooms are discussed in Sections 4.4 and 4.5, respectively, and the findings of this chapter are summarized in Section 4.6.

4.1 One flow coefficient for all cells

Wurtz et al. (1999a) have shown the sensitivity of the airflow to the changes of K for natural convection. They considered five values of K (0.1, 0.5, 0.7, 0.83, and 1.0). In this section, this approach will be examined for forced convection. In addition to the above-mentioned values, 1.25, and 2.0 were also included to explore possibility of using K value greater than 1.0 in the PLM.

4.1.1 Case description

An isothermal room with two-dimensional slot inlet, as shown in Figure 4.1 (Nielsen, 1998), with length (L) = 5.4m, height (H) = 2.5m, inlet width (h_0) = 0.01m, outlet width = 0.125m, and inlet velocity (U_0) = 3.47m/s (Re = 2210), was selected. The velocity measurements in the room were made by a low velocity flow analyzer type 54N10 from Dantec with accuracy of about 0.04m/s. For the simulation, the room was divided into 11x11 cells, the PLM was used for cells in the standard zone ($y/H < 0.8$) and air jet model was applied for cells in the jet zone.

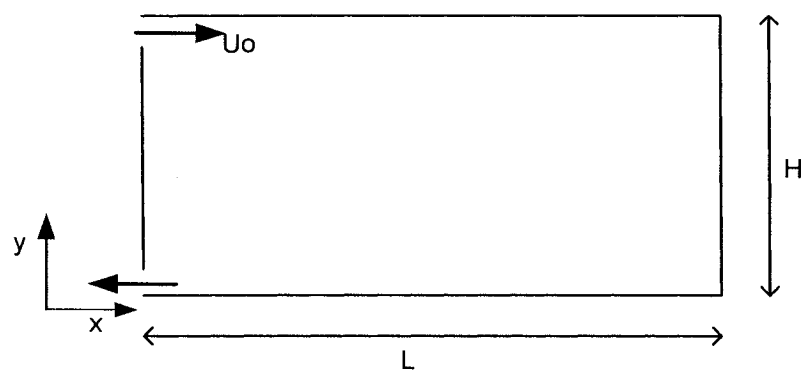

Figure 4.1 Dimensions of the room used for comparing the velocity prediction of different K values (Nielsen, 1998).

4.1.2 Results and discussions

The comparison of the dimensionless air velocity (U/U_0) predicted by the PLM for the seven K values with the measured data, at two vertical positions in the room: x = 1m and x = 3m, are depicted in Figures 4.2 and 4.3, respectively. For both positions, the PLM predicted the same air velocity profiles for all values of K at a given height. But for all

values of K, the PLM predictions are unable to follow the experimental air velocity profile and underestimate the magnitude of the air velocity in the standard zone at both vertical positions. Good predictions were obtained in the specific zone ($y > 0.9$) since Equation 3.21 was applied for all cells in this zone. The discrepancy of the PLM prediction in the standard zone is more pronounced at x = 3m than x = 1m since the former is in the recirculation region (see Figure 4.6).

For the case of natural convection, the variation of K affects the magnitude of the velocity and the predictions were similar to that of CFD for some cells (Wurtz et al. 1999a). This is because the airflow is only due to the density difference and there is no influence from inlet air jet. The density variation compensates for the constant K values used for natural convection, which makes the PLM to have implicitly different K value for each cell.

4.1.3 Concluding remarks

The following remarks could be drawn from the results of this section:

- For forced convection, as long as the same value of K is used for all cells, it is impossible to improve the prediction capability of the PLM in the standard zone.
- The implicit use of variable K for natural convection coupled with the use of variable parameter such as λ in the SDM dictates that the investigation for improving PLM with regard to K values should concentrate on exploring the possibility of using different K values for each cell.

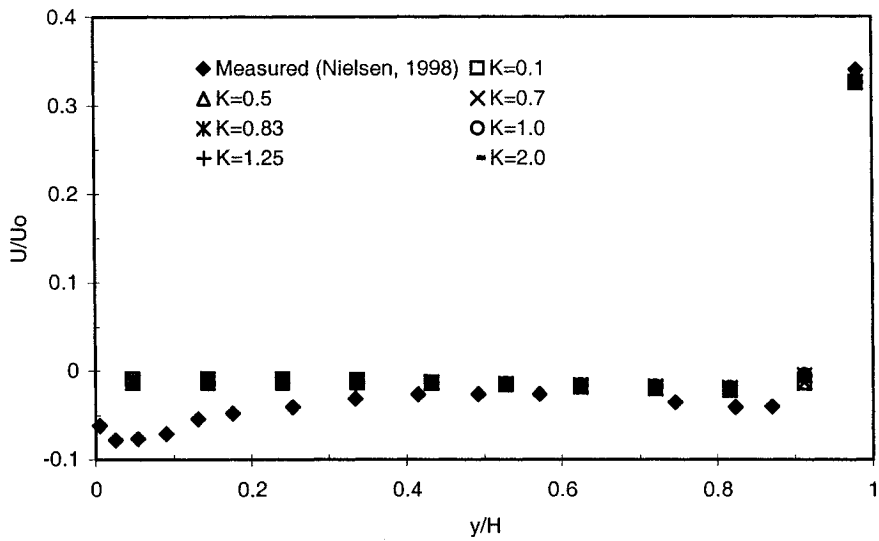

Figure 4.2 Comparison of the PLM prediction for the selected *K* values at x = 1m.

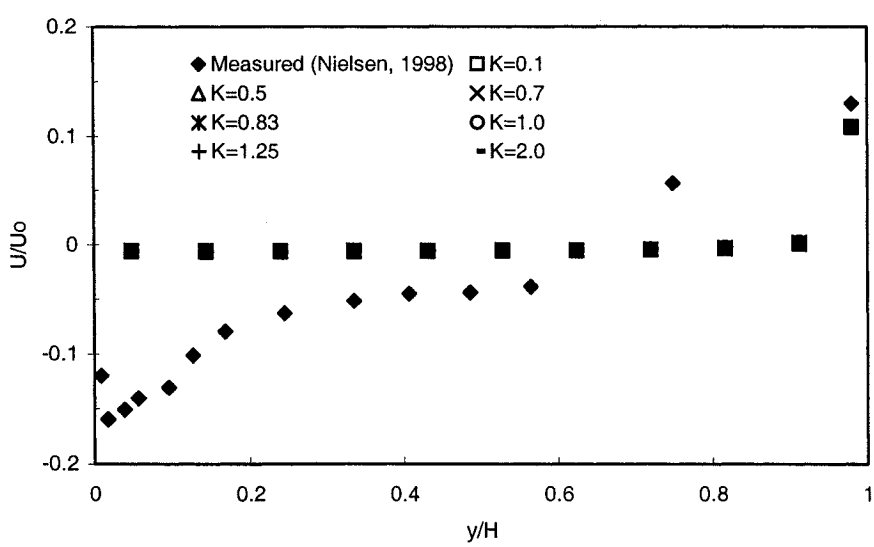

Figure 4.3 Comparison of the PLM prediction for the selected *K* values at x = 3m.

4.2 Different flow coefficients for each cell

The approach requires that each cell must have a different K value, which can be estimated either experimentally or numerically. The velocity and temperature distributions in a room can be measured. But measuring pressure distribution could be difficult due to the small pressure difference between two locations in a room. Obtaining the pressure and velocity numerically using CFD is therefore a reasonable approach. This is due to the fact that CFD has been used to predict the airflow, temperature and contaminant distribution in a room (Haghighat et al.1992; Chen and Xu 1998; Topp et al. 2001) and it has been applied and validated extensively for number of cases (see Nielsen, 1998).

4.2.1 Case description

In order to examine the effect of the type of inlet and its location on the variability of K, three cases were considered for an isothermal room:

- Case I: slot inlet at the top of the left wall and outlet at the bottom of the same wall, as depicted in Figure 4.1.
- Case II: ceiling grille diffuser at the middle of the ceiling and outlet at the bottom of one of the walls, as depicted in Figure 4.4.
- Case III: ceiling diffuser at the middle of the ceiling and outlet at the bottom of one of the walls, as depicted Figure 4.5.

For all cases, the dimensions of the rooms were: L = 5.4m, H = 2.5m, h_0 = 0.01m and outlet width = 0.125m. As mentioned before, Nielsen (1998) used Case I for Re = 2210

(U_0 = 3.47m/s). Other values of *Re* were also used (1000, 3500, 5000, and 10000) for each case to explored the influence of *Re* on the variation of *K*.

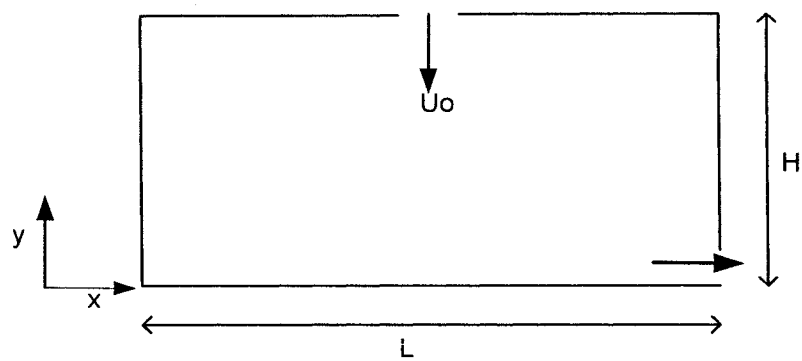

Figure 4.4 Case II: Grille diffuser, and outlet at the bottom of one of the walls.

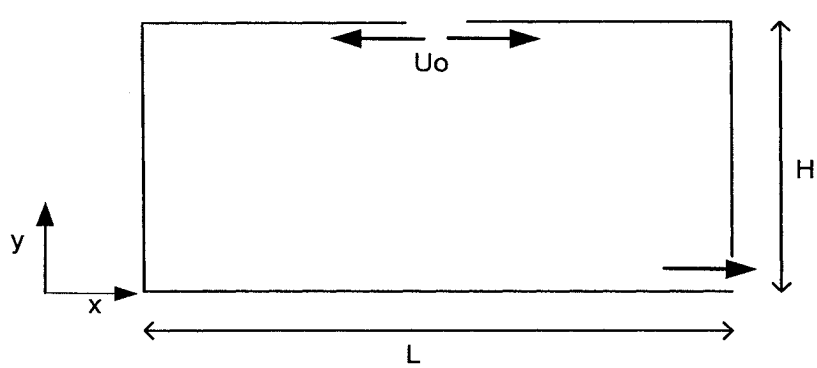

Figure 4.5 Case III: Ceiling diffuser and outlet at the bottom of one of the walls.

4.2.2 Verification of CFD predictions

The most commonly used turbulence model, the k-ε model, was applied for all cases. The inlet turbulence conditions were estimated using the following equations (Nielsen, 1990):

$$k_0 = 1.5(0.04U_0)^2 \tag{4.1}$$

$$\varepsilon_0 = \frac{10k_0^{1.5}}{h_0} \tag{4.2}$$

where

k_o turbulence kinetic energy, m^2/s^2;

U_0 is the inlet velocity, m/s;

ε_0 is the turbulence dissipation at the inlet, m^2/s^3.

A combination of AirPak (AirPak, 2002) and Fluent (Fluent, 2003) softwares was employed for the simulation. First, AirPak was used to create the room geometry and generate grids since AirPak automatically generates optimal grids for a given geometry and reduces user effort required to model diffusers. The automatically generated grids were used without any further refinement for all cases since they were good enough to demonstrate the variability of K. Since detailed air velocity and pressure data is not easy to get from AirPak for post-processing, the geometry was then imported to Fluent to perform the simulation and post-processing.

Similar airflow pattern were predicted for all Re due to the isothermal condition. Hence, only the predicted airflow pattern for Re = 2210 were selected for qualitative and quantitative verifications. Figures 4.6 to 4.8 depict the airflow pattern predicted for Cases

I to III. Comparing the predictions for the three cases, it can be observed that wall slot inlet, Figures 4.6, has produced one recirculation region with its center close to the middle of the room whereas the ceiling inlets, which discharge air vertically and horizontally, as shown in Figures 4.7 and 4.8, respectively have produced two recirculation regions.

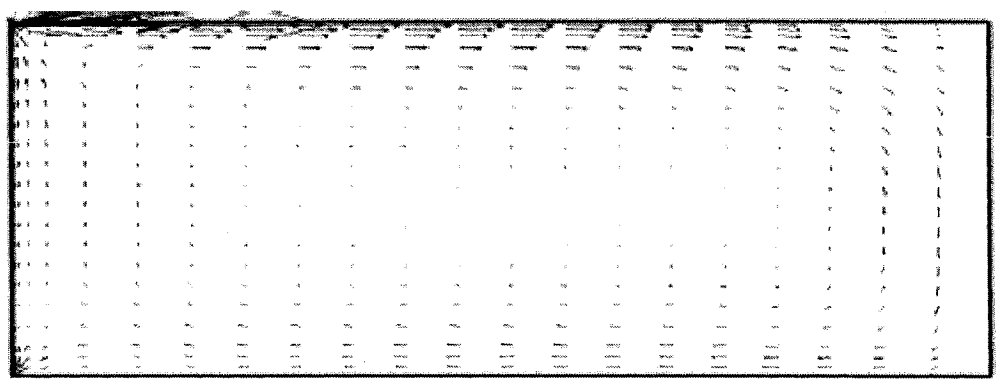

Figure 4.6 Flow pattern predicted by CFD for *Re* = 2210, Case I.

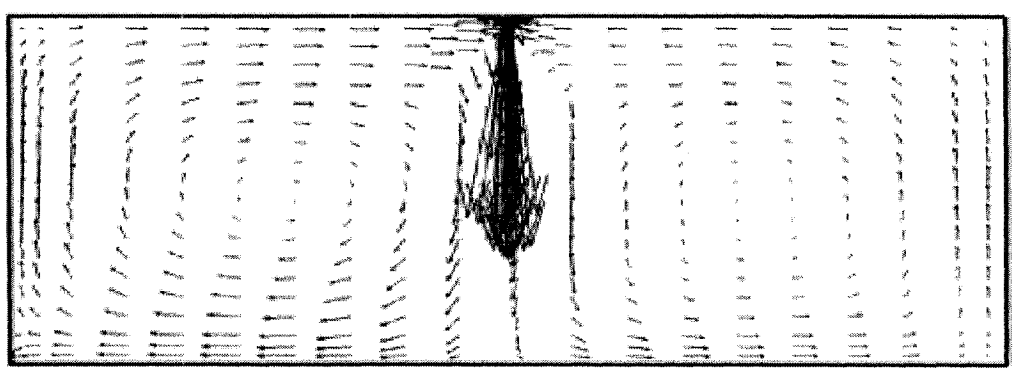

Figure 4.7 Flow pattern predicted by CFD for *Re* = 2210, Case II.

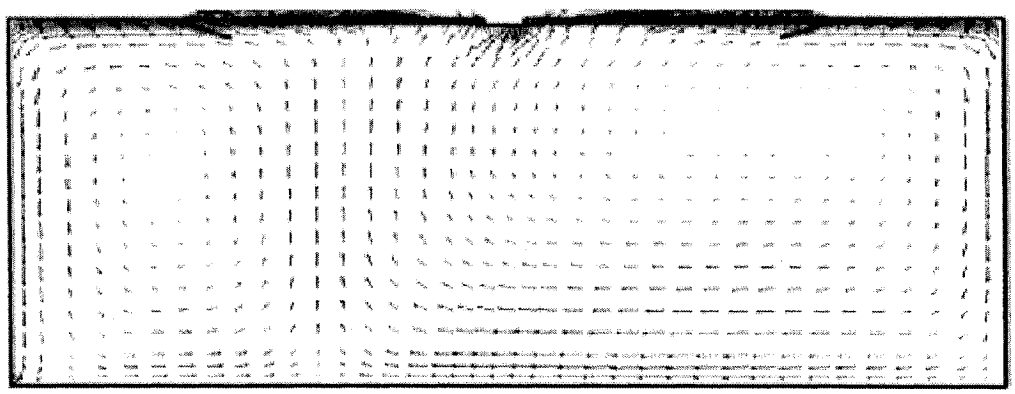

Figure 4.8 Flow pattern predicted by CFD for Re = 2210, Case III.

A qualitative verification was also done with other CFD predictions from the literature to show the similarity of the indoor airflow pattern for a given inlet position in an isothermal room. For this purpose, the CFD predictions of Chen and Xu (1998) were selected. They used an isothermal room with dimensions of L/H = 3.0, h_0 = 0.056H, outlet width = 0.16H (located at the bottom of the wall opposite to the inlet side) and Re = 4773. They employed the indoor zero–equation and the standard k-ε turbulence models. Their CFD airflow pattern predictions are depicted in Figures 4.9 and 4.10. Both airflow patterns are similar to Figure 4.6. Therefore, such similarity of airflow pattern for the same diffuser type and location but different room, inlet and outlet dimension could be an indication that some general pattern for the variation of the flow coefficient can be obtained for isothermal forced convection.

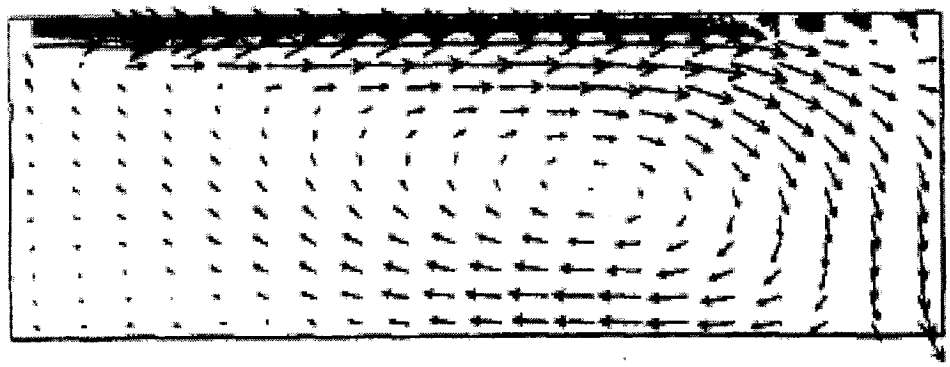

Figure 4.9 CFD flow field prediction using indoor zero-equation turbulence model and 20x18 grids (Chen and Xu, 1998).

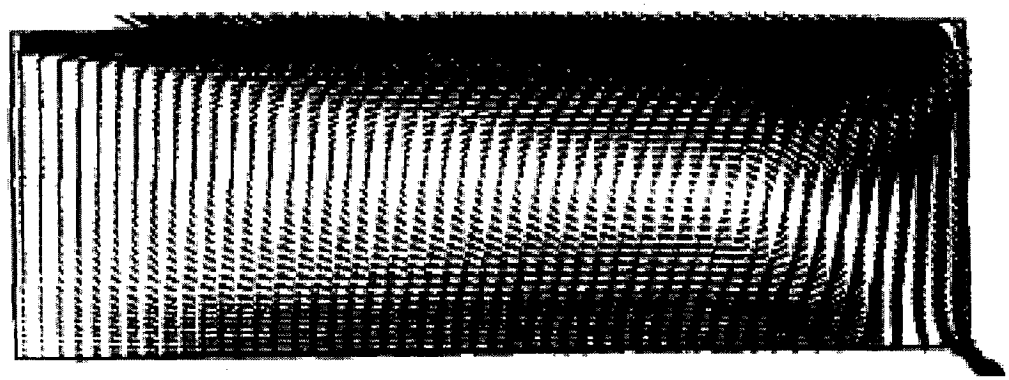

Figure 4.10 CFD flow field prediction using k-ε turbulence model and 50x45 grids (Chen and Xu, 1998).

Furthermore, the CFD predictions for Case I were compared with experimental data from Nielsen (1998). Figures 4.11 and 4.12 depict the comparisons at two vertical positions: x = 1m and x = 3m, respectively. The CFD prediction follows the measured air velocity profile at both vertical sections in the room. Good agreement between predicted and measured air velocities were also obtained at a given height.

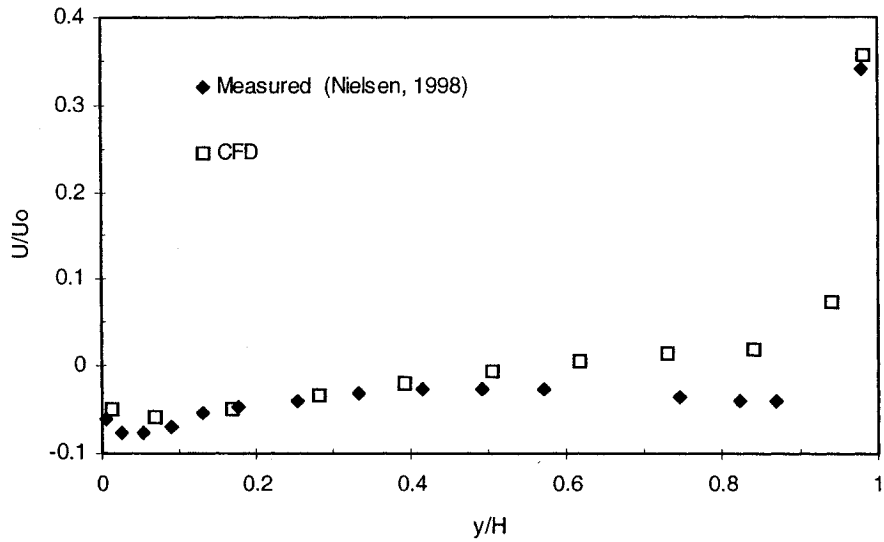

Figure 4.11 Comparison of CFD prediction with experimental data at x = 1m, Case I.

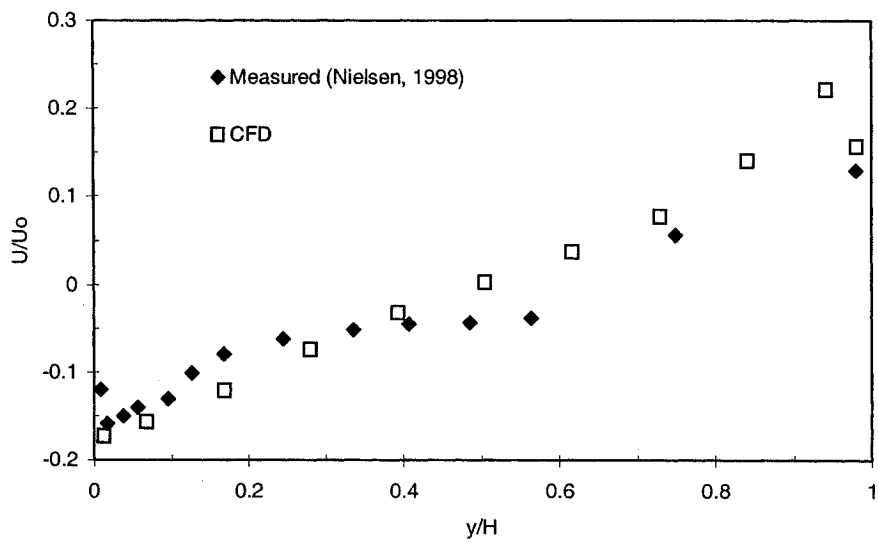

Figure 4.12 Comparison of CFD prediction with experimental data at x = 3m, Case I.

In summary, the verification of the predicted magnitude of air velocity and airflow pattern in this subsection shows that the CFD predictions of this study were reliable

enough to be used for further analysis such as estimation of the flow coefficient for each cell in the standard zone.

4.2.3 Estimation of the flow coefficient

After the pressure and air velocity distributions were obtained from CFD simulation, the next steps were:

- Discretization of room into a smaller number of cells, which are less than that used for CFD simulation and estimating the K values of each cell in the x and y directions;
- Analyzing the results of the estimation with due consideration to the distribution of absolute values of K and their average in the room; and
- Examining the influence of the number of cells on the K value and the possibilities of obtaining parametric equations for K.

4.2.3.1 Discretization of the room and estimation of K

For the estimation of K values, the room was divided into 11x11, 9x9, and 11x11 cells, for Cases I to III, which are about half the number of cells used for the respective CFD simulations. This is a reasonable number as far as the zonal models are concerned. The cells and the vertical positions used for the estimation are shown in Figure 4.13. Moreover, as shown in Figure 4.14, for any cell j the flow coefficients for the horizontal airflow (K_x) and for vertical airflow (K_y) were separately estimated using the components of the velocity and pressure differences in the respective directions.

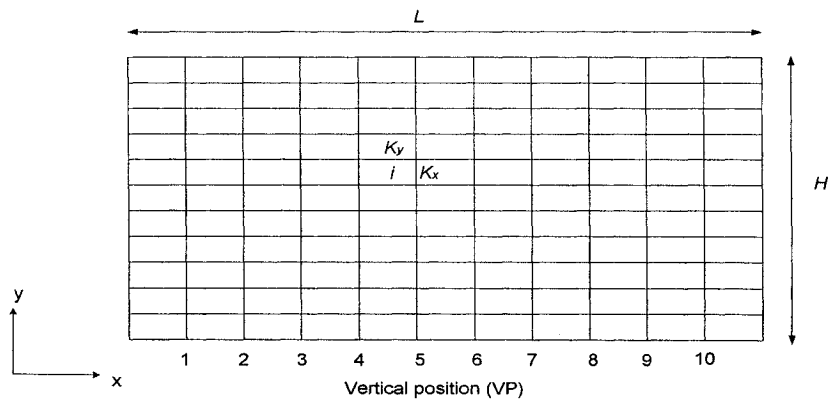

Figure 4.13 Division of the room into 11x11 cells for the estimation of K_x and K_y, Case I.

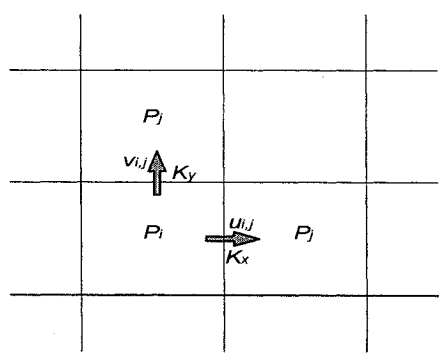

Figure 4.14 Estimation of K_x and K_y for cell j.

4.2.3.2 Results and discussions

The variations of the K values along the vertical positions shown in Figure 4.13 were used to present the estimated K_x and K_y values for the three cases. For example, for Case I, ten vertical positions shown in Figure 4.13 were directly used for K_x but eleven vertical positions through the cell centers were used for K_y since the zonal method employs the staggered grid structure (see Figure 4.14).

1. Distribution of K_x and K_y

Since the room was isothermal and the trends were similar for other values of *Re*, the estimated values for *Re* = 2210 were selected to demonstrate the variation of K_x and K_y as a function of dimensionless height of the room (*y/H*). The distributions are depicted in Figures 4.15 and 4.16 for Case I; in Figures 4.17 and 4.18 for Case II; and in Figures 4.19 and 4.20 for Case III. The distributions of K_x and K_y values depend on the type and location of the diffuser. Generally, comparing the distributions of K_x and K_y for all cases, it can be observed that the value of K_x increases away from the mid-height; whereas the value of K_y increases towards the mid-height of the room. The difference between the maximum and minimum values increases away from the mid-height for K_x and decreases for K_y. This shows that the error in using the constant value of $K = 0.83$ increases away from the mid-height for the horizontal airflow and decreases away from the mid-height for the vertical airflow.

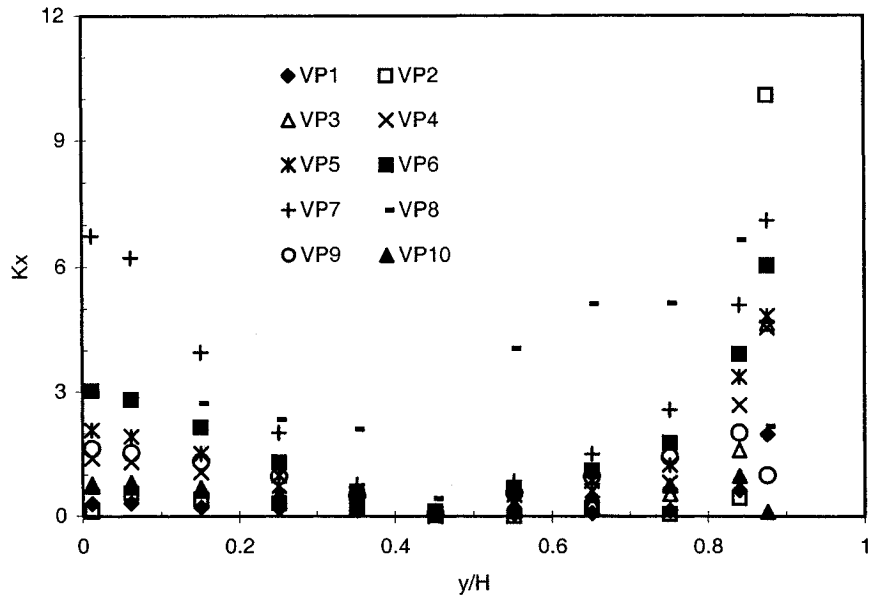

Figure 4.15 Distribution of K_x for slot inlet at ten vertical positions (VP), Case I.

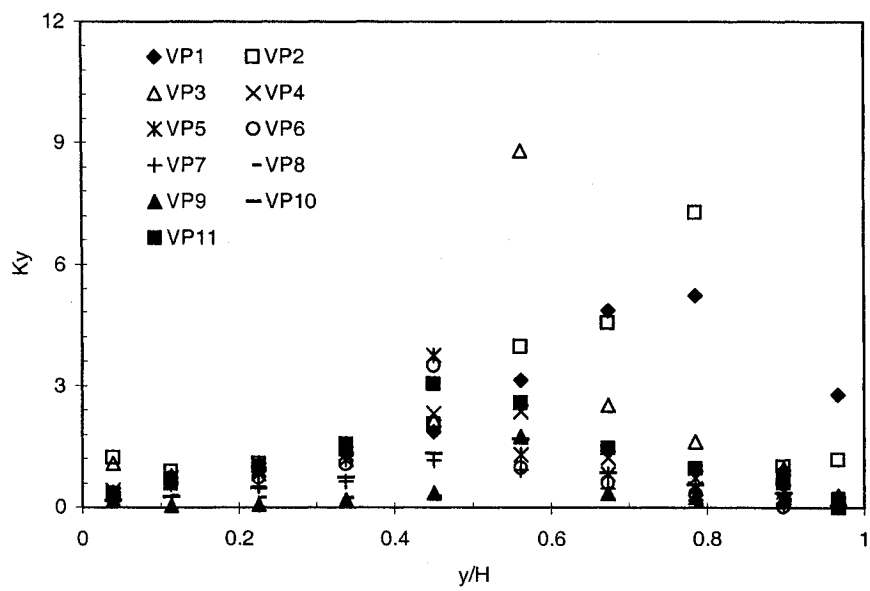

Figure 4.16 Distribution of K_y for slot inlet at eleven vertical positions (VP), Case I.

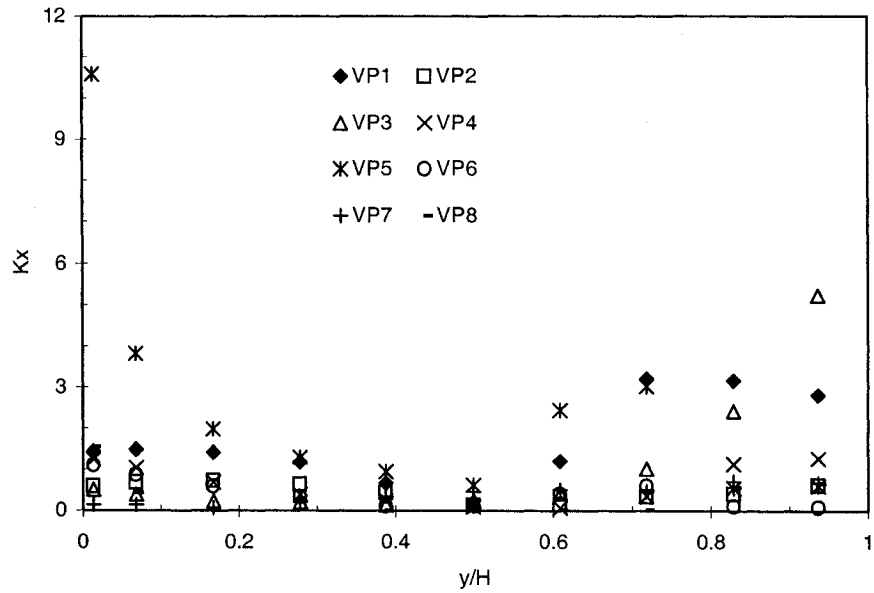

Figure 4.17 Distribution of K_x for grille inlet at eight vertical positions (VP), Case II.

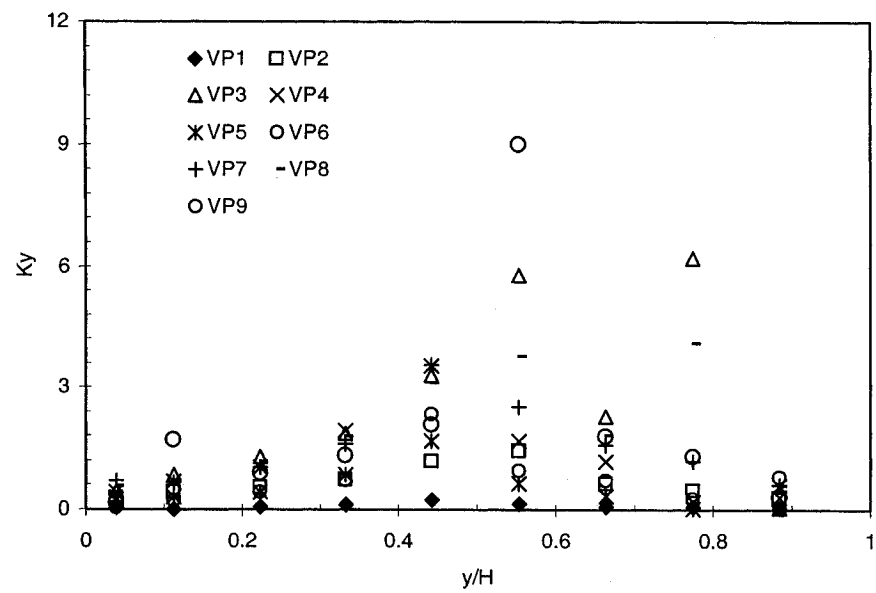

Figure 4.18 Distribution of K_y for grille inlet, at nine vertical positions (VP), Case II.

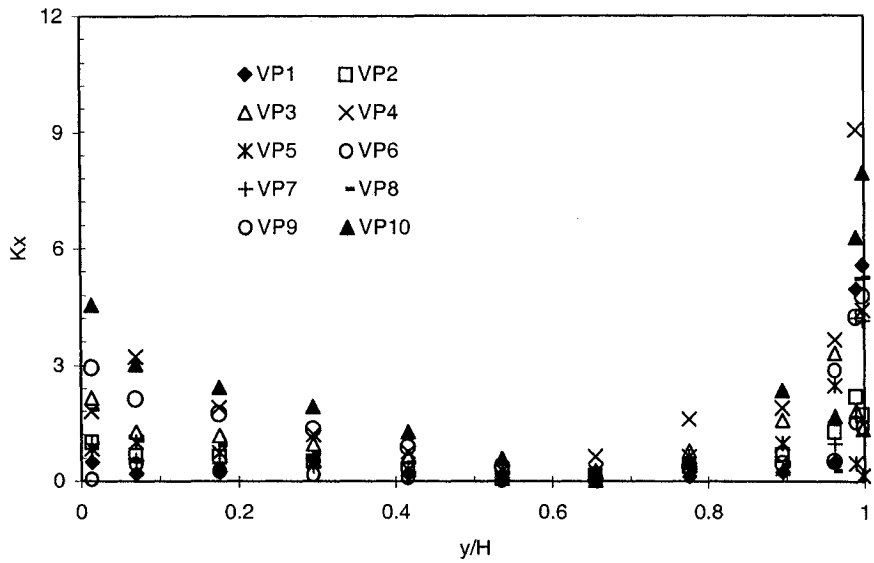

Figure 4.19 Distribution of K_x for ceiling diffuser at ten vertical positions (VP), Case III.

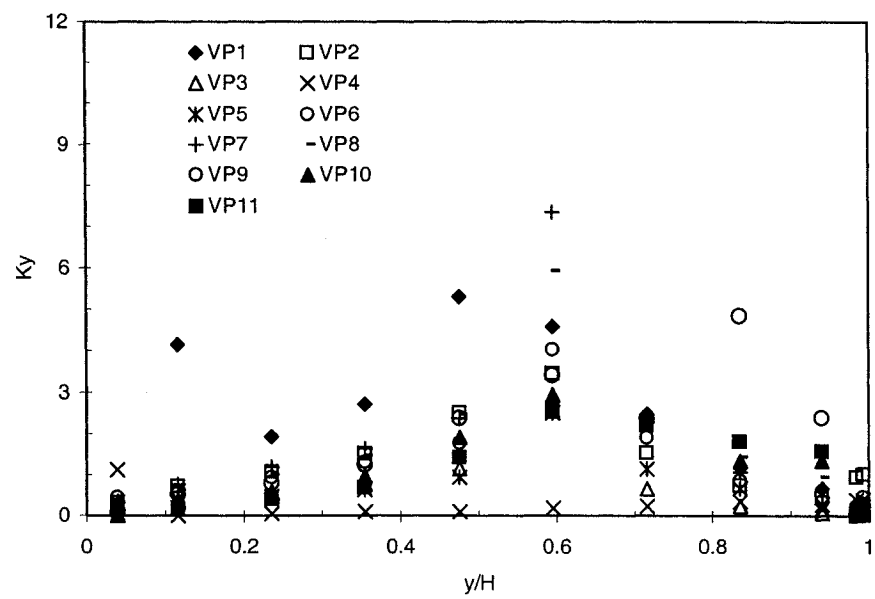

Figure 4.20 Distribution of K_y for Ceiling diffuser at eleven vertical positions (VP), Case III.

2. Influence of Re on the distribution of average K_x and K_y

In order to examine the influence of *Re* K_x and K_y, the values of K_x and K_y at the same height (*y/H*) were averaged and these average K_x and K_y values were assigned for all cells at that height. Note that the points discussed below should be seen from the perspective of the distributions in Figures 4.15 to 4.20 since at any height *y/H*, the values of K_x and K_y show variability even for the same *Re*.

The average K_x and K_y values as a function of *y/H* for the five Reynolds numbers are depicted in Figures 4.21 to 4.26. It can be seen that the variation of K_x and K_y as a function of *y/H* depends on the type and location of the diffuser and for all *Re* values, the variations of K_x and K_y show similar trends for the respective diffusers.

Figures 4.21 and 4.22 depict the average K_x and K_y values for slot diffuser. In Figure 4.21, as one traverses from the floor to the ceiling, the average K_x value first decreases from the floor to the mid-height of the room and then starts to increase from the mid-height to the ceiling. The variation of K_x could be due to the formation of recirculation in the room. The recirculation could make the average horizontal velocity increase away from the center of the recirculation, which results in a higher average pressure drop around the center than away from it. Therefore, in line with Equation 3.4, the average of K_x in the PLM has to decrease towards the center and increase away from it. Unlike K_x, K_y (see Figure 4.22) increases towards the mid-height of the room. This could be due to the decrease in the average vertical velocity away from the center of the recirculation and the corresponding increase in pressure drop.

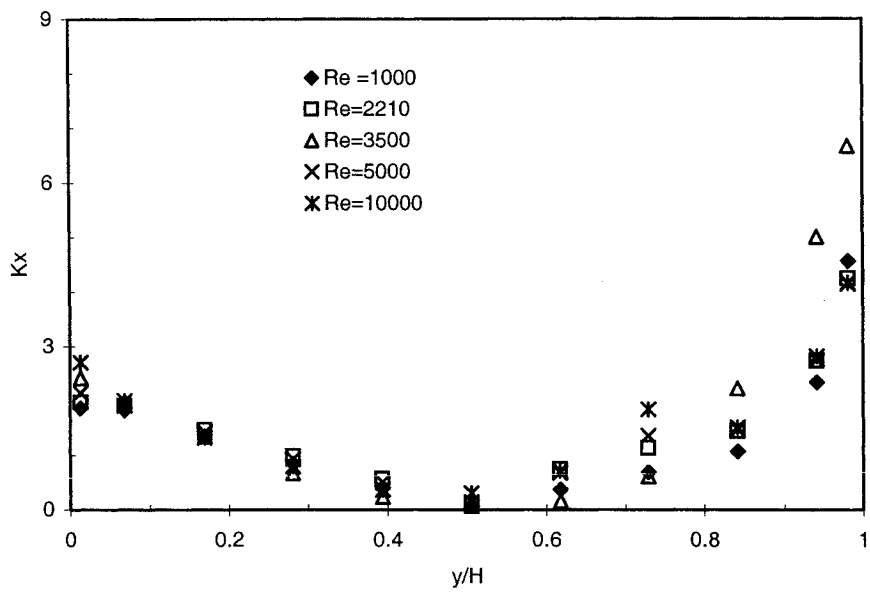

Figure 4.21 Distribution of average K_x for slot inlet, Case I.

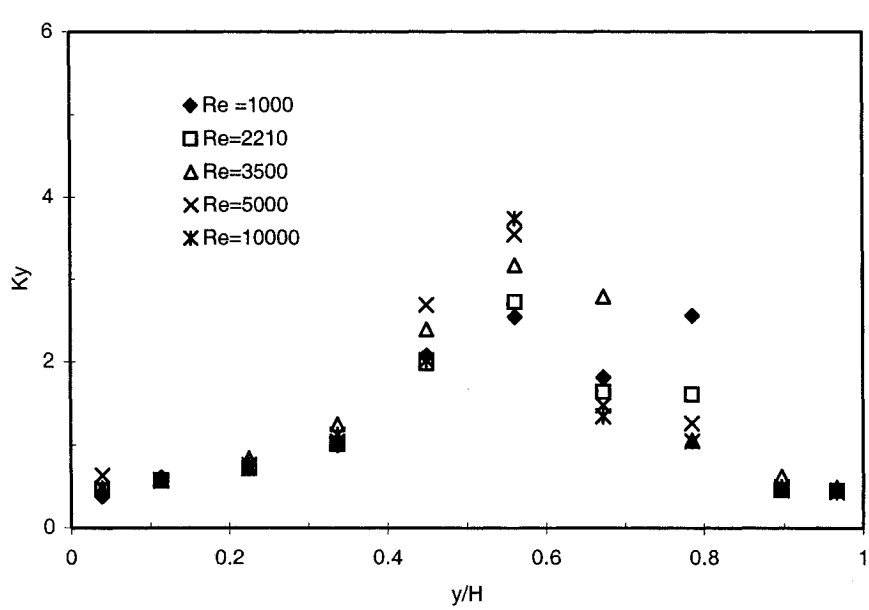

Figure 4.22 Distribution of average K_y for slot inlet, Case I.

The variation of the average K_x and K_y values for a grille diffuser are shown in Figures 4.23 and 4.24, respectively. Like Case I, the variations of K_x and K_y show similar trend for all *Re*. In Figure 4.23, K_x first decreases from the floor up to the mid-height of the room and then starts to increase from the mid height to the ceiling. But K_y, in Figure 4.24, increases towards mid-height from the floor, and decreases from the mid-height to the ceiling. Figures 4.25 and 4.26 show the estimated average values of K_x and K_y for ceiling diffuser, respectively. In this case, the minimum and the maximum values for K_x and K_y are shifted towards the ceiling compared to the slot diffuser (see Figures 4.21 and 4.22), since the centers of the recirculation zones are moved towards the ceiling (see Figure 4.8).

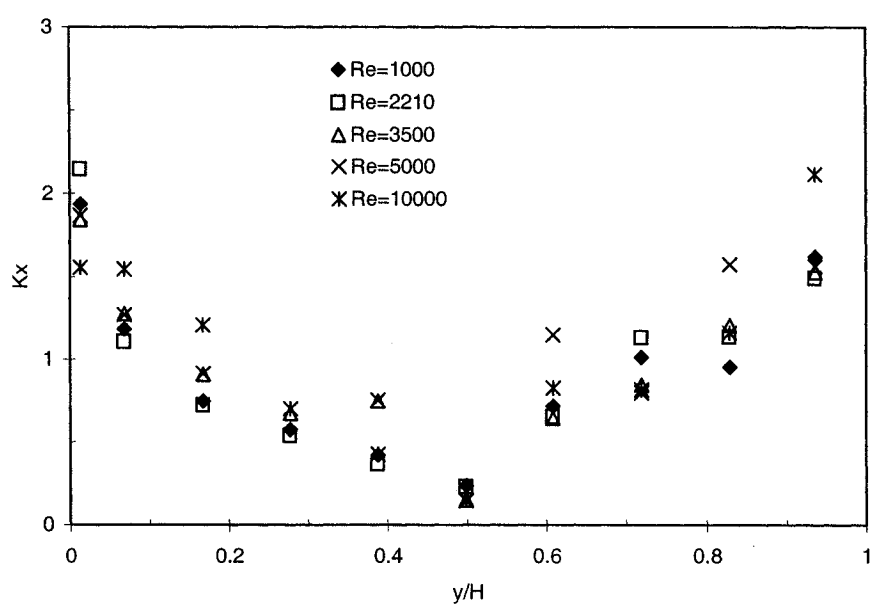

Figure 4.23 Distribution of average K_x for grille diffuser, Case II.

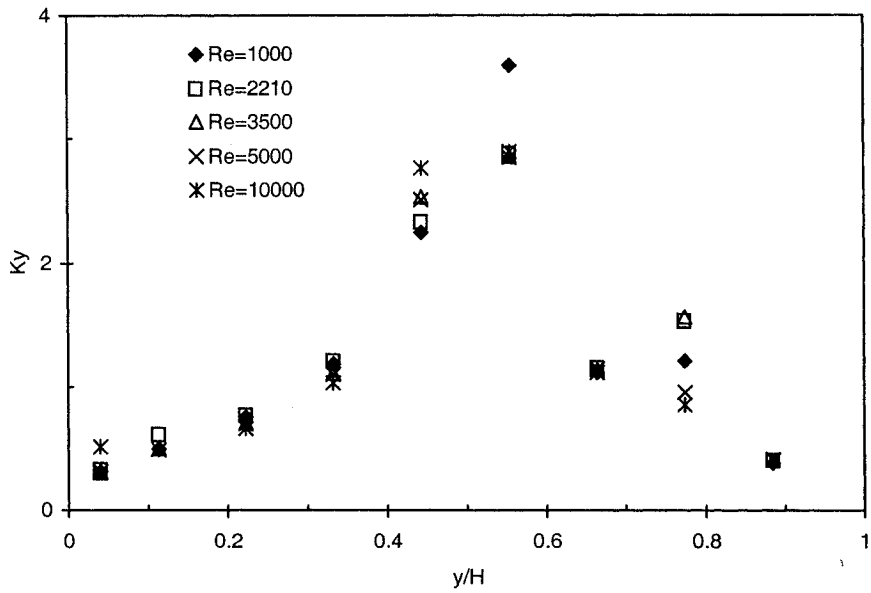

Figure 4.24 Distribution of average K_y for grille diffuser, Case II.

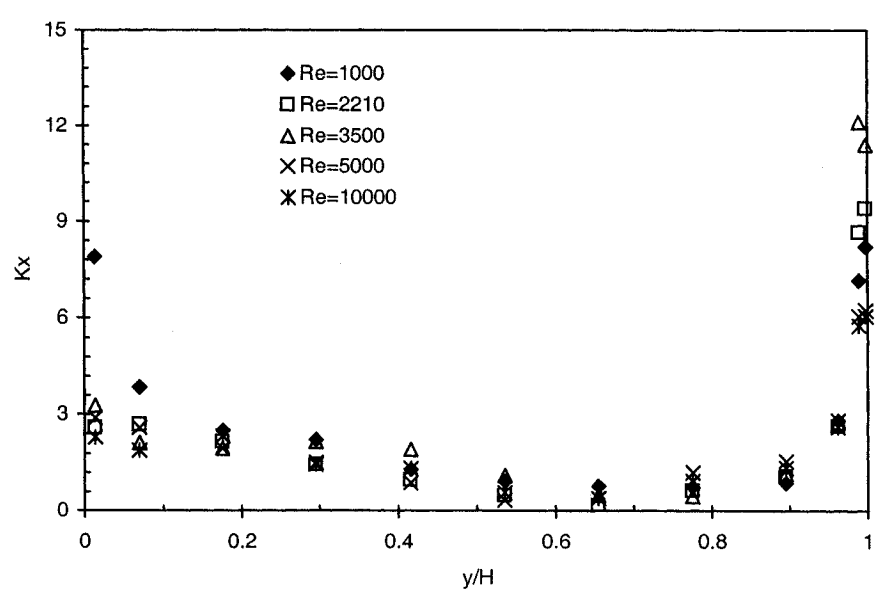

Figure 4.25 Distribution of average K_x for ceiling diffuser; Case III.

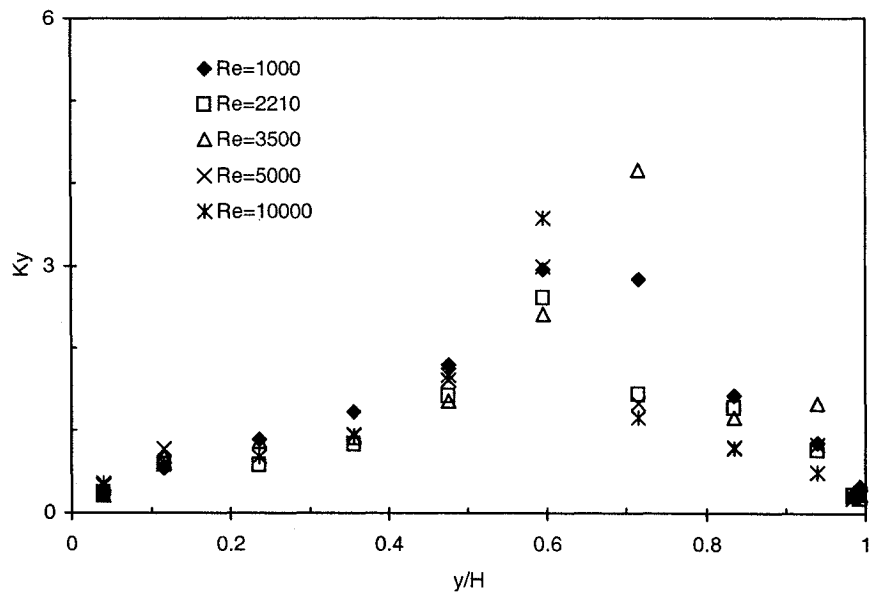

Figure 4.26 Distribution of average K_y for ceiling diffuser, Case III.

4.2.3.3 Further on the variability of K_x and K_y

This subsection presents further investigations made on the practicality of implementing the PLM with variable K for the prediction of indoor airflow distribution. This was done considering:

- the influence of the number of cells used for the estimation of K_x and K_y; and
- the effect of using parametric equations for K_x and K_y as a function of y/H.

1. Influence of number of cells on K_x and K_y

In order to examine the influence of the number of cells on the values of K_x and K_y, Case I, slot inlet at Re = 2210 was selected. In subsection 4.2.3.2 K_x and K_y were estimated using 11x11 cells for the slot diffuser. Here, the reduction of the number of cells was done in the x-direction for K_x and in the y-direction for K_y. Therefore; the number of cells

used for the estimation of K_x and K_y in Figures 4.15 and 4.16 was reduced to 6x11 and 11x6 for the estimation of K_x and K_y, respectively. Figure 4.27 shows the cells and the vertical positions used for the estimation. The distribution of K_x and K_y estimated using the reduced number of cells is depicted in Figures 4.28 and 4.29. Comparing Figure 4.28 with Figure 4.15; and Figure 4.29 with Figure 4.16, it can be discerned that the general pattern is not affected. The value of K_x increases away from the mid-height whereas the value of K_y increases towards the mid-height of the room. The difference in values could be attributed to the shifting of the location of the vertical positions.

To examine the possibility of generalizing the variability of K_x and K_y for any number of cells, the average values of K_x and K_y obtained using 11x11cells and the reduced cells were compared. It can be seen from Figures 4.30 and 4.31 that the trends are the same but there are differences in the average values of K_x and K_y since the number of cells in the y-direction was decreased for K_y (in Figure 4.30 the values of K_y for 11x11 and 11x6 are at different heights). Noting these differences in values and the general trend, it could be possible to relate the variation of K_x and K_y with the dimensionless height (y/H) for a given inlet location.

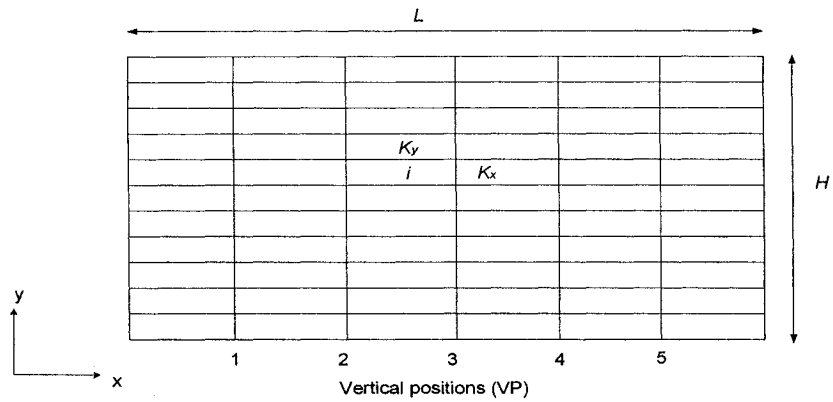

Figure 4.27 Division of the room into 6x11 cells for the estimation of K_x and K_y, Case I.

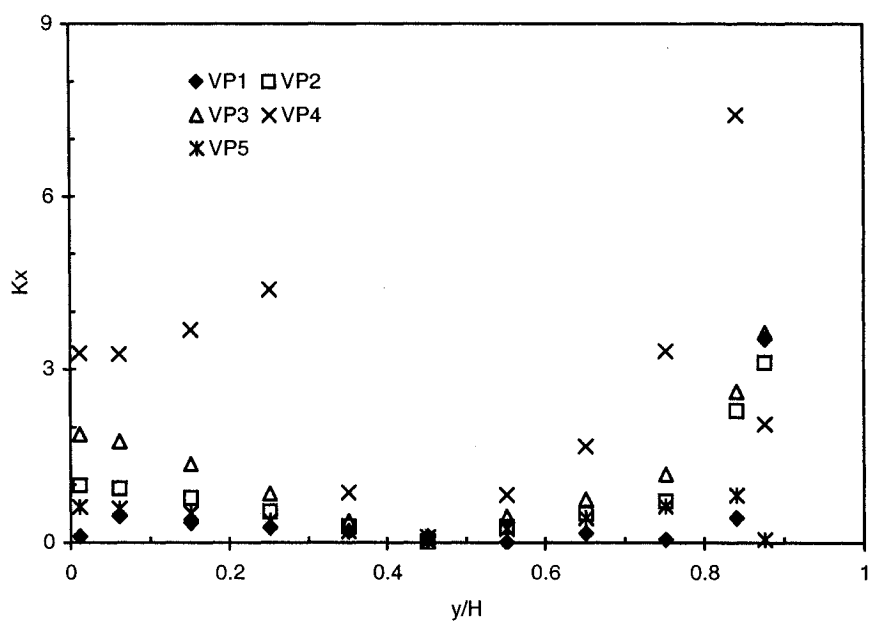

Figure 4.28 Distribution of K_x for slot inlet, Case I.

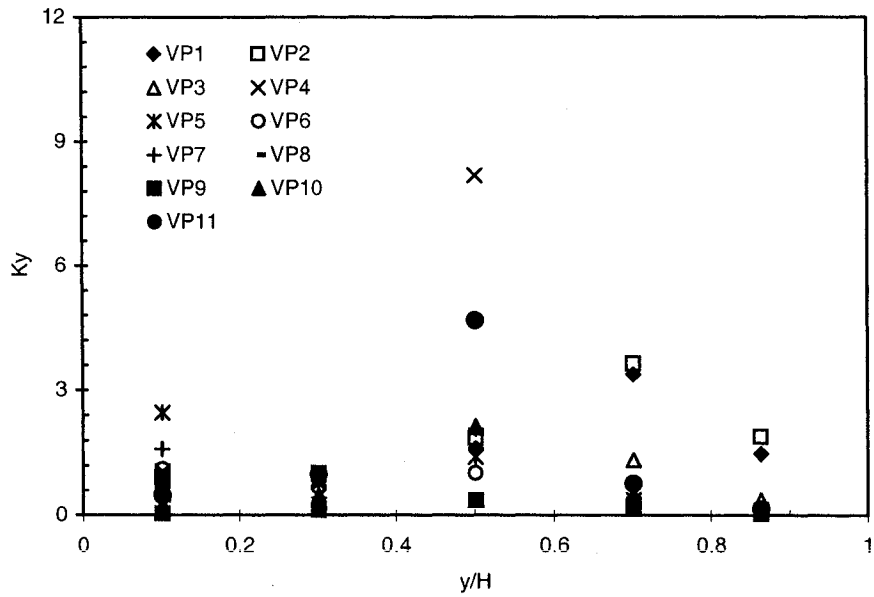

Figure 4.29 Distribution of K_y for slot inlet, Case I.

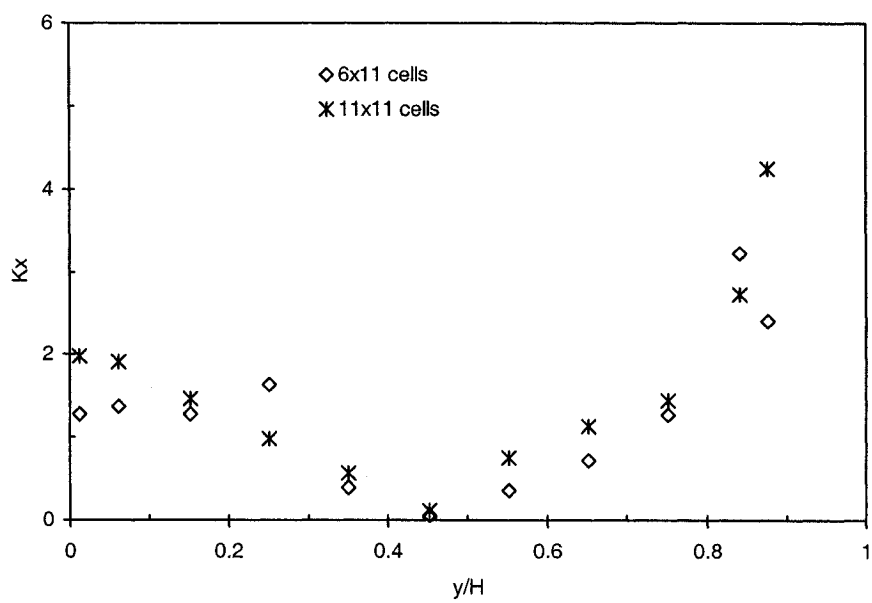

Figure 4.30 Average K_x for slot inlet, Case I.

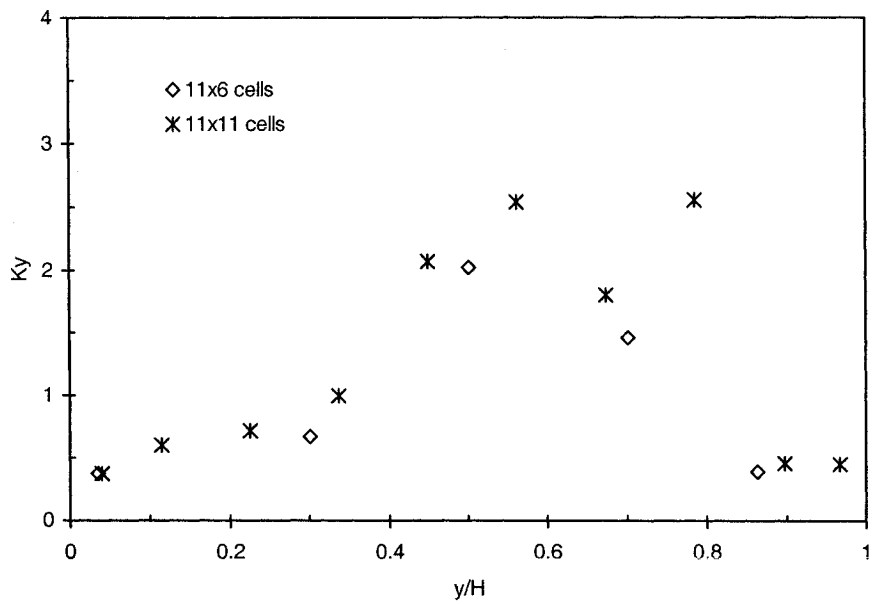

Figure 4.31 Average K_y for slot inlet, Case I.

2. Equations for K_x and K_y

The above discussion reveals the possibility of obtaining general relations for K_x and K_y. For the purpose of comparison, two versions of the PLM were first identified:

- PLM with variable K (PLMK): the distribution of the K_x and K_y from Figures 4.15 to 4.20, were directly utilized.
- PLM with variable K where K is a function of y/H ($PLMK_{func}$): the variation of K_x and K_y as a function of y/H was obtained using the average values from Figures 4.21 to 4.26. It can be seen that a second-degree polynomial could be used as a general equation to approximate the average value of K:

$$K = a\left(\frac{y}{H}\right)^2 + b\left(\frac{y}{H}\right) + c \tag{4.3}$$

where

a, b, and c are coefficients specific to the type and location of the diffuser.

The slot diffuser (Case I), for Re = 2210 and 11x11 cells, was selected for comparison of the airflow predictions of the PLM, the PLMK, and the $PLMK_{func}$. For the PLM, since other values of K were found to make no difference in the predition K = 1.0 was used (see Section 4.1). For the PLMK, all the K_x and K_y values estimated for 11x11cells, shown in Figures 4.15 and 4.16, were directly applied. For the $PLMK_{func}$, the coeffients in Equation 4.3 were estimated by correlating the average values in Figures 4.21 and 4.22. The coefficients a, b, and c for Case I are given in Table 4.1. The comparison of the predicted air velocity profiles at two vertical sections in the room are depicted in Figures 4.32 and 4.33.

Table 4.1 Values of coefficients for Equation 4.3, Case I.

	a	b	c	r^2	Range
K_x	0	-4.81	2.25	0.99	$0< y/H <0.5$
	0	4.28	-2.05	0.99	$0.5 <y/H <1.0$
K_y	14.42	-3.12	0.65	0.98	$0 <y/H <0.5$
	9.13	-20.51	11.71	0.98	$0.5 <y/H <1.0$

In Figures 4.32 and 4.33, the PLMK follow the trend of the measured velocity profile better than the $PLMK_{func}$ and the PLM. The predictions of the PLMK are very close to the measured ones at x = 1m than x = 3m. This shows that the discrepancy of using variable K, in the PLMK and the $PLMK_{func}$, increases as one moves towards the recirculation zone. This is further illustrated using the airflow pattern predictions of the

three models in Figures 4.34 to 4.36. Comparing these figures with Figure 4.6, it can be observed that the airflow patterns predicted by the PLMK and the $PLMK_{func}$ show the tendency to form recirculation.

The PLMK improved the predicted magnitude of the air velocity compared to the PLM, and the $PLMK_{func}$. The airflow patterns show the difficulty of predicting the recirculation using the PLMK and the $PLMK_{func}$. The discrepancy of the $PLMK_{func}$ indicates that the difficulty of generalizing the distribution of K_x and K_y. Nevertheless, the results justify the fact that K could not have one value for all cells.

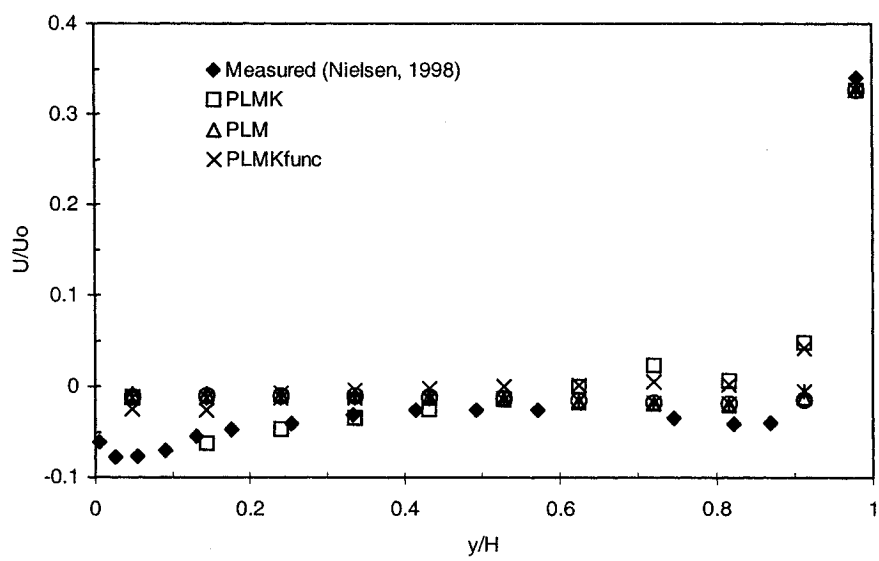

Figure 4.32 Comparison of velocity profiles predicted by PLMK, PLM and $PLMK_{func}$ at x = 1m, Case I.

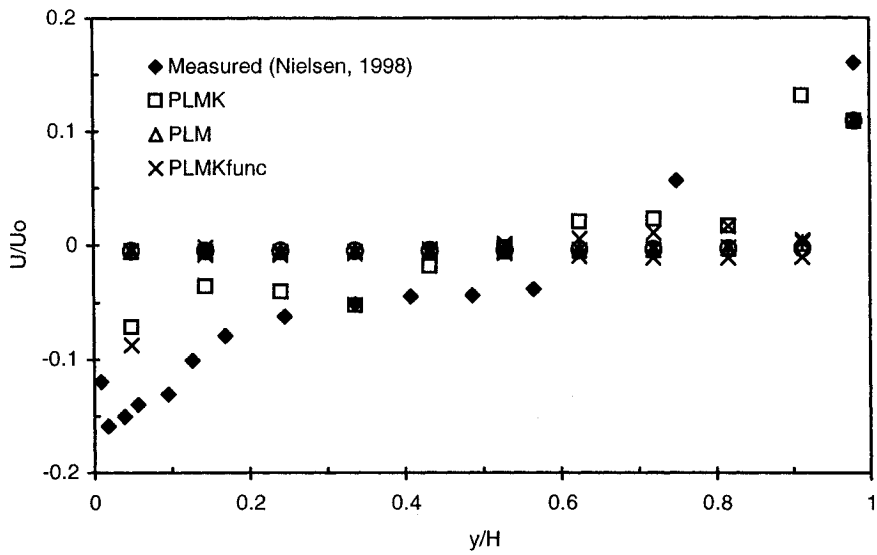

Figure 4.33 Comparison of velocity profiles predicted by PLMK, PLM and $PLMK_{func}$ at x = 3m, Case I.

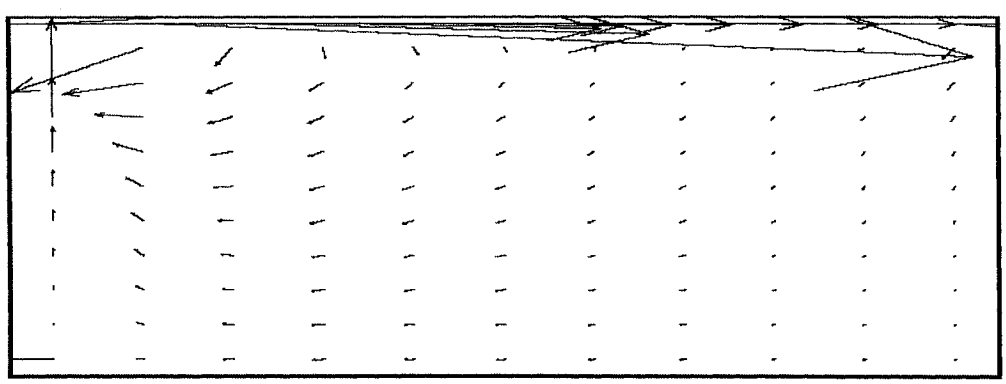

Figure 4.34 Airflow pattern predicted by the PLM, Case I.

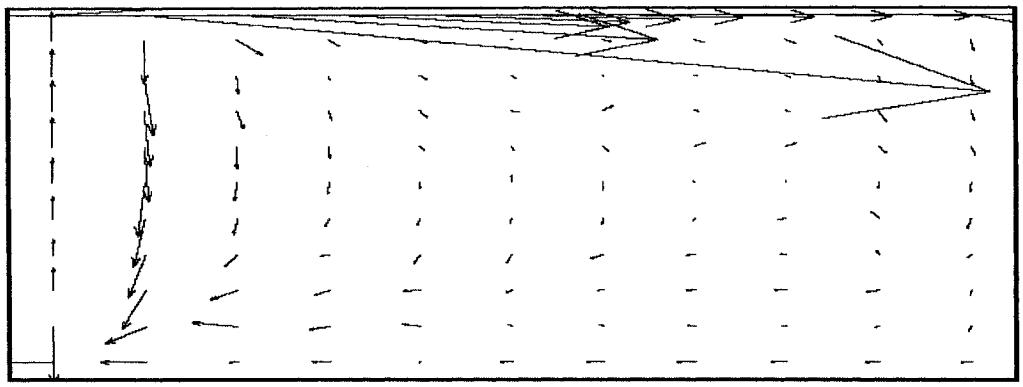

Figure 4.35 Airflow pattern predicted by the PLMK, Case I.

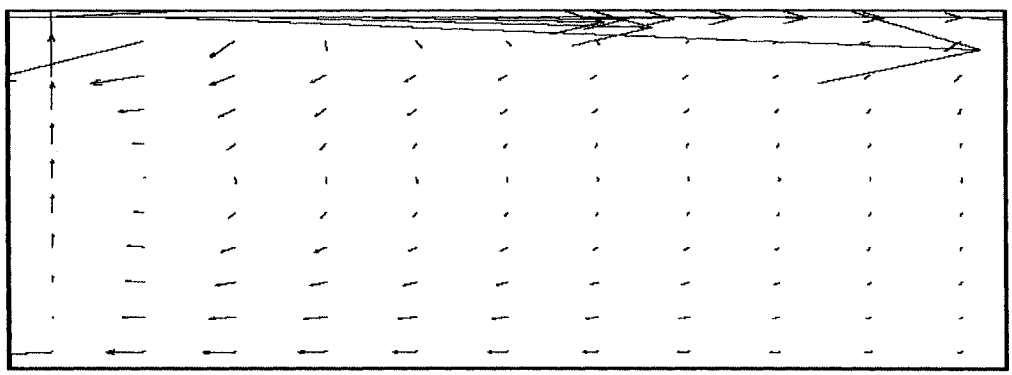

Figure 4.36 Airflow pattern predicted by the $PLMK_{func}$, Case I.

4.2.4 Concluding remarks on the flow coefficient

- Using the same K value for all cells could not improve the prediction capability of the PLM.
- The application of CFD for the estimation of the flow coefficient has provided a new version of the PLM, the PLMK, which is found to give better prediction than the PLM.

- The use of different K value for each cell could improve the magnitude of the predicted velocity. But the difficulty of generalizing the distribution of K_x and K_y implies that in order to estimate appropriate K_x and K_y for each cell, one needs to run a new CFD simulation for the particular case, which is an unnecessary complication.
- Although the PLMK prediction of the airflow pattern is better than the PLM more improvement is needed, which indicates that the prediction of recirculation in the standard zone calls for other possible ways for the modification of the PLM.

4.3 Combining the PLM and the SDM

The difficulty of generalizing the PLMK and the $PLMK_{func}$, coupled with the discrepancies of the SDM and the PLM predictions, has led to the pursuit of the other methodology for the improvement of the PLM - combining the PLM and the SDM. The two strategies employed for combining the two models are the direct and the indirect combinations. For the direct combination, the pressure difference $\Delta P_{i,j}$ and the mass flow rate $m_{i,j}$ in the SDM and the PLM were added to get the total pressure drop and mass flow rate between two cells. For the indirect combination, however, an analogy of fluid flow between parallel plates was employed to modify and combine the SDM with the PLM.

4.3.1 The direct combination

The first direct combination of the PLM and the SDM leads to the following general relation for the zonal models:

$$\Delta p_{i,j} = am_{i,j}^2 + bm_{i,j} \tag{4.4}$$

Where a and b are coefficients given in Table 4.2 for the combined zonal models:

- The surface-drag-power-law Type 1 (SD-PLM1); and
- The surface-drag-power-law Type 2 (SD-PLM2).

The second direct combination gives the surface-drag-power-law model Type 3 (SD-PLM3):

$$m_{i,j} = a\Delta p_{i,j}^{0.5} + b\Delta p_{i,j} \tag{4.5}$$

Where a and b are the coefficients listed in Table 4.2.

In Table 4.2, the other models presented in the general form, Equation 4.4, are:

- The PLM (Equations 3.4 and 3.5);
- The PLMK and the $PLMK_{func}$;
- The surface-drag flow model Type 1 (SDM1), Equation 3.17; and
- The surface-drag flow model Type 2 (SDM2), Equation 3.18.

Table 4.2 Values of coefficients in Equations 4.4 and 4.5.

Model	a	b
Power-law (PLM)	$\frac{1}{2K^2A^2\rho}$	0
Power-law with variable K (PLMK or $PLMK_{func}$)	$\frac{1}{2[K(y/H)]^2A^2\rho}$	0
Surface-drag Type1 (SDM1)	0	$\frac{\mu_e\pi^2\Delta x}{4\rho Y^2A}$
Surface-drag Type2 (SDM2)	$\frac{2\lambda\kappa^2a^3\Delta x}{\rho A^2\Delta y}$	0
Surface-drag-power-law Type 1 (SD-PLM1)	$\frac{1}{2K^2A^2\rho}$	$\frac{\mu_e\pi^2\Delta x}{4\rho Y^2A}$
Surface-drag-power-law Type 2 (SD-PLM2)	$\frac{2\lambda\kappa^2a^3\Delta x}{\rho A^2\Delta y}+\frac{1}{2K^2A^2\rho}$	0
Surface-drag-power-law Type 3 (SD-PLM3)	$KA\sqrt{2\rho}$	$\frac{4\rho Y^2A}{\mu_e\pi^2\Delta x}$

Similar equations, like Equations 4.4 and 4.5, with different coefficients were also developed for airflow through cracks and orifices (Etheridge, 1998; Chiu and Etheridge, 2002). The similarity is not a coincidence given the fact that the power-law equation commonly used in the zonal models was originally development for airflow through cracks and large openings. Moreover, the linear and the nonlinear terms in Equation 4.5 are also used independently for the implementation of the PLM (Haghighat et al. 2001). The linear term is invoked at smaller pressure differences whereas the non-linear is invoked at higher ones.

4.3.1.1 Case description

The isothermal room with slot inlet used for Case I (Nielsen, 1998) was selected. The room was divided into 11x11 cells in order to directly utilize the K_x and K_y values for the PLMK.

4.3.1.2 Results and discussions

Since value of K has no impact on the predictions of the PLM, the value of K for all combined models in Table 4.2 with $a \neq 0$ was set to 1.0 for all cells in the standard zone. The SDM1 and the SD-PLM2 were not included in the comparison. This is because the linear SDM1 is similar to the power-law for smaller pressure differences. Moreover, Axley (2001) has suggested that the linear SDM1 can only serve as a preliminary solution, which can be used as initial guess for the nonlinear SDM2. The combined SD-PLM2 is simply the PLM with value of K other than 1.0, which has made no impact on the predictions of the air velocity (see Section 4.1).

Simulations were conducted to compare the prediction capabilities of the combined models in the standard zone. Equation 3.21 was used to evaluate the airflow for cells in the air jet zone and the airflow in the standard zone was calculated by the PLM, the SD-PLM1, the PLMK, the SDM2, and the SD-PLM3. Figures 4.37 and 4.38 depict the comparison of the predicted dimensionless velocity (U/U_0) profile for Re = 2210. It can be observed that at vertical position x = 1m from the inlet, the predictions of all the models except the PLMK do not show any tendency to follow the experimental profile. For all models, the magnitudes of the predicted velocities show discrepancies compared

to measured values except in the specific zone ($y/H > 0.9$) due to the use of Equation 3.21. The discrepancy becomes more pronounced as one traverse towards the middle of the room to a vertical position of x = 3m (see Figure 3.38). Also, all the models except the PLMK do not show any tendency to follow the measured values and predicted low velocity in the standard zone. This indicates that the discrepancies of the predictions of the zonal models become more apparent as one moves towards the recirculation region. The PLMK seems to avoid this problem to a certain extent but as shown in Figure 4.35 it is not completely able to capture the recirculation.

In summary, the comparison of the selected models in this section has shown that the direct approach of combining the PLM and the SDM could not predict both the magnitude and the airflow pattern any better than the PLM. So far only the PLMK has given promising result in predicting the magnitude of the air velocity.

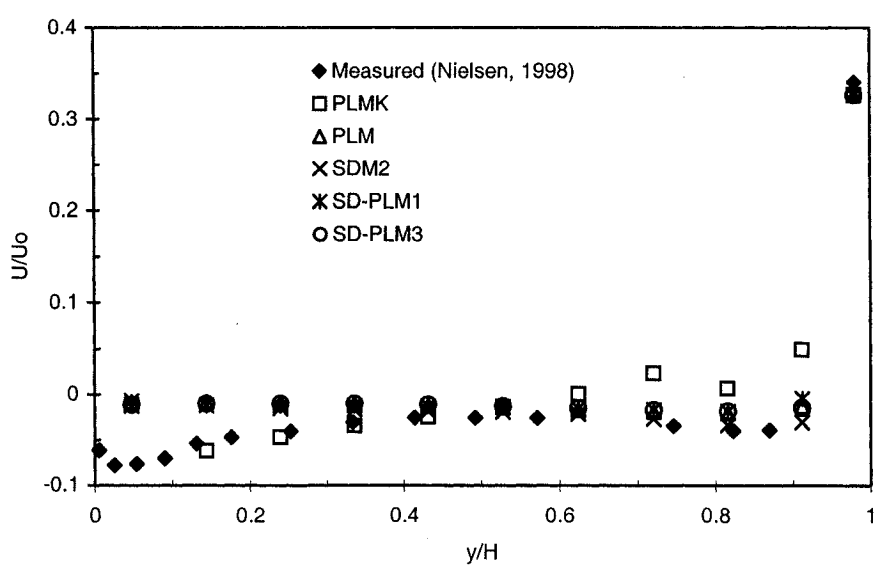

Figure 4.37 Comparison of the zonal models predictions with experiment at x = 1m.

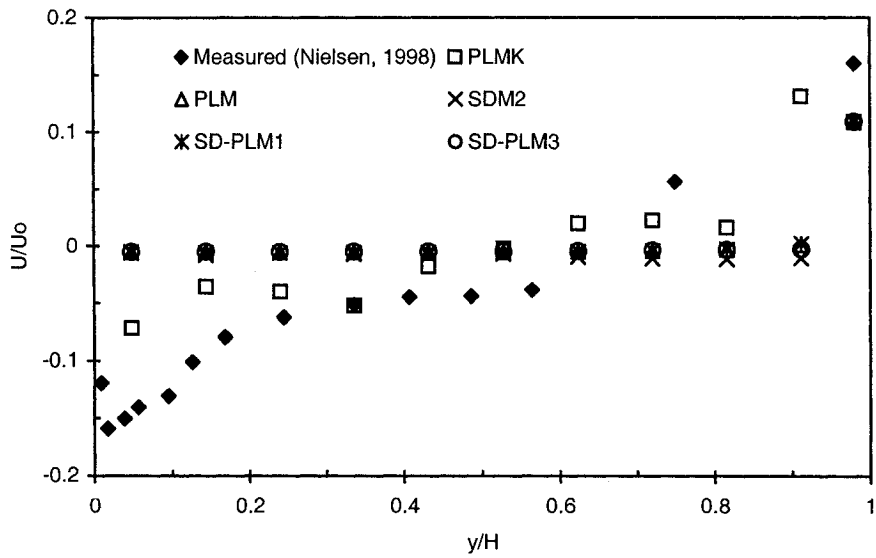

Figure 4.38 Comparison of the zonal models predictions with experiment at x = 3m.

4.3.2 The indirect combination

The development of new zonal models using the indirect combination can be initiated by observing closely the discrepancies pertaining to the SDM and the PLM. Consider the airflow pattern predicted by the PLM using Nielsen's (1998) geometry in Figure 4.34. The dominant flow is in the direction of the inlet velocity but the direction of the velocities in all the cells in the standard zone is reversed. As depicted in Figures 4.2 and 4.3 and confirmed previously by Haghighat et al. (2001) and Mora et al. (2003) for other room dimensions and inlet configuration, the magnitudes of the velocities predicted by the PLM for cells in the standard zone are very small compared to CFD predictions and experimental data. For the PLM (Equations 3.4 and 3.5), and the SDM (Equations 3.17 and 3.18) information of the flow is transmitted from cell to cell only through the

pressure in the flow direction. This produces back flow in all cells in the standard zone when the pressure gradient in the flow direction is negative.

To further clarify and facilitate the derivation of the new zonal model, the modified power-law model (MPLM), analogy of the PLM prediction in Figure 4.34 and the combined Couette-Poiseuille flow between plates in Figure 4.39 can be used.

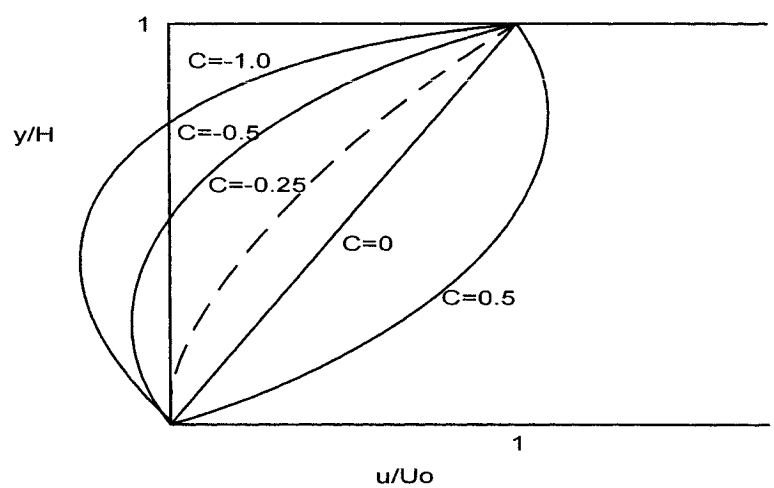

Figure 4.39 Velocity profile for combined Couette-Poiseuille flow between parallel plates (White, 1990).

The Couette-Poiseuille flow can be written as:

$$\frac{u}{U_0} = 0.5\left(1+\frac{y}{H}\right)+C\left(1-\frac{y^2}{H^2}\right) \tag{4.6}$$

where

u is the horizontal velocity at a distance y/H from bottom plate, m/s;

U_0 is the maximum velocity (at the top plate), m/s;

H is the gap height, m;

μ is the air viscosity kg/m.s;

ΔP is the pressure drop in the flow direction, Pa;

C is coefficient given by

$$C = \left(-\frac{\Delta P}{\Delta x}\right)\frac{H^2}{2\mu U_0} \tag{4.7}$$

The jet zone close to the ceiling in Figure 4.34 can be considered as analogous to the upper moving plate in Figure 4.39. Figure 4.39 shows that there is always a reverse flow in some part of the gap between the two plates when the dimensionless pressure C is less than -0.25 (White, 1990). In those parts, the negative pressure difference could be so dominant that it makes the first term in the right hand side of Equation 4.6 negligible. A similar situation occurs in all cells in the standard zone since the PLM does not take into account the influence of the driving jet in those cells. Therefore, the PLM prediction in the standard zone can be considered as similar to the extreme case of the Couette-Poiseuille, or simply the Poiseuille flow. As highlighted in Chapter 3, Axley (2001) used the latter with some modifications for the derivation of the SDM. Nevertheless, the SDM has not provided any improvement compared to the PLM.

The above discussion shows that in order to enhance the prediction capability of the PLM, the velocity in the dominant flow direction should not only depend on the pressure difference but also the magnitude of the maximum velocity at a vertical position. Therefore, to derive the modified power-law model (MPLM), Equations 3.4 and 3.5 were

modified to have the form of Equation 4.6. The MPLM can be given for x, and y direction as:

$$m_{x(i,j)} = K\Delta y l\left(2\rho_{i,j}(P_{i,j} - P_{i+1,j})\right)^{n_1} + \Delta y l \rho_{i,j} U_x \left(\frac{y}{H}\right)^{n_2} \tag{4.8}$$

$$m_{y(i,j)} = K\Delta x l\left(2\rho_{i,j}(P_{i,j} - P_{i,j+1})\right)^{1/2} \tag{4.9}$$

where

n_1 is the power-law exponent;

n_2 is the surface-drag exponent.

The MPLM is therefore a modified form of the Couette-Poiseuille equation. In the MPLM a room is considered as a number of connected parallel plates (ceiling and floor) each like in Figure 4.39. Unlike with the Couette-Poiseuille, in the MPLM the pressure gradients in the directions normal to the dominant flow are not zero and the pressure gradient in the dominant flow direction is not known a priori; it is rather a part of the solution. This makes the MPLM similar to "parabolized" Navier-stokes (PNS) in which strong pressure interaction and flow separation exists in the dominant flow direction (see Tennehill et al. 1997).

The introduction of the second term in Equation 4.8 makes sure that the influence of the driving air jet in the cells in the standard zone is taken into account. The influence of the air jet is only included in the dominant jet flow direction, which is x for horizontal inlet velocity and y for vertical inlet velocity. This makes the second term in Equation 4.8 to be known for all cells at the start of the solution for a given inlet condition.

Two possibilities were explored for the value of the velocity for each 'parallel plate' in a room. The first calculates the maximum velocity at the upper side (ceiling), U_x by using the air jet formula in Equation 3.21 as shown in Figure 4.40. The second uses a constant value of $U_x = U_0$ as depicted in Figure 4.41.

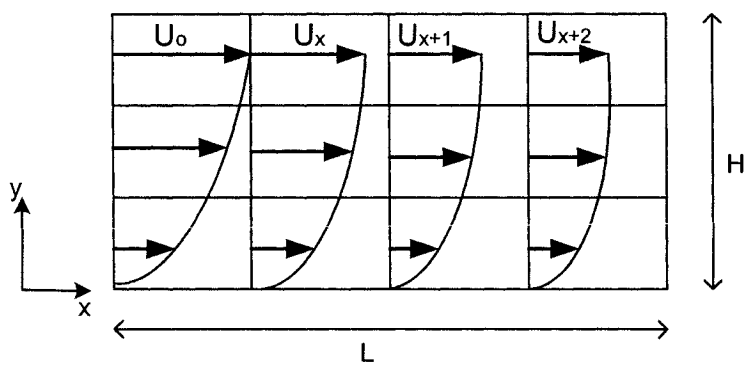

Figure 4.40 Velocity profile for the second term in Equation 4.8. U_x calculated by Equation 3.21.

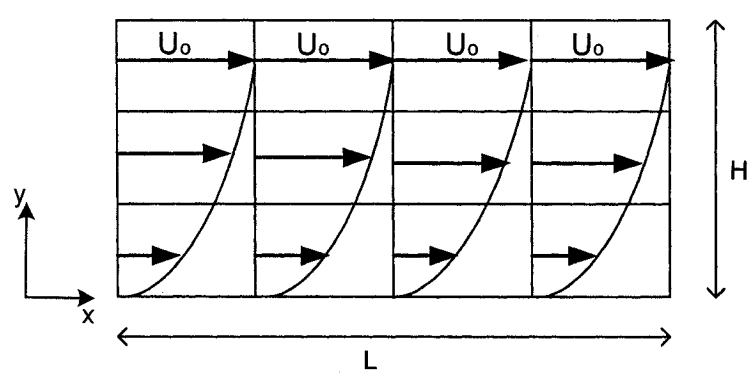

Figure 4.41 Velocity profile for the second term in Equation 4.8. $U_x = U_0$.

Simulations were then conducted for an isothermal room with two-dimensional slot inlet (Nielsen, 1998) shown in Figure 4.1. The exponents, n_1 and n_2 in Equation 4.8, were given values of 0.5 and 2, respectively (refer Sections 4.4.1.1 and 4.4.1.2 for the influence of n_1 and n_2 on the predictions of the MPLM). The predicted airflow pattern for the first case (Figure 4.40) is shown in Figure 4.42 and for the second (Figure 4.41) is shown in Figure 4.43. The recirculation in Figure 4.42 is confined mostly close to the inlet side, while the recirculation in Figure 4.43 covers the entire room. Comparison of the two airflow patterns with the CFD prediction (Figure 4.6) shows that the prediction of Figure 4.43 for $U_x = U_o$ in the specific zone is more acceptable than Figure 4.42. Therefore, in the following sections $U_x = U_o$ will be employed in Equation 4.8 for the verification of the MPLM predictions for isothermal and non-isothermal rooms.

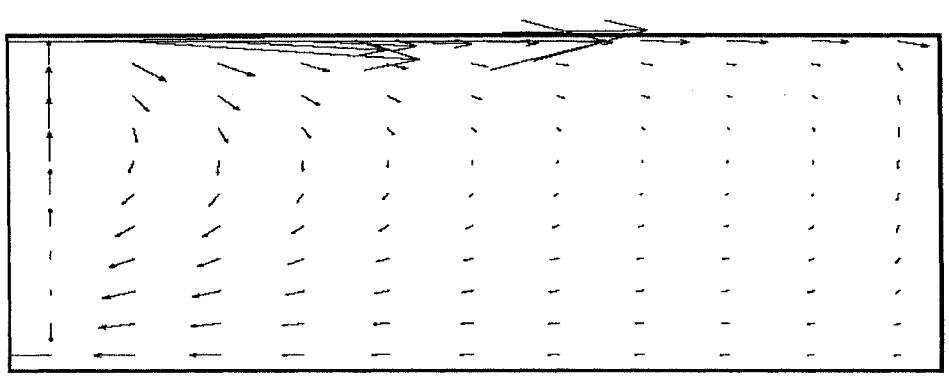

Figure 4.42 Airflow pattern predicted by MPLM using the profile in Figure 4.40, Case I.

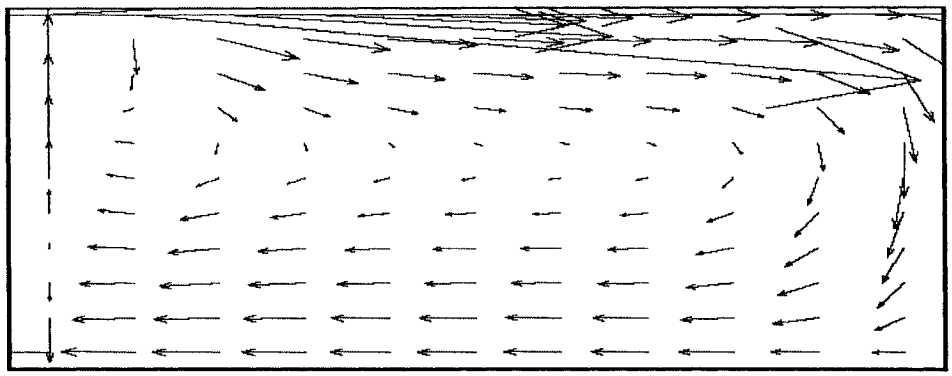

Figure 4.43 Airflow pattern predicted by MPLM using the profile in Figure 4.41, $n_1 = 0.5$ and $n_2 = 2$, Case I.

4.4 Verification of the MPLM prediction for an isothermal room

The predictions of the airflow distributions for the isothermal room were performed for wall and ceiling inlets.

4.4.1 Wall inlet

The same room with a slot inlet at $U_0 = 3.47$m/s, Case I (Nielsen, 1998) shown in Figure 4.1, was used for the simulation. The prediction of the MPLM was then compared with the PLMK and experimental data. The PLMK was chosen because of its better prediction of the airflow pattern compared to the other zonal models in Table 4.2. Furthermore, in order to examine the influence of n_1 and n_2, the simulations of the MPLM were conducted by varying first n_2 and then n_1.

4.4.1.1 Influence of the surface-drag exponent, n_2

Five values were chosen for n_2 (1/7, 0.5, 1, 1.5, 2). These values include the laminar (n_2 = 2) and turbulent (n_2 = 1/7) flow velocity profiles in a duct. $n_1 = 0.5$ was used for all of the

simulations. Since other values of K have no influence on the prediction, K =1.0 was used for all simulations of the MPLM.

Comparisons of the velocity profile predicted by the MPLM for the five n_2 values at two vertical positions are depicted in Figures 4.44 and 4.45. For all values of n_2, the prediction of the velocity profiles by the MPLM and that of the PLMK are similar to each other and to the measured profile at x = 1m. But the maximum predicted velocity close to the floor is lower at x = 3m for both the MPLM and the PLMK.

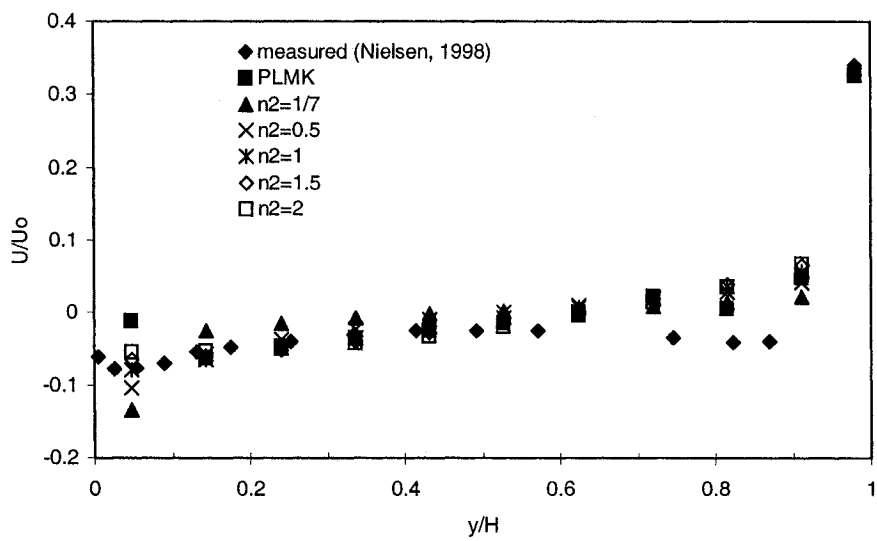

Figure 4.44 Comparison of the MPLM predictions for different values of n_2 with measured data and the PLMK at x = 1m.

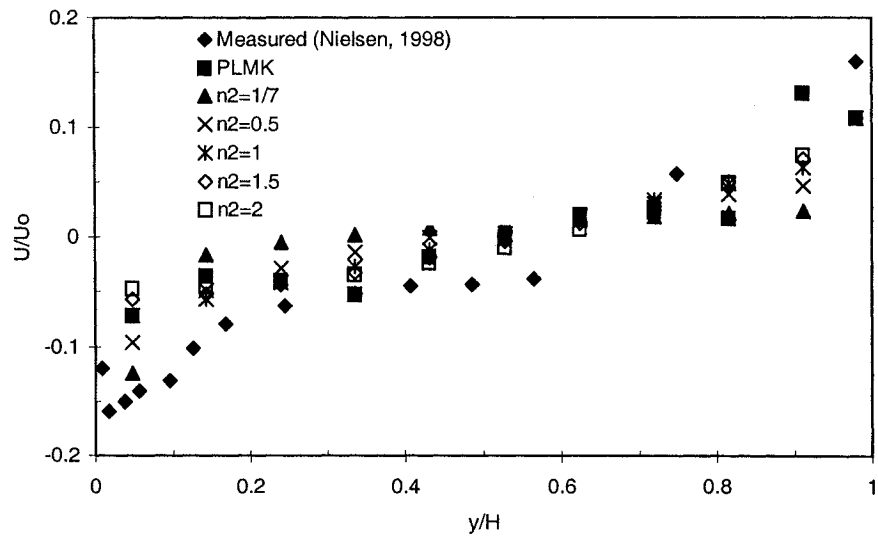

Figure 4.45 Comparison of the MPLM predictions for different values of n_2 with measured data and the PLMK at x = 3m.

Figures 4.44 and 4.45 also show that increasing n_2 decreases the magnitude of the velocity close to the floor. Furthermore, the predicted airflow patterns for the three values of n_2 (1/7, 0.5, 1.0) are shown in Figures 4.46 to 4.48. The predicted airflow pattern for n_2 = 2 is depicted in Figure 4.43. These figures show that increasing n_2 moves the center of the recirculation towards the ceiling. From Figures 4.43 and 4.48, it can also be discerned that n_2 = 1/7 is more accurate for cells close to the floor and n_2 = 2.0 is more acceptable for cells at the center and close to the jet zone. But Globally the airflow pattern predicted for n_2 = 2 is more acceptable since it captures the recirculation region better.

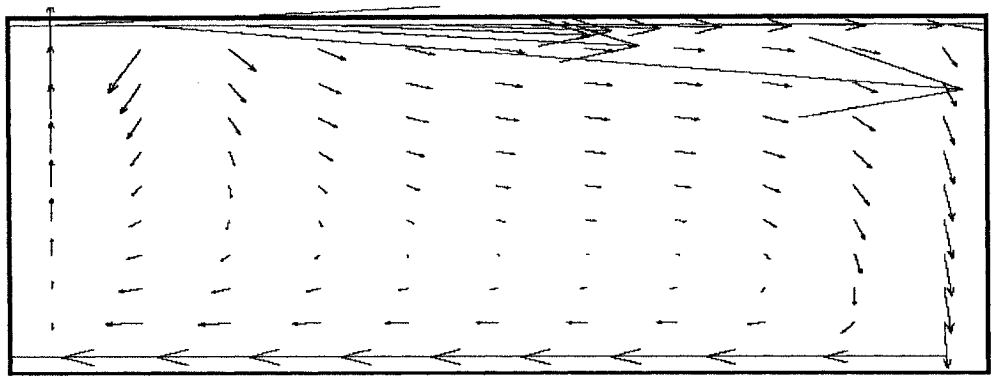

Figure 4.46 Airflow pattern predicted by MPLM for $n_1 = 0.5$ and $n_2 = 1/7$, Case I.

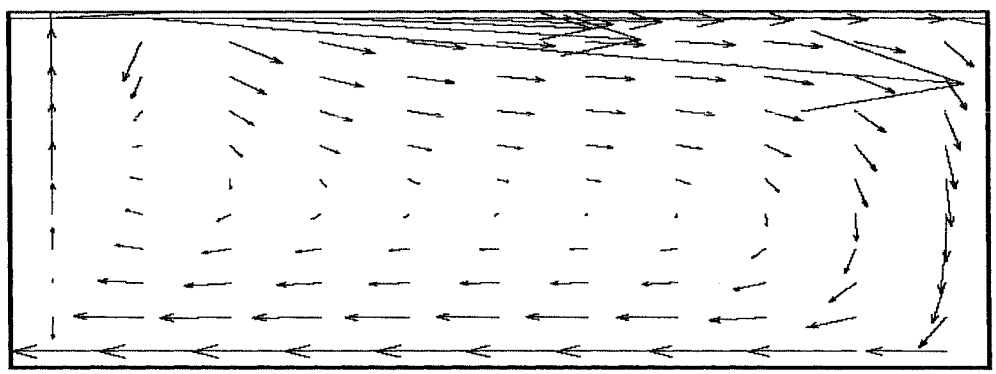

Figure 4.47 Airflow pattern predicted by MPLM for $n_1 = 0.5$ and $n_2 = 0.5$, Case I.

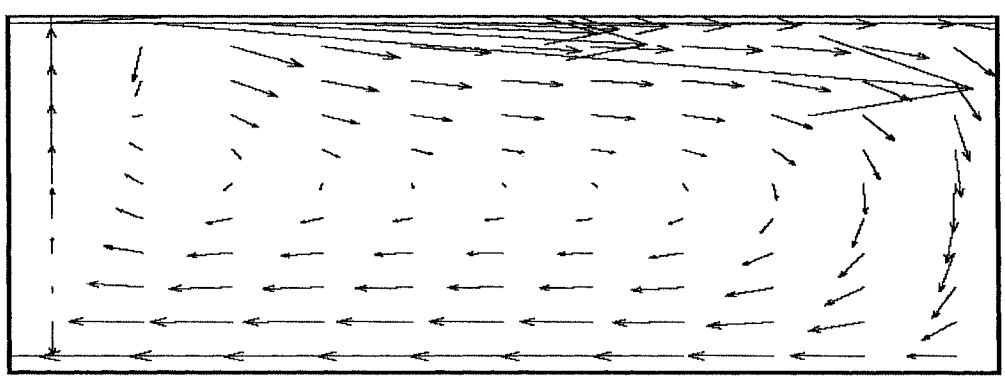

Figure 4.48 Airflow pattern predicted by MPLM for $n_1 = 0.5$ and $n_2 = 1$, Case I.

4.4.1.2 Influence of the power-law exponent, n_1

To investigate the effect of the power law exponent on the prediction of the MPLM, n_1 in Equation 4.8 was changed from 0.5 to 1.0. The values of $n_2 = 1$ and $n_2 = 2$ for $n_1 = 0.5$ from Figures 4.44 and 4.45 were also chosen. This gives four combinations of n_1 and n_2: ($n_1 = 0.5, n_2 = 1$); ($n_1 = 0.5, n_2 = 2$); ($n_1 = 1, n_2 = 1$); and ($n_1 = 1, n_2 = 2$). Figures 4.49 and 4.50 compare the air velocity profiles predicted by the four combinations of n_1 and n_2 at two vertical positions: x = 1m and x = 3m. The result show that for both vertical positions changing n_1 from 0.5 to 1.0 has no significant influence on the magnitude of the predicted air velocity.

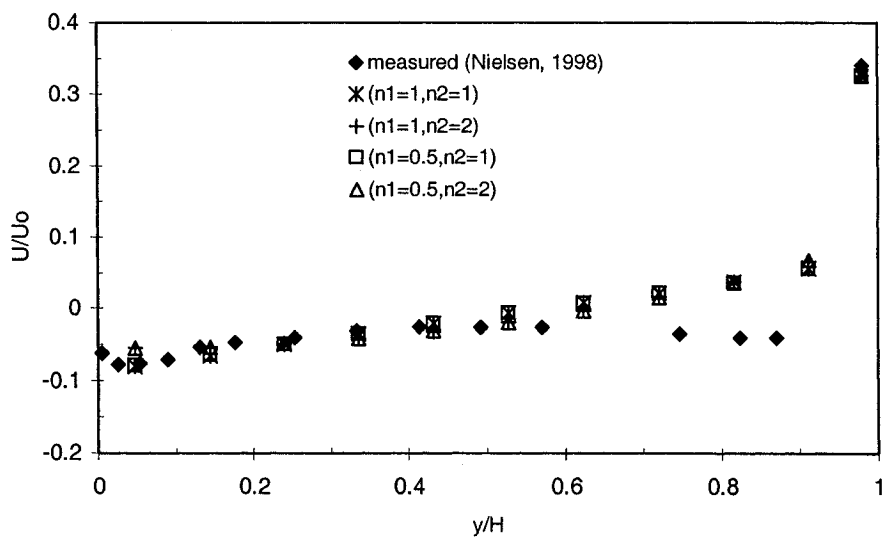

Figure 4.49 Comparison of the MPLM predictions for different values of n_1 and n_2 with measured data at x = 1m.

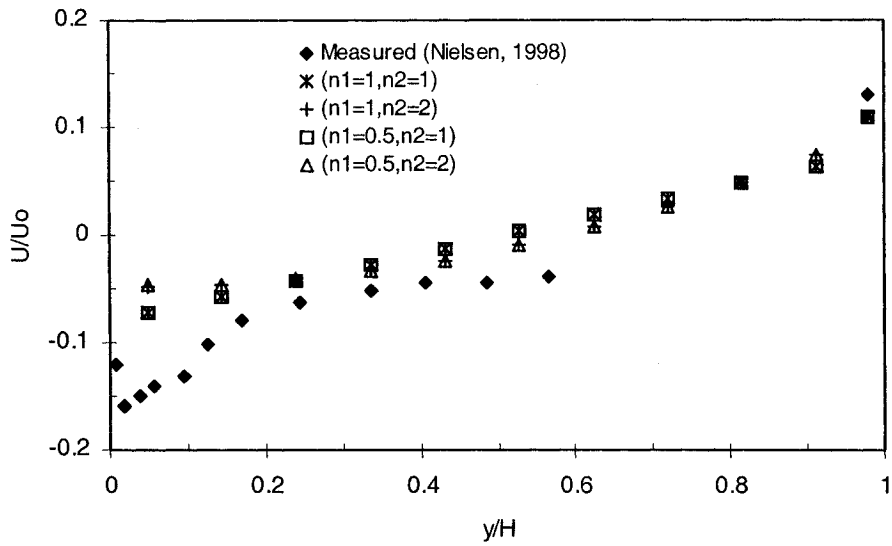

Figure 4.50 Comparison of the MPLM predictions for different values of n_1 and n_2 with measured data at x = 3m.

4.4.2 Ceiling inlet

For the ceiling inlet another room used for experimental and numerical study of room airflow by Nielsen (1998) was selected. Figure 4.51 shows the plan view of the room. The dimensions of the room were H = 2.8m, W = 4.0m, L = 6.0m, and h_0 = 0.02m. The slot inlet has three major parts, each of 1.2m long. The distance between two of the major parts was 0.13m and the distance from the sidewall to the inlet was 0.07m. Four exhausts with dimension of 1.2mx0.16m were positioned symmetrically on the ceiling. The air was discharged into the room in two opposite horizontal directions at an average velocity of 2.53m/s. In this case the velocity measurements in the room were also made with a low velocity flow analyzer type 54N50 from Dantec with accuracy of about 0.04m/s.

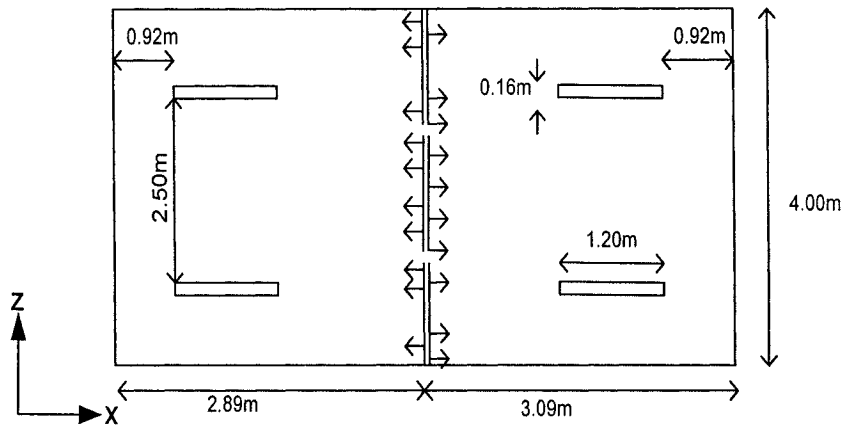

Figure 4.51 Plan view of the test room (Nielsen, 1998).

Simulations of the MPLM were done for 15x3x5 and 15x3x10 cells. Due to the aforementioned reasons, $n_2 = 2$, $n_1 = 1.0$, and $K = 1.0$ were used. Figures 4.52 and 4.53 illustrate the comparison of the predictions of the MPLM and measured values at two vertical positions (x = 1m and x = 2m) on the mid-plane of the room. The predicted air velocities follow the measured velocity profile for both 15x3x5 and 15x3x10 cells. Close to the floor, however, the measured velocities are higher. The discrepancies are more apparent at x = 1m than x = 2m from the left wall. But, the predicted velocities are within the range of accuracy of the measurement. Moreover, increasing the number of cells has increased the accuracy of the prediction below the center of recirculation. The flow fields predicted by the MPLM for the two cases are depicted in Figures 4.54 and 4.55. The recirculation region can be seen more clearly as the number of cells is increased.

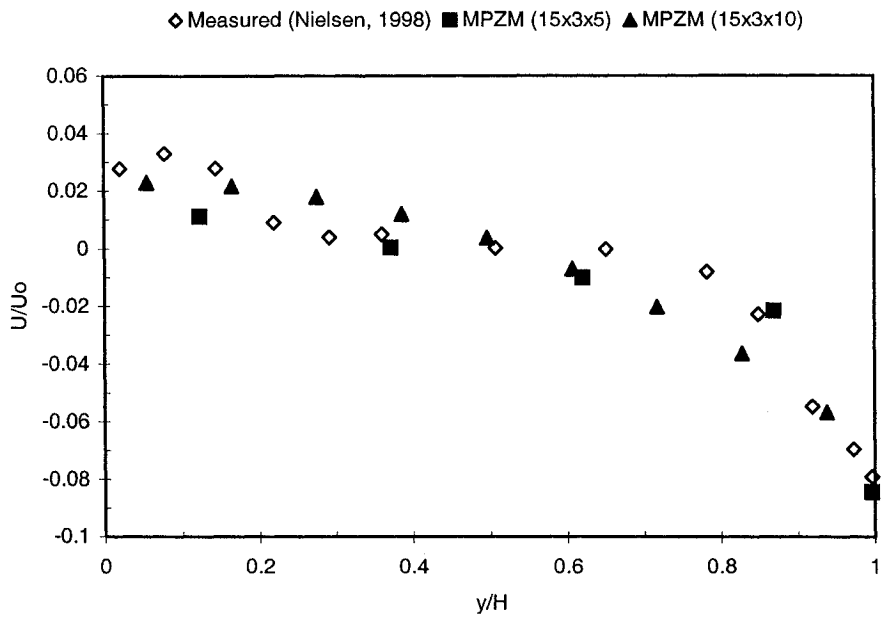

Figure 4.52 Comparison of the MPLM predictions with measure data at x = 1m.

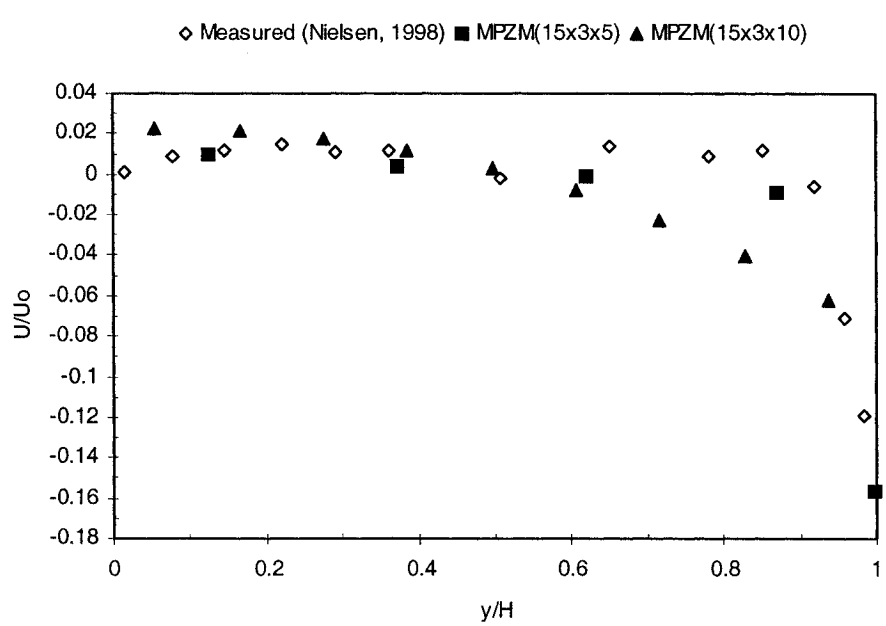

Figure 4.53 Comparison of the MPLM predictions with measured data at x = 3m.

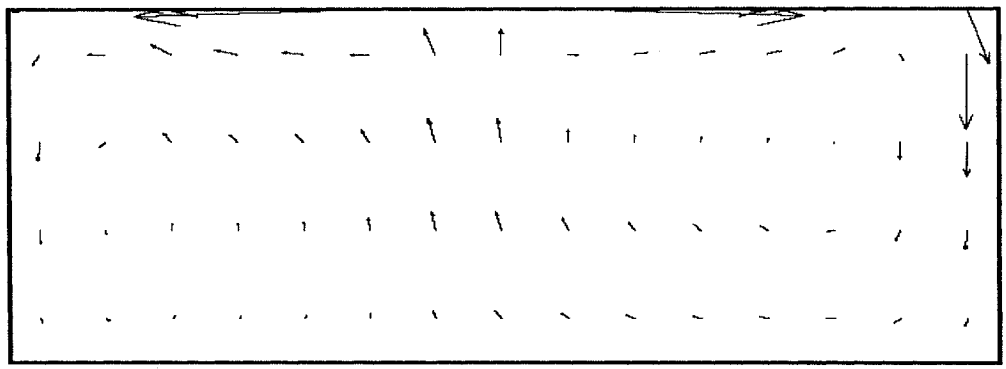

Figure 4.54 Airflow pattern predicted by the MPLM for 15x3x5 cells.

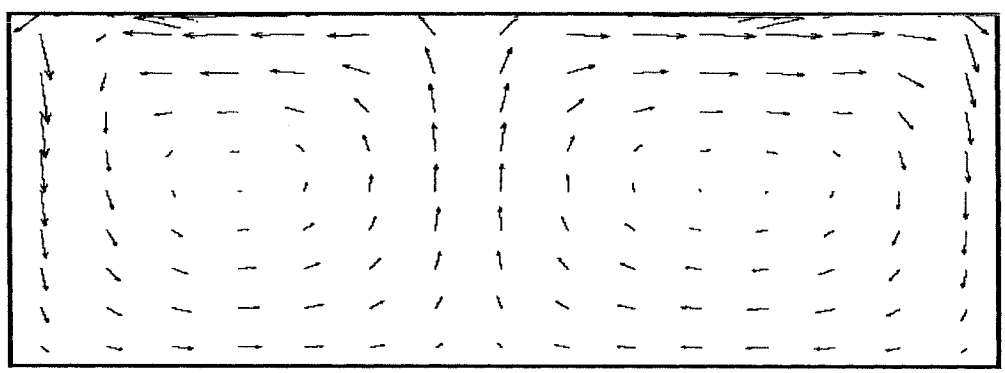

Figure 4.55 Airflow pattern predicted by the MPLM for 15x3x10 cells.

4.5 Verification of the MPLM prediction for a non-isothermal room

The isothermal condition is typically used for ventilation studies because of its simplicity in modeling and analysis. But good prediction of the airflow pattern and the magnitude of the air velocity in the non-isothermal condition are more meaningful and practical than isothermal condition.

It was stated that the PLM has been found to predict the airflow and the temperature distribution very well for natural convection since there is no influence from the inlet jet

(see Wurtz et al. 1999a; Haghighat et al. 200; Ren, 2002; Griffith and Chen, 2003; Gharbi et al. 2004). Consequently, the verification in this section concentrates on mixed convection in which both inertia and thermal buoyancy forces are important.

4.5.1 Case description

A non-isothermal room, shown in Figure 4.56, with L = 5.5m, W = 3.7m, and H = 2.4m, h_o = 0.05m, and outlet width = 0.2m (Zhang et al. 1992; Zhao, 2000) was selected. The average inlet air velocity (U_0) = 1.78 m/s. The heating capacity (178W/m^2) can raise the average room air temperature (T_{indoor}) to 32°C. The test room and the exhaust plenum chamber were well insulated so that the heat loss through the walls, ceiling, and floor can be neglected (Zhang et al., 1992). Zhang et al. (1992) and Zhao (2000) measured the air temperature and air velocity distribution in this room: Zhang et al. (1992) used the hot wire technique and Zhao (2000) used the PIV technique. The PIV technique, in addition to the magnitude of the air velocity, provides vector plot of the airflow pattern in the room.

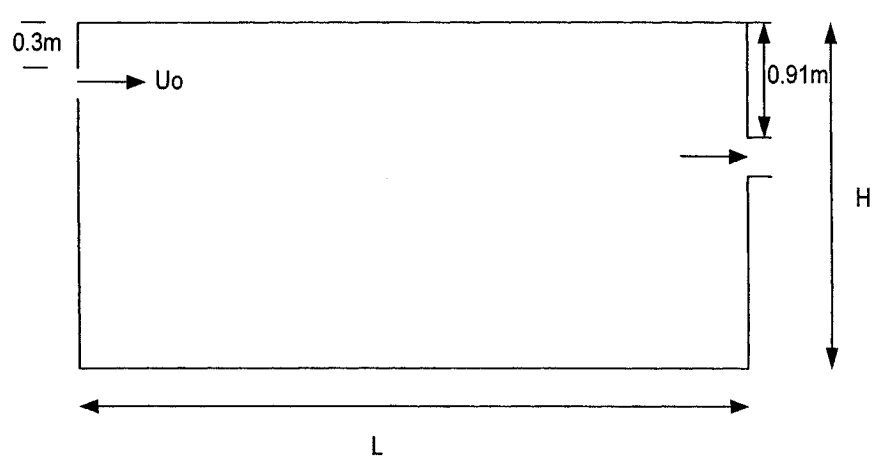

Figure 4.56 Geometry of test room (Zhang et al. 1992; Zhao, 2000).

4.5.2 Results and discussion

The major forces exerted on the air jet in the non-isothermal condition are inertia and thermal buoyancy. Therefore, for the non-isothermal condition, the Archemedes number (Ar_0), which is the ratio of thermal buoyancy force to inertia force (Equation 3.22) is an important parameter. It limits the penetration length (L_p) of the air jet. The critical Ar_0 is a limiting value above which the diffuser air jet drops immediately after entering the room. For T_0 = 24 °C, T_{indoor} = 32 °C, U_0 = 1.78 m/s and h_0 = 0.05m, Equation 3.22 gives Ar_0 = 0.004056. Since $Ar_0 < 0.023$, the air jet cannot drop immediately after entering the room and L_p is approximately equal to 3.3m (Figure 4.57). The MPLM was directly applied in the region $0 < x < L_p$. But the second term in Equation 4.8 was set to zero in the region $L_p < x < L$ due to the absence of the air jet in this region. Additionally, as per the description of the experimental set-up, all the surfaces except the floor are assumed adiabatic. The numerical solution technique outlined in Figure 3.5 was then employed to solve the system of mass and energy balance equations.

4.5.2.1 Air velocity distribution

Figures 4.58 and 4.59 depict the prediction of the airflow pattern in the non-isothermal room by the MPLM and the PLM, respectively. Comparing Figures 4.58 and 4.59 with the measure airflow pattern (Figure 4.57) shows that the MPLM prediction like PIV shows one recirculation zone formed within the range $0 < x < L_p$. The PIV also shows another smaller and weaker recirculation near the air outlet. The MPLM only shows the

tendency to form this weaker recirculation. Generally, the MPLM prediction of the airflow pattern is more acceptable than the PLM prediction.

Furthermore, Figure 4.60 shows the comparison of the air velocity predicted by the MPLM and the PLM with measured data at H = 1.7m from the floor. The comparison shows that the MPLM prediction is superior to that of the PLM. It predicts the air velocity very well. This shows that good prediction of the recirculation is important for the accuracy of air velocity distribution.

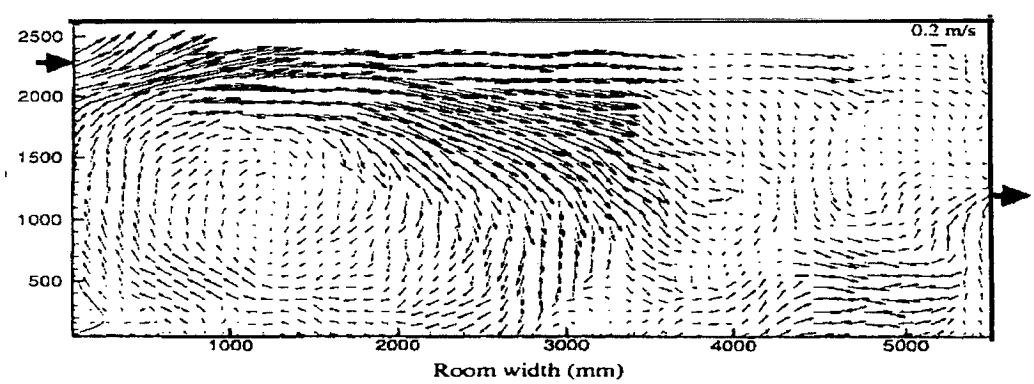

Figure 4.57 Airflow pattern measured using PIV technique (Zhao, 2000).

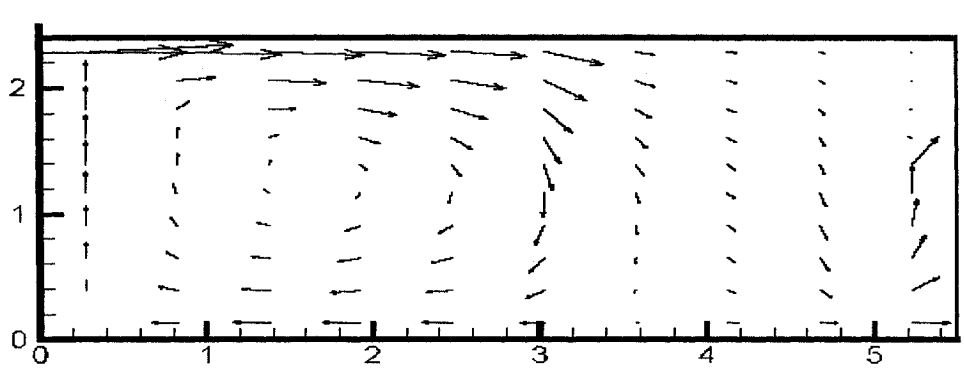

Figure 4.58 Airflow pattern predicted by the MPLM.

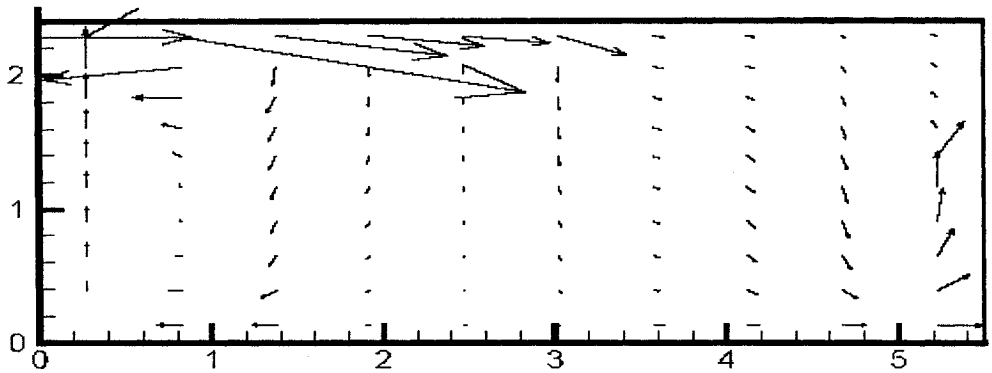

Figure 4.59 Airflow pattern predicted by the PLM.

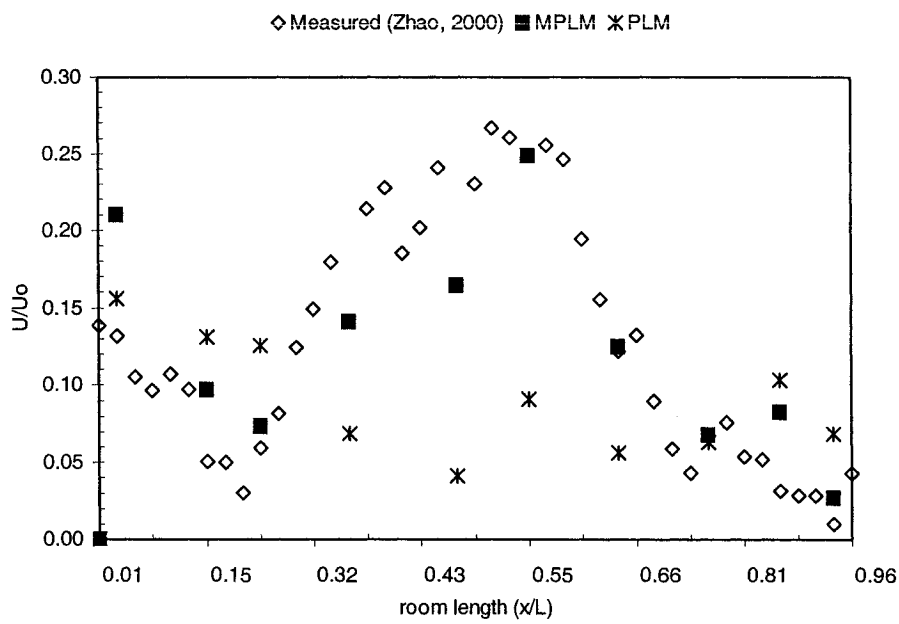

Figure 4.60 Comparison of measured and predicted air velocity at H=1.7m.

4.5.2.2 Air temperature distribution

The measured and predicted air temperature distributions in the room are depicted in Figures 4.61 to 4.63. As shown in Figures 4.57 and 4.58, the recirculation draws air from the outlet side to the inlet side. Since the floor further heats this warm air, the inlet side in

Figures 4.61 and 4.62 is always warmer than the outlet side. Comparing Figures 4.62 and 4.63 with Figure 4.61, it can be seen that both the MPLM and the PLM predict well the temperature close to the inlet and outlet sides. However, the temperature distribution around the occupied region is less than that of the MPLM prediction in Figure 4.62. This is because in the prediction of the PLM (Figure 4.61), the air jet falls rapidly after entering the room, which draws warm air to the inlet side, and the region outside the recirculation region moves the warm air to the outlet side. This leaves the occupied region at a lower temperature than either side of the room. This further shows the importance of predicting the recirculation region in the standard zone.

In conclusion, the approaches pursued in this chapter show the difficulty of obtaining an improved zonal model, which is applicable for many cases with little or no adjustment. The significance of using the same value of K for all cells and the estimation of K value using CFD, which culminated into the development of the PLMK and the $PLMK_{func}$ clearly underlined the challenges of improving the PLM by tuning of the parameter K. The MPLM was found to be more versatile than the other versions of the PLM and has significantly improved the prediction capability of the existing zonal models without increasing the computation time (in all cases convergence within ten seconds using a Pentium based 1.7GHz and 256MB PC). It is applicable for inlet configurations, which discharge air either horizontally or vertically. That is the inlet velocity has to be predominant in one coordinate direction. Thus, the MPLM may need more improvements to make it applicable when the diffuser discharges in all directions.

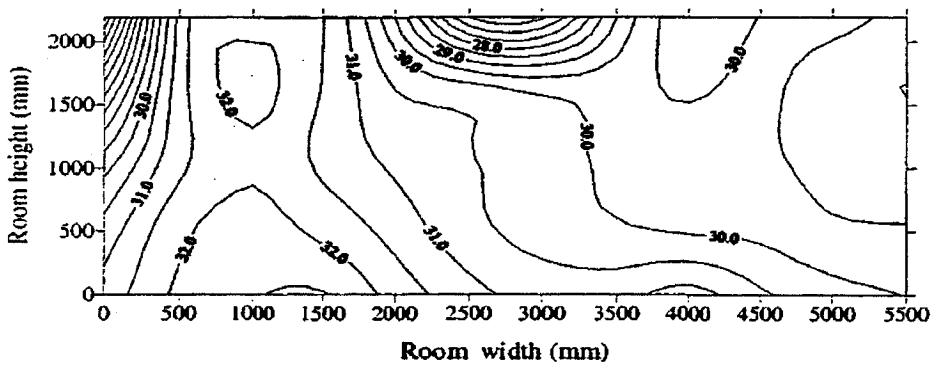

Figure 4.61 Measured temperature distribution (Zhao, 2000)

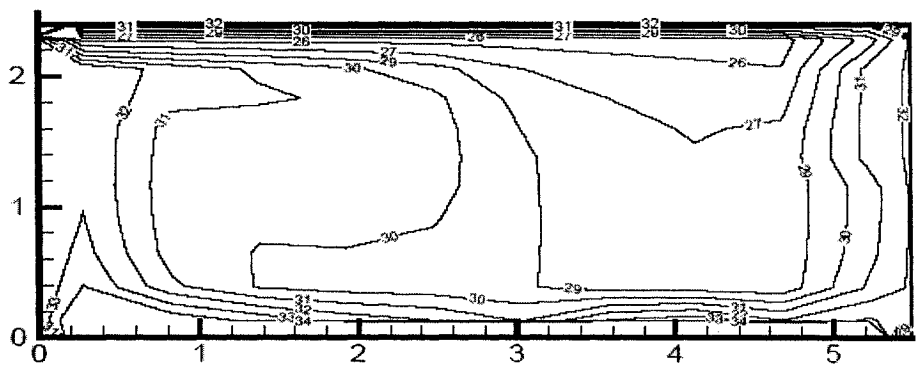

Figure 4.62 Temperature distribution predicted by the MPLM.

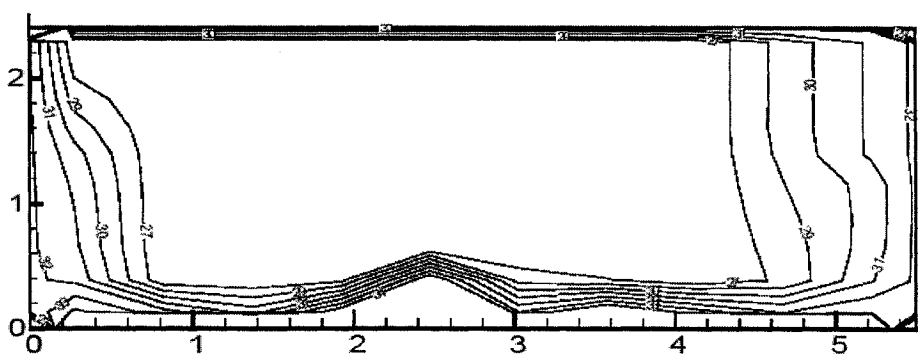

Figure 4.63 Temperature distribution predicted by the PLM.

4.6 Summary

In this chapter attempts were made to reduce the discrepancies of the zonal approach in the standard zone through a number of approaches. The significance of using the same value of flow coefficient, K, for all cells was first discussed. The result revealed the ineffectiveness of using one optimal K value for all cells in the standard zone to improve the prediction capability of the PLM.

The next attempt made to improve the PLM prediction was the use of a variable K for the case of forced convection. The estimation has shown that K_x and K_y vary differently and can be affected by variability of the airflow pattern, which can change significantly and depends on the choice of inlet device and its relative location. The PLMK has improved the prediction of the airflow pattern and its magnitude in the standard zone compared to the PLM.

The other improvement methodology pursued was the combination of the PLM and the SDM using the direct and the indirect approaches. The direct combination could not enhance the prediction capability of zonal models. The indirect approach has gave the MPLM. The introduction of the air jet contribution for the cells in the standard zone has made the air velocity prediction of the MPLM to be superior to all the other zonal models. The influence of the jet is only included in the dominant airflow direction, which is horizontal for horizontal inlet velocity and vertical for vertical inlet velocity.

The MPLM was also applied for a non-isothermal room. In this case the behavior of the air jet is affected by thermal buoyancy as well as inertia. The MPLM was directly applied in the region included in the jet penetration length and the contribution of the jet in the region outside of the jet penetration was neglected. Good agreement was obtained between measured and predicted air velocity and air temperature.

5 APPLICATION OF THE ZONAL MODELS FOR DOUBLE-SKIN FAÇADES

It was highlighted in the literature review that the zonal approach has been applied for isothermal and non-isothermal conditions (see Table 2.1). The verifications of the MPLM in Chapter 4 further showed that how the predictions of the zonal approach could be improved for isothermal and non-isothermal conditions. Nevertheless, the zonal approach has not been applied to predict the performance of double-skin façades (DSF).

DSF are building envelopes, which are composed of two glasses, a ventilated air cavity in between and solar control devices placed within the cavity. The ventilated cavity functions as a thermal buffer by reducing problems such as undesired heat gain during the cooling season, heat loss during the heating season and thermal discomfort due to asymmetric thermal radiation. DSF can be classified according to ventilation and construction type (see Appendix A.1).

Experimental and numerical models have been used for studying the performance and optimization of DSF. Models that have been used for the prediction and analysis of the performance of DSF include CFD, analytical and lumped models, dimensional analysis, network models and control-volume models. A review of experimental and numerical studies on DSF is presented in Appendix A.2.

The DSF considered for this study (see Section 5.1) is mechanically ventilated since the fan installed at the exit provides suction - there is no air jet at the inlet of the DSF and all the cells in the air cavity are in the standard zone. Consequently, the second term in Equation 4.8 is zero and the PLM can be used to evaluate the airflow rate in the DSF cavity. The development and solution technique of the zonal air and thermal flow models for DSF are compiled in Appendix A.3 to A.6.

In this Chapter, the application of the zonal models for the prediction of the temperature stratification in a mechanically ventilated DSF system is presented. Section 5.1 provides the case used for the development and validation of the thermal and airflow models. Section 5.2 discusses the verification of the zonal models' predictions. A parametric study is presented in Section 5.3. Finally, the findings of this chapter are summarized in Section 5.4.

5.1 Case description

The case used for the development and verification of the DSF models is an experimental test cell at the Department of Energy Studies, Politicnico di Torino, Italty. The test cell was 2.5m high, 1.6m wide and, 3.6m long. The south facing side of the cell, which was 1.6m wide and 2.5m high, has a DSF with an outer double-pane façade, and an inner façade as shown in Figure 5.1. The outer double-pane façade, L1 and L2, was divided into three parts: upper, middle and lower. L1 and L2 were 8mm and 6mm thick clear glasses. The air cavity between L1 and L2 was 15mm wide. The internal pane, L4, was

6mm thick clear glass, which could be opened in order to make the gap accessible. The air cavity between L2 and L4 is 14.8cm wide and can be enlarged up to 30cm.

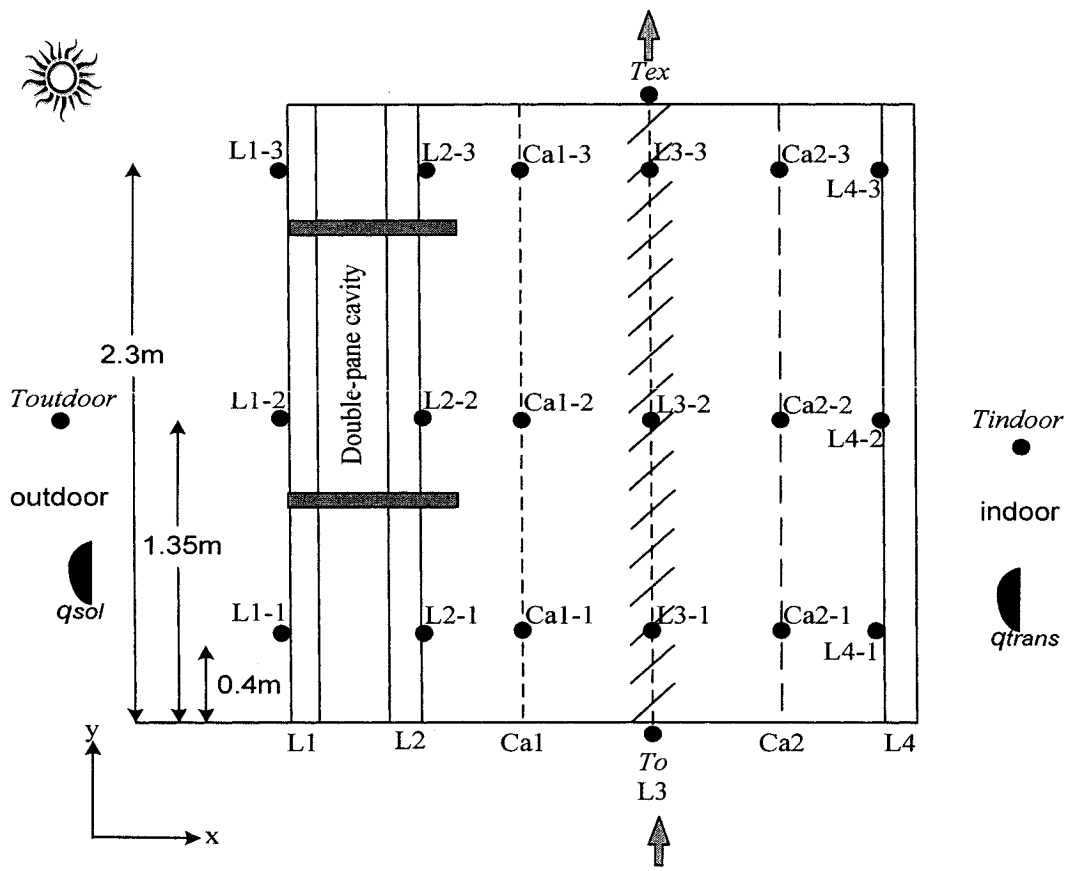

Figure 5.1 Mechanically ventilated DSF. L1 is the exterior glass of the double pane; L2 is the interior glass of the double-pane; L3 is the venetian blinds; L4 is the interior glass of the ventilated DSF; Ca1 is the outer cavity; and Ca2 is the inner cavity, T_o is the air temperature at the inlet, T_{ex} is the air temperature at the exit, T_{indoor} is the room air temperature, $T_{outdoor}$ the outside air temperature, q_{sol} is the total solar radiation, q_{trans} is the transmitted solar radiation, ● is thermocouple and ◖ is pyranometer.

A venetian blind, L3, was installed in the air cavity between L2 and L4. The slats have small pores and were inclined at 45° from the horizontal. The air from the test cells enters into the DSF cavities through an opening located at the bottom of the DSF, which is then extracted at the top of the DSF by a fan.

The test cell was equipped with a continuous monitoring system to measure energy consumption, indoor air temperatures, heat fluxes through the façade, temperature distributions in the air gap and on the façade surfaces, and airflow rate. The sensors in the DSF system were positioned at 0.4cm, 1.35m, and 2.3m from the floor as shown in Figure 5.1. The average volumetric flow rate at inlet is 54.2 m^3/h. The measured outdoor and indoor boundary conditions (on April 23, 2005) are shown in Figure 5.2. These data will be used in section 5.2 as input to the zonal models.

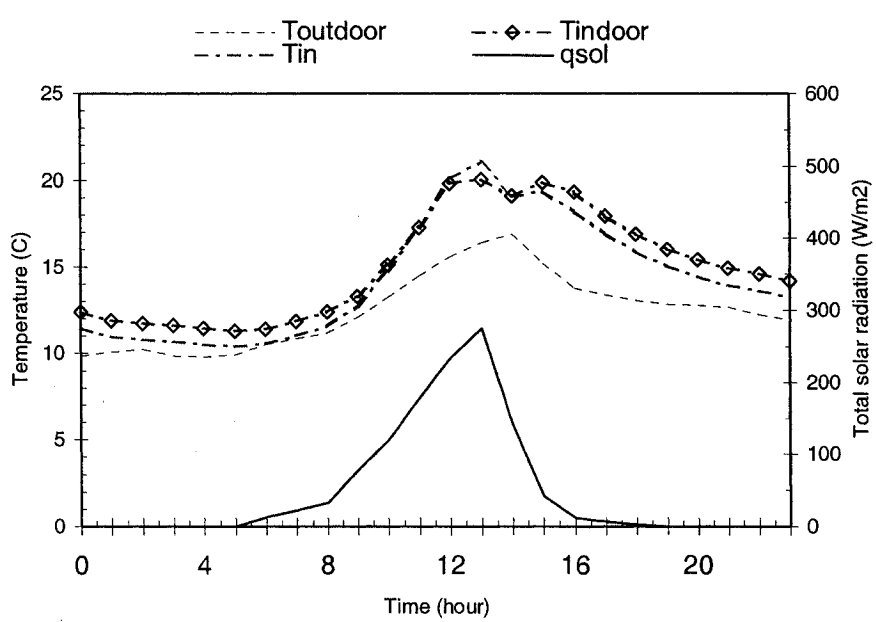

Figure 5.2 Measured inlet and boundary conditions.

5.2 Model verification

In order to avoid overheating of the DSF cavity and the venetian blinds, and to monitor the energy exchanged as the ventilating air flows through the cavity, temperature distributions in the outer cavity (Ca1), inner cavity (Ca2), venetian blinds (L3), and the exhaust temperature should be predicted. Moreover, the temperature distribution in the inner glass (L4) should be known in order to evaluate the thermal comfort in the room. Thus the comparisons of the measured and predicted temperature distributions were done for the air in the outer cavity, the venetian blinds, the air in the inner cavity, and the inner pane at the positions (1) 40cm, (2) 135cm and (3) 230cm (Figure 5.1). The comparison of the temperature of exhaust air with experimental data was also done. Figures 5.3 to 5.6 depict the temporal and spatial variation for Ca1, Ca2, L3 and L4. The temporal variation of the exhaust temperature is shown in Figure 5.7.

In all of the figures the predicted temperature follows the experimental data and the prediction error increases during higher solar radiation, and attains a maximum value around 13:00 hour. The prediction error for the outer cavity, the inner cavity, the venetian blinds and the inner glass, shown in Figures 5.3 to 5.6, is mostly at the top position than at the middle and bottom. The errors could be due to

- the complicated long wave exchange with the venetian blinds and the other surfaces;
- the lumping of the diffused and reflected solar radiation into the total radiation instead of treating them separately due to shortage of measured data;

- three-dimensional effects such as reverse flow and local short circuit caused by the outer façade frames (used to partition the outer pane into three parts);
- the complicated airflow through the venetian blinds;
- the heat transfer through the frames;
- air leakage;
- experimental errors; and
- the uncertainty of surface heat transfer coefficients.

A more detailed model such as CFD could be used to reduce the errors. But the occurrence of errors of these magnitudes could be difficult to avoid even if CFD was employed (see Manz, 2004; Manz et al. 2004). Therefore, from the perspective of the simplified approach pursued for thermal and airflow modeling of the DSF, the results obtained in this study show that the zonal model can be used to assess the performance of the DSF system with venetian blind by providing information which is not possible for the lumped and the control-volume models. The lumped model only uses a single node for each part of the DSF system, whereas the control-volume approach is good for estimating the vertical stratification of temperature when the shading device is a roller screen.

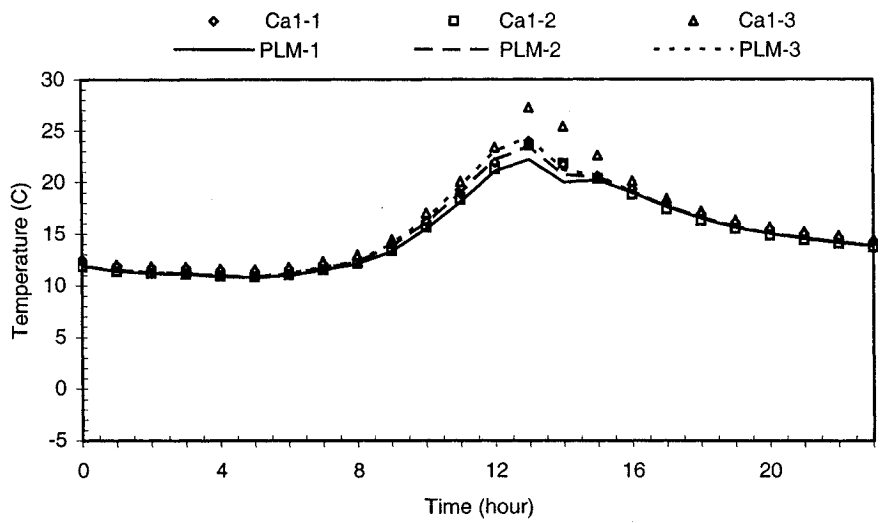

Figure 5.3 Comparison of predicted and measured temperature of the air in Ca1 at positions 1, 2, and 3.

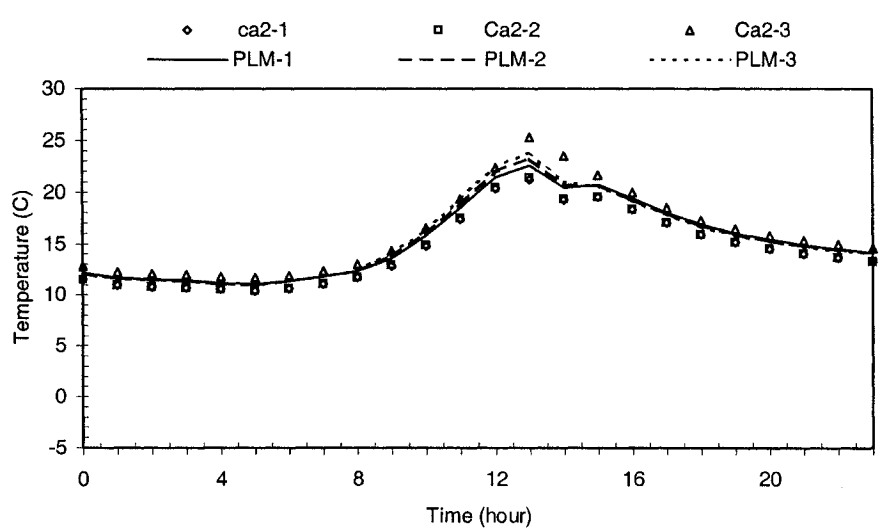

Figure 5.4 Comparison of predicted and measured temperature of the air in Ca2 at positions 1, 2, and 3.

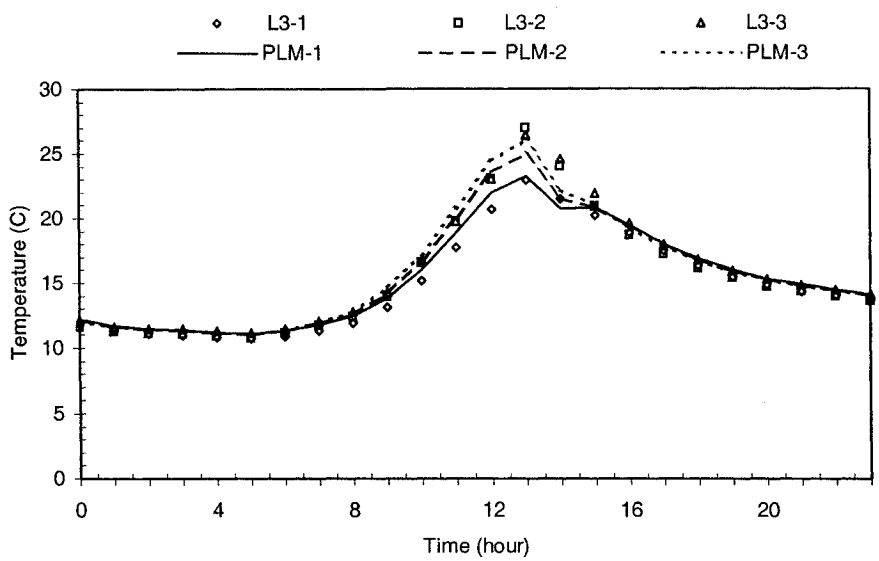

Figure 5.5 Comparison of predicted and measured temperature of the venetian blind at positions 1, 2, and 3.

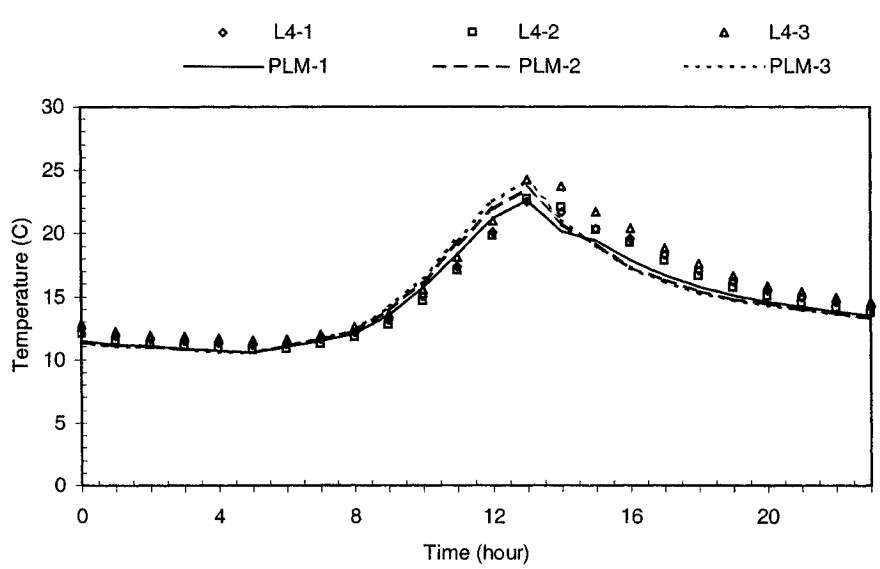

Figure 5.6 Comparison of predicted and measured temperature of inner glass at positions 1, 2, and 3.

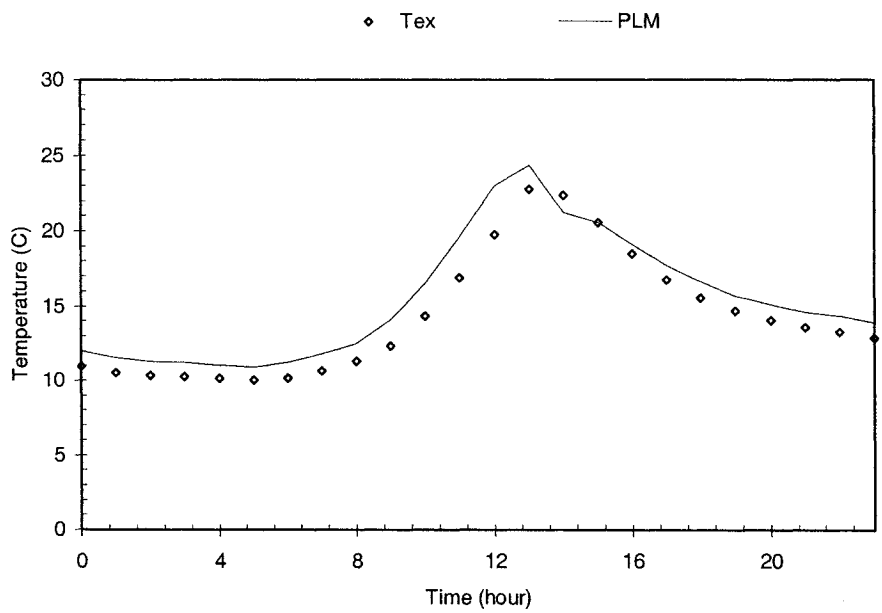

Figure 5.7 Comparison of predicted and measured temperature of exhaust air.

5.3 Parametric study

The zonal models were then used to evaluate the influence of some of the parameters of the DSF on the temperature change of the cavity air from inlet to outlet $(T_{ex}-T_{in})$. The inlet flow rate (M_0), the height of the DSF (H), the presence and absence of venetian blinds were chosen. The study used three values for the airflow rate ($0.5M_0$, M_0 and $2M_0$); three values for the height ($0.5H$, H and $2H$); and two possibilities for the venetian blinds (with blinds and without blinds). When the value of one parameter was changed, the values of the other parameters were kept constant, and in all cases the inlet and boundary conditions in Figure 5.2 were used.

The influences of M_o, H and venetian blinds on the inlet-outlet temperature difference (T_{ex}–T_{in}) are shown in Figures 5.8 to 5.10. For all values of the three parameters, T_{ex}–T_{in} increases with increase in solar radiation. The impact of changing the values of each parameter is more apparent during the day than during the night. The results of the parameter study are summarized in the following subsections.

5.3.1 Inlet airflow rate

As depicted in Figure 5.8, T_{ex}–T_{in} is lower as the inlet flow rate M_0 increases. This indicates that increasing the inlet airflow rate makes the air flowing in the cavity cooler and decreases the indirect heat gain to the room.

5.3.2 Height

The influence of the height of the DSF (H) on T_{ex}–T_{in} is depicted in Figure 5.9. T_{ex} –T_{in} increases as H increases. Thus, increasing H is not good strategy to control the indirect heat gain to the room. This is a practical problem for DSF used for multistory buildings.

5.3.3 Shading device

The effect of the presence and absence of venetian blinds on T_{ex}–T_{in} is shown in Figure 5.10. The T_{ex}–T_{in} is higher with blinds than without blinds. The indirect heat gained by the blinds heats the cavity air. This shows that although venetian blinds reduce the direct solar gain, they can increase the indirect gain if the DSF cavity is not properly ventilated.

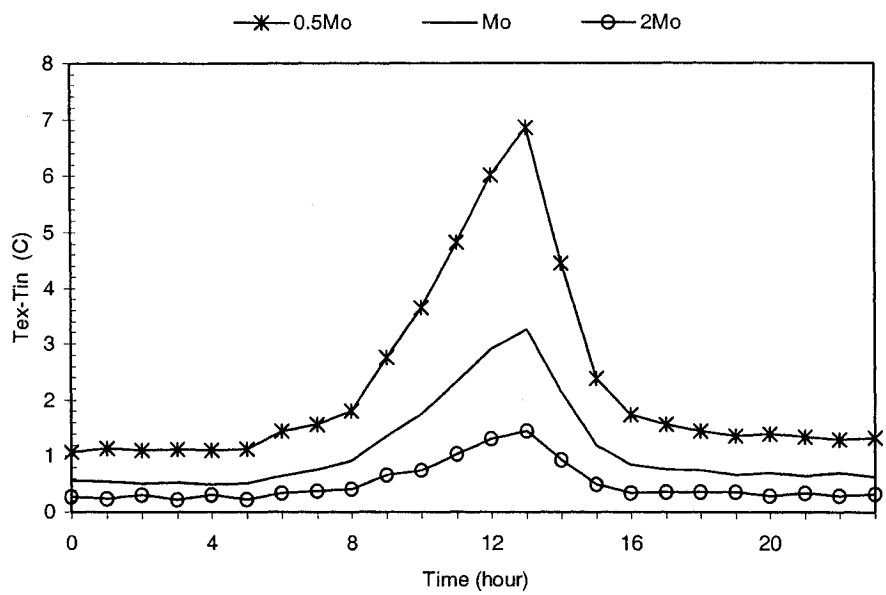

Figure 5.8 Sensitivity of T_{ex}–T_{in} to M_0.

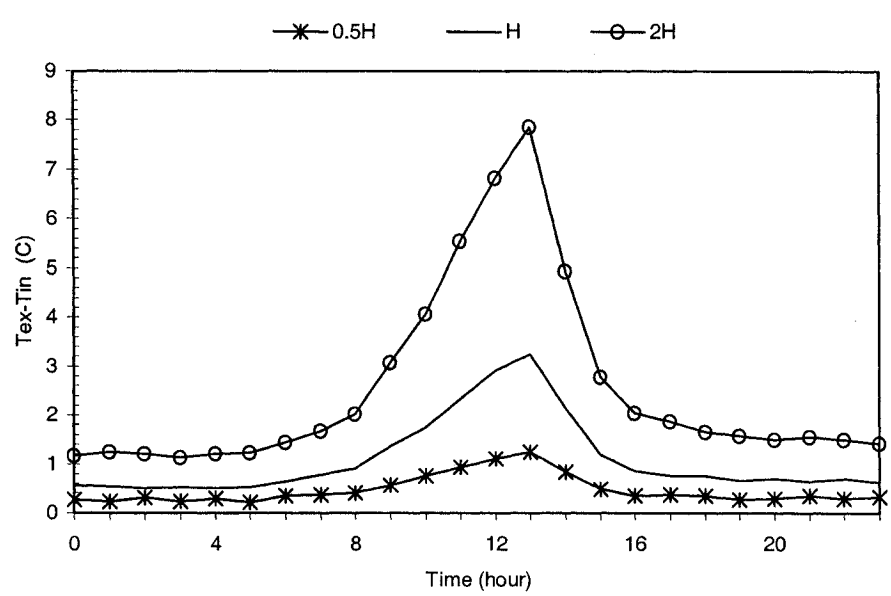

Figure 5.9 Sensitivity of T_{ex}–T_{in} to H.

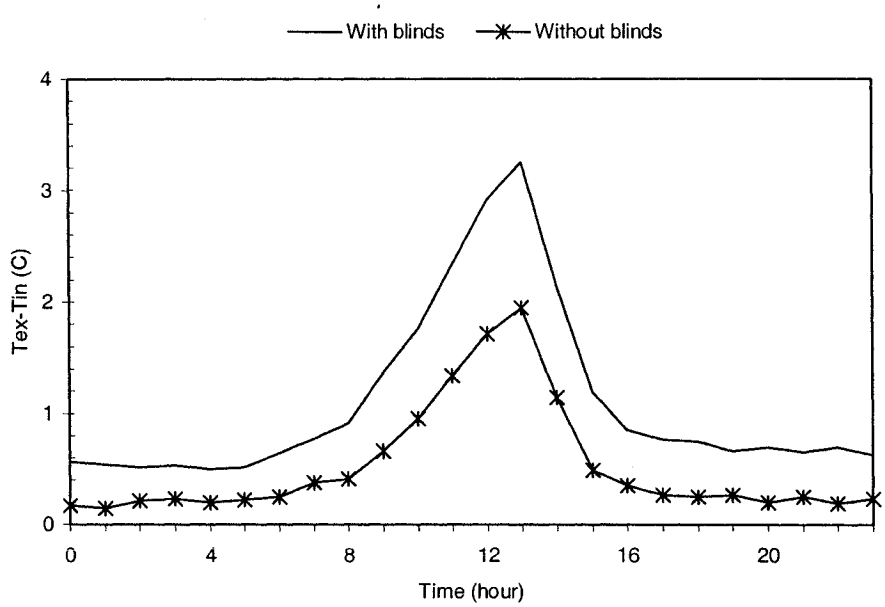

Figure 5.10 Sensitivity of T_{ex} –T_{in} to venetian blinds.

5.4 Summary

In this chapter zonal modeling of DSF with venetian blinds was discussed. The predicted temperature follows the experimental data and the prediction error increases with higher solar radiation. However, as far as the simplified approach pursued for thermal and airflow modeling of the DSF is concerned, the results show that the zonal model can be used to assess the performance of the DSF system with venetian blinds.

The zonal model was also used to assess the influence of parameters such as H, M_0, and the presence of venetian blinds on the outlet-inlet temperature difference, T_{ex}–T_{in}. The result shows that the influence of changing the values of each parameter is more apparent

during the day than during the night. Increasing H and the presence of venetian blinds increases T_{ex}–T_{in}, while increasing M_0 decreases T_{ex}–T_{in}.

6 CONCLUSIONS AND RECOMMENDATIONS

In the zonal approach a room is divided into specific and standard flow zones. The specific flow zones include jets, plumes, and boundary layer zones. The standard flow zone is the region outside the specific zones, which includes the occupied region. The airflow models used in specific flow zone and standard flow zone are referred to as non-pressure models and power-law model (PLM), respectively.

The PLM has shown pronounced discrepancies in predicting the recirculation and the magnitude of the air velocities in the standard zone for the case of forced convection. Previous attempts such as the use of values of K other than 0.83 for all cells in the standard zone, and the surface-drag flow model (SDM) were unable to reduce the discrepancy. Moreover, intermediate models (such as the zonal models) that can provide global information faster than CFD and more accurately than simpler models (such as the lumped and the control-volume) have not been applied for double-skin facades (DSF).

In the following sections, the concluding remarks are summarized and the recommendations for future work are addressed.

6.1 Concluding remarks

1. One K value for all cell

- This approach shows that for forced convection, as long as the same value of K is used for all cells, it is impossible to improve the prediction capability of PLM in the standard zone.

2. Estimation of K value for each cell

- For isothermal condition, the error in using the commonly used constant value of K = 0.83 increases away from the mid-height for the horizontal flow and decreases for the vertical flow.
- For isothermal forced convection, the variation of average K_x and K_y as a function of the dimensionless height (y/H) depends on the type and location of the diffuser.
- The two models developed using this approach are the PLM with variable K (PLMK), and the PLM with variable K where K is a function of y/H ($PLMK_{func}$). The former directly uses the distribution of the K_x and K_y for each cell while in the latter the variation of K_x and K_y as a function of y/H is obtained using the average values of K_x and K_y for all cells at the same height, y/H.
- The PLMK gives better predictions than the PLM and $PLMK_{func}$. But it is difficult to generalize: in order to estimate appropriate value for K_x and K_y, one needs to run a new CFD simulation for the particular case, which is an undesired complication. Moreover, although the PLMK prediction of the airflow pattern was better, improvement was needed to predict a more accurate airflow pattern (recirculation) in the standard zone.

3. Combining the PLM and the SDM

- Two approaches were employed for combining the PLM and the SDM: direct and indirect.
- For the direct approach, the pressure difference $\Delta P_{i,j}$ and the mass flow rate $m_{i,j}$ in the SDM and the PLM were added to get the total pressure drop and mass flow rate between two cells.
- For the indirect approach, analogy of flow between parallel plates was used to modify and combine the SDM with the PLM. This modification means inclusion of the influence of the inlet air jet on the standard zone in the PLM, which gives the modified power-law model (MPLM).
- The models obtained using the direct approach: SDM1, SDM2, SD-PLM1, SD-PLM2, and SD-PLM3 were found to be unable to predict recirculation in the standard zone compared to the PLMK and experimental data.
- In the MPLM, air jet model was also used in the specifice zone. The influence of the jet was only included in the dominant jet flow direction, which is horizontal for horizontal inlet velocity and vertical for vertical inlet velocity.
- The MPLM was found to predict the flow field reasonably well in the standard zone compared to the other zonal models such as the PLMK for an isothermal room and PLM for a non-isothermal room.
- Varying the power-law exponent of the MPLM (n_l) has been found to have no significant influence on the prediction of the MPLM. However, varying the

surface-drag exponent (n_2) of the MPLM was found to affect both the location of the center of the recirculation and the magnitude of the velocities.

- Application of the MPLM for non-isothermal room shows the importance of accurate prediction of the recirculation in the standard zone since it significantly affects the distribution of the air velocity and temperature in the occupied region.

4. Application of the zonal models for DSF

- The predicted temperature follows the experimental data and the prediction error increases with higher solar radiation.
- The results show that the zonal model can be used to assess the performance of the DSF system with venetian blind by providing information which is not possible for the lumped and the control-volume models.
- The result of the parametric study shows that the influence of changing the values of the parameters M_0, H, and the presence and absence of venetian blinds are more apparent during the day than during the night. Increasing H and the presence of venetian blinds increases outlet-inlet temperature difference, $T_{ex} - T_{in}$, while increasing M_0 decreases $T_{ex} - T_{in}$.

6.2 Recommendations for future works

This study has introduced new methodologies for improving the prediction capability of the PLM. A new generation of zonal models were developed using these methodologies. The models were applied for predicting the airflow and temperature distribution in a

room and in a mechanically ventilated DSF with venetian blinds. In order to enhance these contributions, the recommendations for future work could include:

- Improving the MPLM further so as to accommodate the different inlet configurations encountered in a room.
- Integrating the MPLM and its improved versions in the COwZ program to enhance the prediction capability of the latter. This will broaden the potential applications of the zonal approach, which includes the provision of faster prediction of contaminant dispersion and temperature distribution in a building and the surroundings for protecting building occupants from fire accidents, chemical/biological attacks by terrorists and from natural occurring diseases such as SARS and avian flu, and to explore the influence of urban heat island on heating and cooling load of a building.
- Integrating the DSF model into Building Simulation tool that includes the HVAC plant, which could allow evaluation of the use of control mechanisms in the DSF and their influence on the energy consumption of the HVAC system.

APPENDIX A: DOUBLE-SKIN FAÇADES

A.1 Classification

Double-skin façades (DSF) can be classified based on the type of ventilation and construction. The ventilation of the DSF cavity can be either natural or mechanical. The driving force for natural ventilation is either thermal buoyancy or wind pressure. The airflow is therefore not easy to control nor is it continuous since it depends on the weather condition. Naturally ventilated façade, depicted in Figure A.1b, can be applied as a supply window for natural ventilation of room (when the window on the internal façade is open) or as an insulation envelope for a conditioned room (when the window on the inner façade is closed), which increases the thermal resistance. Mechanically ventilated façade, shown in Figure A.1a, is usually part of the Heating Ventilation and Air Conditioning (HVAC) system of the building (Figure A.1a). The type of opening on the inner façade can be like a window for naturally ventilated façade or simply a slot for a mechanically ventilated façade.

Naturally ventilated DSF can be subdivided based on the way the façade is constructed (Oesterle, 2001): box windows, shaft-box windows, corridor façades, and multi-story or continuous façades. Box windows are the oldest form of DSF. The cavity between the two facades is divided horizontally a room-by-room basis. Vertically, the divisions occur either between stories or between individual window elements. They are discontinuous

which helps to avoid the transmission of sound and contaminants. Shaft-box façades are a special form of box window construction consisting of a system of box windows with continuous vertical shafts that extend a number of stories to create a stack effect. In the case of corridor façades, the intermediate space between the two skins is closed at the level of each floor. For multistory (continuous or buffer) façades, the intermediate space between the inner and outer layers is adjoined vertically and horizontally by a number of rooms. In the extreme case, the space may extend around the entire building without any intermediate divisions.

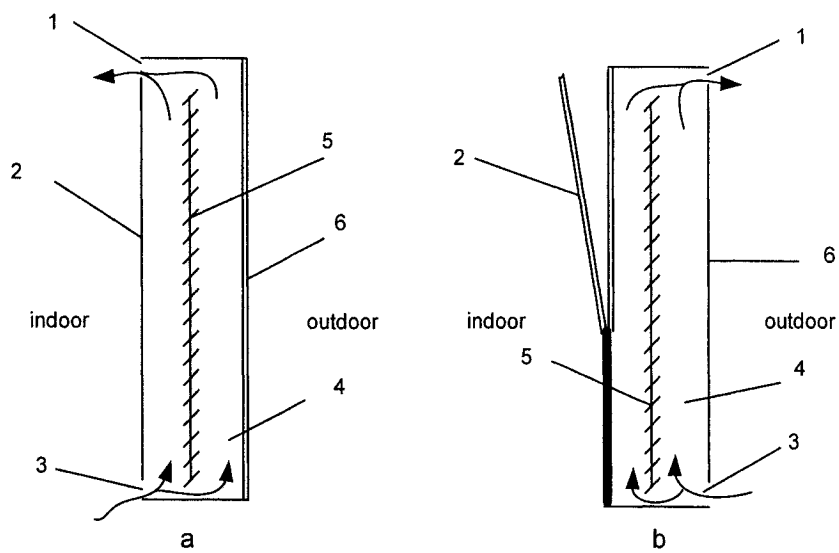

Figure A.1 Components of ventilated double-glass façade (a) mechanical ventilation (b) natural ventilation. (1) air outlet, (2) interior pane, (3) air inlet (4) air cavity, (5) shading device and (6) outer pane.

A.2 A review of experimental and numerical studies on DSF

CFD and other simple models such as analytical and lumped models, dimensional analysis, network models and control-volume models have been used for the prediction and analysis of the performance of DSF.

The lumped approach represents each façade and cavity by a single temperature. Haddad and Elmahdy (1998); Park et al. (2004a); Park et al. (2004b); Von Grabe (2002); and Balocco (2002) used lumped model for naturally ventilated DSF. Balocco (2004) used dimensional analysis to describe the energy performance of different DSF designs and Holmes (1994) developed analytical models for ventilated DSF, which assume a linear vertical temperature gradient.

Tanimoto and Kimura (1997) applied the airflow network model for DSF equipped with venetian blinds. Airflow network models coupled with energy simulation have also been used to evaluate the natural ventilation of office buildings with DSF (Gratia and De Herde, 2004a; Gratia and De Herde, 2004b), and to evaluate the energy performance of office buildings with DSF (Gratia and De Herde, 2004c; Stec and Van Paassen, 2005).

In the control-volume approach only one-dimensional flow in the vertical direction is assumed. The temperature stratification in a ventilated façade is evaluated by dividing the façade into control volumes in the vertical direction and setting the mass flow rate for each control-volume equal to the inlet mass flow rate (Saelens, 2002; Faggembauu et al. 2003a; Faggembauu et al. 2003b).

Detailed studies have also been conducted using CFD and experiment for mechanically ventilated façades (Manz et al. 2004), for naturally ventilated façades (Manz, 2004; Zoller et al. 2002) and for naturally ventilated façades equipped with venetian blinds (Safer et al. 2005).

A.3 Problem statement and methodology

The numerical models used for the investigation of the performance of DSF range from simple analytical models to CFD. Detailed information on the flow field and temperature distribution has been obtained using CFD. The control-volume models are thermal models similar to the non-pressure zonal models used to predict temperature stratification in a room. The problem with control-volume models is that the airflow has to be known a priori and it is not part of the numerical solution. Moreover, the extension of the control-volume models to other shading devices such as venetian blinds is not straight forward, as it requires pressure distribution in the cavity in order to evaluate the airflow in the inner and the outer cavities. Therefore, in order to enhance the prediction capability of the control-volume models for a DSF with venetian blinds, the PLM was applied in this study.

Safer et al. (2004) in their CFD model for a DSF used a simple homogeneous porous media model similar to Equation 4.4 to calculate the airflow rate through the venetian blinds. Moreover, Tanimoto and Kimura (1997) have used power-law relation for calculating the airflow through the blinds using the network approach. The main

difference between the present study and Tanimoto and Kimura (1997) approach is that in the latter the total airflow in the outer and inner cavity is calculated using the power-law equation but the airflow through each blind is approximated as a fraction of the total airflow rate, which is proportional to the distance of the blind from the bottom of the DSF. In this study, the airflow rate through the blinds is directly calculated using the PLM, which is similar to the Safer et al. (2004) approach but the latter used the quadratic model (Equation 4.4). Moreover, the pressure drop for banks of tubes in cross and parallel flow is calculated using an equation similar to the PLM. Therefore, the application of the PLM assumes each slat of the venetian blind as long horizontal cylinder in the ambient fluid except when the venetian blinds are completely closed.

The energy balance equation for DSF includes the absorbed solar radiation, long wave radiation exchange between layers, convective heat transfer between the cavity air and the layers, and conduction in the DSF layers (glass and shading device). Hence, the energy balance for any cell in layer of the DSF system can be given as:

$$m_{Li,j} c_{p,Li} \frac{T_{Li,j}}{dt} = q_{cond,Li,j} + q_{conv,Li,j} + q_{rad,Li,j} + A_{Li,j} \alpha_{Li} q_{sol,Li} \tag{A.1}$$

where

$m_{Li,j}$ is the mass of the glass cell j in layer i, kg;

$c_{p,Li}$ specific heat capacity of layer i, J/kg/k;

$q_{cond,Li,j}$ is the heat transferred due to conduction to cell j in layer i, W;

$q_{conv,Li,j}$ is the heat transferred due to convection to cell j in layer i, W;

$q_{rad,Li,j}$ is the heat transferred due to long wave radiation to cell j in layer i, W;

$q_{sol,Li,j}$ is the total solar radiation flux on cell j in layer i, W/m^2;

$A_{Li,j}$ is the area of cell j in layer i, m^2;

α_{Li} is the absorptance of layer i.

In the following sections the development of the airflow and thermal models for a DSF system and their solution techniques are presented.

A.4 Thermal models for the DSF system

In the zonal approach, the layers are divided into a number of cells and Equation A.1 is then applied for each cell. In this section, the conduction, solar radiation, long wave radiation and convection models for the DSF system in Figure 5.1 are discussed. In order to develop these thermal models, the following assumptions were made:

- Material properties such as specific heat capacity and thermal conductivity are constant and the cavity air is treated as a non-absorbing and non-emitting medium;
- Heat transfer in the lateral direction is negligible: the thermal models for cavity air are two-dimensional;
- The elements are all diffuse-gray surfaces for long wave radiation analysis. This was found to be satisfactory when the enclosure has multiple surfaces (Siegel and Howell, 1992). For diffuse surface, the reflectivity is independent of the outgoing or incoming directions, and the emissivity and absorptivity of a gray surface are independent of the wavelength.

A.4.1 Conduction heat transfer

Since the glass panes are very thin (6mm and 8mm), a one-dimensional conduction in the y-direction was assumed in layers L1, L2, and L4:

$$q_{cond,Li,j} = \frac{A_{Li,j} k_{Li} (T_{Li,j-1} - T_{Li,j})}{\Delta y} \tag{A.2}$$

where

$q_{cond,Li,j}$ is the heat transferred by conduction between two cells, W;

$A_{Li,j}$ is the area of the cell face on layer i, m^2;

k_{Li} is the thermal conductivity for layer i, W/m.K;

$T_{Li,j}$ and $T_{Li,j-1}$ are the temperatures of cells, K.

A.4.2 Radiation heat transfer

Radiation heat transfer occurs due to the energy transported in the form of electromagnetic waves with wavelength between 0.1μm and 1000 μm. This includes the short wave (solar radiation), which has wavelength between 0.3 μm and 2.5 μm; and the long wave (emitted by surfaces at terrestrial temperature) that has wavelength between 5 μm and 50 μm (Duffie and Beckman, 1980).

A.4.2.1 Solar radiation

The total solar radiation reaching on the DSF layers is the sum of the direct solar radiation, the diffuse sky radiation and the solar radiation reflected from the surrounding surfaces:

$$q_{sol} = q_{sol,D} + q_{sol,d} + q_{sol,r} \tag{A.3}$$

Where,

q_{sol} is the total solar radiation reaching on DSF layer, W/m^2;

$q_{sol,D}$ is the direct solar radiation, W/m^2;

$q_{sol,d}$ is the diffuse sky radiation, W/m^2 ;

$q_{sol,r}$ is the solar radiation reflected from the surrounding surfaces, W/m^2.

Solar radiation incident on a DSF system is partly transmitted, reflected and absorbed within the DSF system. The fraction of the incident solar radiation that is reflected is called reflectance (ρ), the fraction transmitted is called transmittance (τ), the fraction absorbed is called absorptance (α). The properties ρ, τ and α of the materials of the DSF are functions of the wavelength and the incident angle. Angle dependent but spectrally (wavelength) averaged values are also used. In this study, values α = 0.1 for all glasses, and α= 0.40 for the venetian blind (which are the optical properties at normal incidence, 0°) were taken from ASHRAE, (2001) since no information on the angular variation was available from the manufacturer. This is reasonable since optical properties such as absorptance change little between 0° and 60^0 and most solar radiation is irradiated in this range. Furthermore, for the DSF with venetian blinds and the slat angle greater than 40°, straight-through transmission of direct solar radiation is completely eliminated and the transmitted diffuse and reflected components remain (ASHRAE, 2001). However, the venetian blind shading device at slat angle equal to 45° shown in Figure 5.1 could not completely eliminate the transmission of direct solar radiation due to the pores on the slats. The diffused and ground reflected solar radiations, which are required for the calculation of the absorbed solar radiation $A_{Li,j}q_{sol}\ \alpha_{Li}$ in Equation A.1, were not measured. Thus, the total solar radiation was used.

A.4.2.2 Long wave radiation

Long wave radiation and convection heat transfer between the surroundings (sky and ground) and room is part of the overall thermal resistance of a fenestration system. The heat transferred due to the combined effect of convection and long wave radiation between the external layer (L1) and the surrounding or the internal layer (L4) and the room can be calculated as follows:

$$q_{Li,j} = Ah_{conv-rad}(T_{eq} - T_{surf}) \tag{A.4}$$

where

T_{eq} is the equivalent temperature, K;

$h_{conv-rad}$ is the surface heat transfer coefficient due to convection and radiation, W/m^{2}K.

The equivalent temperature of the outdoor environment is assumed to be equal to the outdoor air temperature for L1 and the indoor temperature for L4 (ASHRAE, 2001). Many correlations have been proposed which relate the outside surface heat transfer coefficient with wind speed. Since no wind speed measurement was done near the site of the DSF described in section 5.1, a standard value of 29W/m^{2}K, which corresponds to wind speed of 6.7m/s was used (ASHRAE 2001).

At the inner layer, the surface heat transfer coefficient can be calculated as follows (ASHRAE 2001):

$$h_{conv-rad} = 1.48\left(\frac{T_{L4} - T_{indoor}}{H}\right)^{0.25} + \frac{T_{L4}^4 - T_{indoor}^4}{T_{L4} - T_{indoor}} \tag{A.5}$$

where

T_{L4} is the temperature of the inner layer (glass), K;

T_{indoor} is the temperature of the room, K;

H is the height of the DSF, m.

The long wave radiation heat transfer in the DSF is a more complex problem due to its nonlinear behavior and the obstruction of the venetian blinds. Therefore, to determine the long wave exchange between the venetian blinds and the other layers, non-linear surface radiosity balance equations are required. In order to simplify this, the long wave radiation heat transferred to a cell j in layer Li is approximated by (Tanimoto and Kimura, 1997):

$$q_{rad,Li,j} = A_{Li,j} h_{rad,Li,Li+1} (T_{Li+1,j} - T_{Li,j}) \tag{A.6}$$

where

$h_{rad,Li,Li+1}$ is the radiation heat transfer coefficient between surface L_i and L_{i+1}, W/m^2K; which is defined as

$$h_{rad,Li,Li+1} = \frac{4\sigma T_m^3}{\frac{1}{F_{Li,Li+1}} + \frac{1-\varepsilon_{Li}}{\varepsilon_{Li}} + \frac{1-\varepsilon_{Li+1}}{\varepsilon_{Li+1}}} \tag{A.7}$$

where

σ is the Stefan-Boltzmann constant = $5.67 \times 10^{-8} W/m^2.K^4$;

T_m is the mean temperature of the two opposite layers, K;

ε_{Li} and ε_{Li+1} are emissivities of layer L_i and L_{i+1};

$F_{Li,Li+1}$ is the view factor for the two layers.

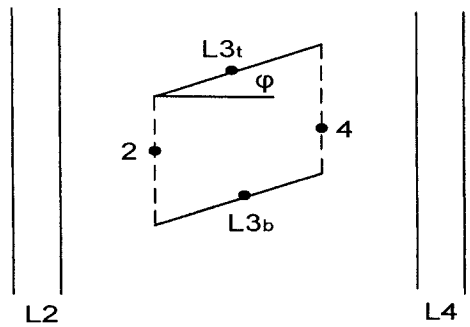

Figure A.2 Fictitious cavity for calculating the view factors for the layers of a DSF.

The view factor $F_{Li,Li+1}$ is calculated by using the fictitious cavity method (Rheault and Bilgen, 1987; Park, 2003). As shown in Figure A.2, the fictitious cavity is the region surrounded by the surfaces $L3_t$, 4, $L3_b$, and 2. For example, in this method the view factor from $L3_t$ to L4 ($F_{L3t,L4}$) is assumed to be $F_{L3t,4}$ since the long wave radiation exchange between surfaces $L3_t$ and L4 is through surface 4. Using the summation and reciprocity rule, the view factors can be calculated as (Park 2003):

$$
\begin{aligned}
F_{L2,L3} &= 2 - \sin\left(\frac{90+\varphi}{2}\right) - \sin\left(\frac{90-\varphi}{2}\right) \\
F_{L2,L4} &= \sqrt{2}\cos\left(\frac{\varphi}{2}\right) - 1 \\
F_{L3,L4} &= F_{L2,L3}
\end{aligned}
\tag{A.8}
$$

where

φ is the angle the slats make with the horizontal.

A.4.3 Convective heat transfer in the cavities

Convective heat transfer between the surfaces of the DSF and the cavity, depending on the position of the glazing in the DSF system, can be evaluated using Equation 3.32. As discussed in Section 3.2, the surface heat transfer coefficient has to be known a priori or determined during the numerical calculation using empirical equations. Like in the case of the room thermal flow, the convective heat transfer coefficients in the cavities can also be estimated using the empirical relations.

For the ventilated cavity and the outside double-glazing, the convective heat transfer coefficients can be estimated by using empirical relations for the average Nusselt number (Nu) for duct, flat plates and narrow cavity. The average heat transfer coefficient is then estimated using the relation:

$$h_{conv} = \frac{Nuk_a}{l_{ch}} \tag{A.9}$$

where

h_{conv} is the average heat transfer coefficient, W/m^{2}K;

k_a is the thermal conductivity of air, W/m.K;

l_{ch} is the characteristic length, which is equal to H, W, or D_h, m.

The hydraulic diameter, D_h is calculated by

$$D_h = \frac{4A_0}{p} \tag{A.10}$$

where

A_0 is the area of the inlet, m^2;

p is the perimeter of the inlet, m.

A.4.3.1 The double pane

Since the cavity in the double pane (L1 and L2) is enclosed, heat transfer is only due to natural convection. The *Nu* for an enclosed cavity is given as function of the aspect ratio (A_{ratio}), Grashof number (*Gr*), Prandtl number (*Pr*) and Rayleigh number (*Ra*), which are defined as:

$$A_{ratio} = \frac{H}{W} \tag{A.11}$$

$$Gr = \frac{g l_{ch}^3 \beta \Delta T}{\nu^2} \tag{A.12}$$

$$\Pr = \frac{\nu}{\alpha} \tag{A.13}$$

$$Ra = \Pr Gr \tag{A.14}$$

where

Pr = 0.72 for air;

H is the height of the cavity, m;

W is the width of the cavity, m;

β is the thermal expansion coefficient, 1/K;

ΔT is the temperature difference between the cavity layers, K;

ν is the kinematic viscosity, m^2/s;

α is the thermal diffusivity, m^2/s.

Characteristic length, which can be cavity height (H), cavity width (W) or hydraulic diameter (D_h), is commonly used as a subscript to the dimensionless numbers in order to show the basis of the calculation. The average Nusselt number for enclosed cavity is given in Table A.1.

Table A.1 Average Nusselt number for the outer double pane cavity.

$2 < A_{ratio} < 10$ (Bejan , 1995)	$A_{ratio} > 40$ (Wright, 1996)
$Nu_H = 0.22\left(\frac{\Pr}{0.2+\Pr}Ra_H\right)^{0.28}\left(\frac{1}{A_{ratio}}\right)^{0.09}$	$5x10^4 < Ra_W \leq 10^6 : \; Nu_W = 0.0673838 Ra_W^{0.3}$
	$10^4 < Ra_W \leq 5x10^4 : Nu_W = 0.028154 Ra_W^{0.4134}$
$\Pr < 10^5, Ra < 10^{13}$	$Ra_W \leq 10^4 : Nu_W = 1 + 1.75967x10^{-10} Ra_W^{2.2984755}$

A.4.3.2 The ventilated cavities

DSF cavities can be ventilated mechanically as part of HVAC system or naturally (wind and buoyancy). Therefore, different expressions describing the convective heat transfer are used. The case described in section 5.1 is for a mechanically ventilated façade. But mixed convection is also possible depending on the ratio of Gr/Re^2. Natural convection can be assisted or opposed by forced convection and vice versa. Natural convection dominates the forced convection when Gr/Re^2 >1000 (Hamadah and Wirtz, 1991). In such cases the reverse flow makes heat removal from the DSF difficult.

1. Mechanically ventilated cavities

For the mechanically ventilated outer and inner cavities, the general relation for the average Nusselt number for forced convection in ducts and vertical plates can be used. The *Nu* for flow in ducts and parallel plates, and external flow on a vertical plate, is a function of the *Pr* and the *Re*. The *Re* and the entrance length are used to divide the flow into entrance region, fully developed laminar, transition and turbulent flow. The transition between the laminar and turbulent region in internal flow starts at $Re = 2000$ and turbulence starts from $Re = 2300$. For flow over a plate, the critical $Re = 5\text{x}10^5$ and the transition between laminar and turbulent flow is $2\text{x}10^4 < \text{Re} < 10^6$ (Bejan, 1995). For the entrance region, heat transfer coefficient correlations for a vertical plate can be used. Table A.2 lists the correlations used for mechanically ventilated cavities.

2. Naturally ventilated cavities

For the evaluation of heat transfer coefficient in naturally ventilated facades, the cavity can be distinguished as a wide or narrow cavity. In the former, the boundary layers are very small compared to the width of the cavity. In the latter, the boundary layers at the two sides interfere and the velocity profiles merge. A cavity is called wide if it satisfies the following inequality (Bejan, 1995):

$$\frac{W}{H} > Ra_H^{-1/4} \tag{A.15}$$

where

Ra_H is the Rayleigh number based of the height (H) of the cavity.

Table A.2 Average Nusselt number correlations used for mechanically ventilated cavities (Bejan, 1995).

	Entrance length	Fully developed Laminar	Fully developed Turbulent
Flow length	$\frac{y_f}{D_h} \approx 0.05\,\mathrm{Re}$	$\frac{y_f}{D_h} \leq 0.05\,\mathrm{Re}$	$\frac{y_f}{D_h} \approx 10$
Thermal length	$\frac{y_t}{D_h} \approx 0.05\,\mathrm{Re}\,\mathrm{Pr}$	$\frac{y_t}{D_h} \leq 0.05\,\mathrm{Re}\,\mathrm{Pr}$	$\frac{y_t}{D_h} \approx 10$
Uniform temperature	$Nu = 0.664\,\mathrm{Re}^{1/2}\,\mathrm{Pr}^{1/3}$	$Nu = 7.54$	$Nu = 0.023\,\mathrm{Re}^{4/5}\,\mathrm{Pr}^{1/n}$ n = 0.3 when the fluid is cooled and n = 0.4 when the fluid is heated
Uniform heat flux	$Nu = 0.906\,\mathrm{Re}^{1/2}\,\mathrm{Pr}^{1/3}$	$Nu = 8.235$	

When Equation 5.15 holds, which is true for the case described in Section 5.1, the heat transfer coefficient can be calculated using single vertical plate formula for air for laminar and turbulent flow (Churchill and Chu, 1975a):

$$Nu_H = (0.825 + cRa_H^{1/6})^2 \qquad 0.1 < Ra_H < 10^{12} \tag{A.16}$$

Where the constant c is equal to 0.325 for uniform temperature and 0.328 for uniform heat flux.

A.4.3.3 Estimated heat transfer coefficients

For the double-pane cavity, the average *Nu* is very close to 1.0 for both cases. This is because the double pane cavity is narrow and the temperature difference between L1 and L2 is very small making *Gr* very small (Equation A.12). This indicates that the heat transfer through the double pane cavity is by conduction. For the ventilated cavities, the ratio Gr/Re^2 is in the order of 10 at L2 and L4 showing that mixed convection prevailed (Hamadah and Wirtz, 1991). The heat transfer coefficients for the natural and forced convection were evaluated as follows:

- Forced convection. $Re_{Dh} = 923 < 2300$ and $Re_H = 1.6\text{x}10^4 < 5\text{x}10^5$ (laminar). From the equations in Table A.2, $y_f = 6.46$m, and $y_t = 4.65$m, which are greater than the height of the DSF (H = 2.5m). Therefore, the laminar vertical plate correlation in Table A.2 can be used for L2 and L4.
- Natural convection. Equation A.15 holds and the heat transfer coefficients were calculated at L2, L3 and L4 using Equation A.16.

The effective heat transfer coefficients were then estimated using:

$$Nu = (Nu_{nat}{}^3 + Nu_{mec}{}^3)^{1/3} \qquad \text{(A.17)}$$

where

Nu_{nat} is the Nusselt number for natural convection;

Nu_{mec} is the Nusselt number for forced convection.

Equation A.17 gives the heat transfer coefficient of 2.2 W/m^{2}K at L2 and 1.5 W/m^{2}K at L4.

A.5 Airflow and energy equations for venetian blinds

The airflow in the outer double-pane cavity was not calculated since the heat transfer between the two panes is by conduction (*Nu* is close to 1.0). For the airflow in the outer cavity (Ca1) and inner cavity (Ca2), the PLM was directly employed. It was mentioned earlier that in this study, the airflow rate through the blinds is calculated using the PLM. In doing so it is assumed that each slat of the venetian blind acts as long horizontal cylinder in the ambient fluid except when the venetian blind is completely closed. When the venetian blind is open, the permeability of the venetian blind, which can be defined as the ratio between the unshaded area and the total area between the slats, can be expressed as (Pfrommer et al. 1996):

$$p = 1 - \left|\cos\varphi \tan\beta - \sin\varphi\right| \tag{A.18}$$

where

p is the permeability of the venetian blinds;

β is the solar altitude.

φ is the angle the slats make with the horizontal.

Since a cell in the shading device (L3) contains both air and one or more blind slats, the absorbed radiation is only associated to the slats. Equation A.1 becomes

$$m_{Li,j} c_{p,Li} \frac{T_{Li,j}}{dt} = q_{conv,Li,j} + q_{rad,Li,j} + (1-p) A_{Li,j} \alpha_{Li} q_{sol,Li} \tag{A.19}$$

Since φ = 45 and using the optical properties at normal incidence θ = 0 and β = 0, Equation A.18 gives p = 0.3. To calculate the heat transfer coefficient for either side of the blind slats, the convective heat transfer between the cavity air and the slats was

estimated by assuming the slats as cylinders in cross flow since both sides of the slats are heated or cooled. Hence, the average Nusselt numbers for natural and forced convection can be given as (Churchill and Chu, 1975b):

$$Nu_D = (0.60 + 0.322 Ra_D^{1/6})^2 \qquad 0.1 < \mathrm{Ra_D} < 10^{12} \tag{A.20}$$

$$Nu_D = 0.51 \mathrm{Re}_D^{0..5}\, \mathrm{Pr}^{0.37} \qquad 40 < \mathrm{Re_D} < 10^3 \tag{A.21}$$

Since the ratio Gr/Re^2 is in the order of 10, the heat transfer is due to mixed convection (Hamadah and Wirtz, 1991). The effective heat transfer coefficient estimated using Equation A.17 is 4.7 W/m^2K.

A.6 Solution of airflow and energy equations

The system of equations involving Equation A.1 were solved, couple with the system of energy balance and the airflow equations for each cells in the cavities using the solution technique described in Section 3.3. The input parameters for all the simulations, pertaining to the case described in Section 5.1, were: the façade geometry, the material properties, the measured average indoor temperature, the measured inlet temperature, the measured inlet airflow rate, the measured outdoor temperature, the measured total solar radiation incident on surfaces, and the estimated convective heat transfer coefficients.

REFERENCES

AirPak. 2002. Fluent Inc., NH, USA.

Alamdari, F., and Hammond, G.P. 1983. Improved data correlations for buoyancy-driven convection in rooms. *Building Services Engineering Research and Technology* 4(3): 106–12.

Arnold P.D., Hammond G.P., Irving A.D., and Martin C.J. 1998. The influence of sun patches on buoyancy-driven air movement and heat transfer within a passive solar test cell. *Proceedings of ASME Heat Transfer Division*, 361(1), 47-57.

ASHRAE 2001. Fundamentals, American Society of Heating, Refrigeration and Air-conditioning Engineers, Atlanta, GA.

Awbi, H. 2003. Ventilation of buildings, 2nd Ed., Taylor & Francis, London.

Awbi, H.B., and Hatton, A. 2000. Mixed convection from heated room surfaces. *Energy and Buildings* 32:153–66.

Axley, J.W. 2001. Surface-drag flow relations for zonal modeling. *Building and Environment* 36:843-850.

Balocco, C. 2002. Simple model to study ventilated facades energy performance. *Energy and Buildings* 34: 469-475.

Balocco, C. 2004. A non-dimensional analysis of a ventilated double façade energy performance. *Energy and Buildings* 36: 35-40.

Beausoleil-Morrison, I. 2000. The adaptive coupling of heat and air flow modelling within dynamic whole-building simulation. PhD thesis, University of Strathclyde, Glasgow, UK.

Bejan, A. 1995. Convection heat transfer 2nd edition. J. Wiley, New York.

Chen, Q. 1996. Prediction of room air motion by Reynolds-stress models. *Building and Environment* 31(3): 233-244.

Chen, Q., and Moser, A. 1991. Simulation of a multiple nozzle diffuser. *Proceedings of the Twelfth AIVC Conference*, Ottawa, Canada, 2: 1-14.

Chen, Q., and Xu, W. 1998. A zero-equation turbulence model for indoor air simulation. *Energy and Buildings* 28:137-144.

Chiu, Y.H., and Etheridge, D.W. 2002. Calculation and notes on the quadratic and power-law equations for modeling infiltration. *International journal of ventilation* 1(1): 65 -77.

Churchill, S.W., and Chu, H.H.S. 1975a. Correlating equations for laminar and turbulent free convection from a vertical plate. International journal of heat and mass transfer 18 (11): 1323-1329.

Churchill, S.W., and Chu, H.H.S. 1975b. Correlating equations for laminar and turbulent free convection from a horizontal cylinder. International journal of heat and mass transfer 18 (9): 1149-1053.

Clifford, M.J., Everitt, P.J., Clarke, R., and Riffat, S.B. 1997. Using computational fluid dynamics as a design tool for naturally ventilated buildings. *Building and Environment* 32 (4): 305-312.

Cocora, O. 1996. Study of heat and mass transfer within closed space. Prediction of air movement in ventilated rooms. *Ph.D. thesis*, Technical University of Construction, Bucharest.

Djunaedy, E., and Cheong, K.W.D. 2002. Development of simplified technique of modeling four-way ceiling air supply diffuser. *Building and Environment* 37(4): 393-403.

Dols, W.S., and Walton, G.N. 2002. CONTAMW 2.0 user manual. National institute of science and technology (NIST), Technology administration, *US department of commerce*.

Duffie, J.A., and Beckman, W.A. 1980. Solar engineering of thermal processes. Wiley, New York.

Etheridge, D.W. 1998. A note on crack flow equations for ventilation modeling. B*uilding and Environment* 33: 325-328.

Etheridge, D.W. 2004. Natural ventilation through large openings – measurements at model scale and envelope flow theory. *International journal of ventilation* 2(4): 325 – 342.

Faggembauu, D., Costa, M., Soria, M., and Oliva, A. 2003a. Numerical analysis of the thermal behavior of ventilated facades in Mediterranean climates Part I: development and validation of a numerical model. *Solar Energy* 75: 217-228.

Faggembauu, D., Costa, M., Soria, M., and Oliva, A. 2003b. Numerical analysis of the thermal behavior of ventilated facades in Mediterranean climates Part II: application and analysis of results. *Solar Energy* 75: 229-239.

Feustel, H.E., and Dieris, J. 1992. A survey on airflow models for multizone structures. *Energy and buildings* 18: 79-100.

Feustel, H.E., and Smith, B. 1997. COMIS 3.0 user guide, *Lawrence Berkeley Laboratory (LBL)*, Berkeley, California, USA.

Fisher, D.E. 1995. An experimental investigation of mixed convection convection heat transfer in a rectangular enclosure. *PhD Thesis*, University of Illinois, Urbana USA.

Fluent. 2003. Fluent users guide, version 6.1, Fluent Inc., NH, USA.

Gagneau, S., and Allard, F. 2001. About the construction of autonomous zonal models. *Energy and Buildings* 33: 245-250.

Gharbi, N., Ghrab-Morcos, N., and Roux, J.J. 2004. ZAER: a zonal model for heat transfer and airflow in unconditioned buildings – an experimental validation. *International Journal of ventilation* 3(1): 11-20.

Gratia, E., and De Herde, A. 2004a. Natural ventilation in a double-skin façade. *Energy and Buildings* 36:137-146.

Gratia, E., and De Herde, A. 2004b. Optimal operation of a south double-skin façade. *Energy and Buildings* 36: 41-60.

Gratia, E., and De Herde, A. 2004c. Is day natural ventilation still possible in office buildings with a double-skin façade? *Building and Environment* 39: 399-409.

Griffith, B., and Chen, Q. 2003. A Momentum-Zonal Model for Predicting Zone Airflow and Temperature Distributions to Enhance Building Load and Energy Simulations. *HVAC&R Research* 9(3): 309 – 325.

Gschwind, M., Bezian, J.J., Hasebe, T., Fonzes, G., Fujita, S., Loiseau, P., and Takeda, I. 1996. A zonal model to simulate a room heated by gas heat pump (GHP) BTHEBES. *ROOMVENT'* 96, 1:61-68.

Haddad, K.H., and Elmahdy, A.H. 1998. Comparison of the monthly thermal performance of a conventional window and a supply-air window. *ASHRAE Transactions*, 1261-1270.

Haghighat, F.1989. Air infiltration and indoor air quality models- a review. *International journal of ambient energy* 10:115-122.

Haghighat, F. Jiang, J., Wang, JCY. and Allard, F. 1992. Air movement in building using computational fluid dynamics. *Transactions of ASME Journal of Solar Energy Engineering* 114: 84-92.

Haghighat, F., Li, Y., and Megri, A.C. 2001. Development and validation of a zonal model- POMA. *Building and Environment* 36: 1039-1047.

Hamadah, T.T., and Wirtz, R.A. 1991. Analysis of laminar fully developed mixed convection in a vertical channel with opposing buoyancy. *ASME Journal of heat transfer* 113: 507-510.

Hanqing, W., Chunhua, H., Zhiqianq, L., Guangfa, T., Yingyun, L., and Zhiyong, W. 2005. Dynamic evaluation of thermal comfort environment of air-conditioned buildings. *Building and Environment*, in press.

Heine, O., and Mogens, S.T. 1990. Calculation of vertical temperature gradient in heated rooms. *ROOMVENT* '90, B1.25.

Heikkinen, J. 1991. Modeling of a supply air terminal for room airflow simulation. *Proceedings of the Twelfth AIVC Conference*, Ottawa, Canada, 213-230.

Holmes, M.J., 1994. Optimization of the thermal performance of mechanically and naturally ventilated glazed facades. *Renewable Energy* 5:1091-1098.

Howarth, A.T. 1980. Temperature distributions and air movements in rooms with a convective heat source. *Ph.D. Thesis*, University of Manchester. UK.

Huang, H. 2003. Modeling of volatile organic compounds emissions and sinks from building materials. *Ph.D. Thesis*, Concordia University, Canada.

Huang, H., Haghighat F., and Wurtz E. 2002. An integrated zonal model for predicting transient VOC distribution in ventilated room. *Proceedings of Esim* 2002, Montreal, Canada, 78-83.

Huo, Y., Haghighat, F., Zhang, J.S., and Shaw, C.Y. 2000. A systematic approach to describe the air terminal device in CFD simulation for room air distribution analysis. *Building and Environment* 35:563-576.

Inard, C., Bouia, H., and Dalicieux, P. 1996a. Prediction of air temperature distribution in buildings with a zonal model. *Energy and Buildings* 24:125-132.

Inard, C., and During, H. 1994. Energy consumption and thermal comfort in buildings: an approach with zonal models. *ROOMVENT* '94, 2:131-146.

Inard, C., Meslem, A., and Depecker, P. 1996b. Use of zonal model for the prediction of air temperature distribution in large enclosures. *ROOMVENT* '96, 2:177-184.

Inard, C., Meslem, A., and Depecker, P. 1997. Energy consumption and thermal comfort in dwelling-cells: a zonal model approach. *Building and Environment* 33:279-291.

Jiang, Y., and Chen, Q. 2001. Study of natural ventilation in buildings by large eddy simulation. *Journal of wind engineering and Industrial aerodynamics* 89:1155-1178.

Jiang, Y., and Chen, Q. 2002. Effect of fluctuating wind direction on cross natural ventilation in buildings from large eddy simulation. *Building and environment* 37:379-386.

Jiang,Y., Allocca, C., and Chen, Q. 2004. Validation of CFD Simulations for Natural Ventilation. *International journal of ventilation* 2(4): 359-370.

Kato, S. 2004. Flow network model based on power balance as applied to cross-ventilation. *International journal of ventilation* 2(4): 395 – 408.

Manz, H. 2004. Total solar energy transmittance of glass double facades with free convection. *Energy and Buildings* 36: 127-136.

Manz, H., Schaelin, A., and Simmler, H. 2004. Airflow patterns and thermal behavior of mechanically ventilated glass facades. *Building and Environment* 39: 1023-1033.

Manzoni, D. and Rongere, F.X. 1996. Simplified models of displacement ventilation systems. ROOMVENT '96, 2:443-448.

Megri A.C., Snyder M., and Musy, M. 2005. Building zonal thermal and airflow modeling – a review. *International journal of ventilation* 4(2):177 – 188.

Mendoca, K.C., Inard, C., Wurtz, E., and Winkelmann, F.C. 2002. A zonal model for predicting simultaneous heat and moisture transfer in buildings. Proceedings of Indoor air 2002.

Mora, L., Gadgil, J., and Wurtz, E. 2003. Comparing zonal and CFD model predictions of isothermal indoor airflows to experimental data. *Indoor air* 13:77-85.

Mora, L., Inard, C., Wurtz, E., and Axley, J.W. 2002. Prediction of indoor environmental quality in multizone buildings using zonal models. *Roomvent* 2002.

Musy, M., Winkelmann, F., Wurtz, E., and Sergent, A. 2002. Automatically generated zonal models for building airflow simulation: principles and application. *Building and Environment* 37: 873-881

Musy, M., Wurtz, E., Winkelmann, F., and Allard, F. 2001. Generation of a zonal model to simulate natural convection in a room with a radiative/convective heater. *Building and Environment* 36:589-596.

Nielsen, J.R.1998. The influence of office furniture on the air movements in a mixing ventilation room. *Ph.D Thesis*, Aalborg University, Denmark.

Nielsen, P.V. 1990. Specification of a two-dimensional test case. *IEA Annex 20 Report*, Aalborg University, Denmark.

Nielsen, P.V. 2004. Computational fluid dynamics in the indoor environment, new developments and quality considerations. *Proceedings of CIB* 2004, 783-791.

Oesterle, E. 2001. Double-skin facades – integrated planning. Prestel Verlag, Munich, Germany.

Park, C.S. 2003. Occupant responsive optimal control of smart façade systems. *Ph.D Thesis*, Georgia Institute of Technology, Georgia, USA.

Park, C.S., Augenbroe, G., Messadi, T., Thitisawat, M., and Sadegh, N. 2004a. Calibration of a lumped simulation model for double-skin façade system. *Energy and Buildings* 36: 1117-1130.

Park, C.S., Augenbroe, G., Sadegh, N., Thitisawat, M., and Messadi, T. 2004b. Real-time optimization of a double-skin façade based on lumped modeling and occupant preference. *Building and Environment* 39: 939 – 948.

Pfrommer, P., Lomas, K. J., and Kupke, C. 1996. Solar Radiation Transport through slat-type blinds: A new model and its application for thermal simulation of buildings. *Solar Energy* 57 (2): 77-91.

Press, W.H., Teukolsky, S.A. Vetterling, W.T., and Flannery, B.P. 1996. Numerical recipes in Fortran 90: the art of parallel scientific computing. Cambridge university press, Cambridge, UK.

Ren, Z. 2002. Enhanced modeling of indoor airflows, temperatures, pollutant emission and dispersion by nesting sub-zones within a multizone model. *PhD Thesis*, the Queen's University of Belfast, UK.

Ren, Z., and Stewart, J. 2003. Simulating airflow and temperature distribution inside buildings using a modified version of COMIS with sub-zonal divisions. *Energy and Buildings* 35:257-271.

Ren, Z., and Stewart, J. 2005. Prediction of personal exposure to contaminant sources in industrial buildings using a sub-zonal model. *Environmental modeling and software* 20 (5): 623-638.

Rheault, S., and Bilgen, E.1987. Heat Transfer Optimization of An Automated Venetian Blind Window System. *ASES 12th National Passive Solar Conference*, Portland, Oregon, 122-128.

Saelens, D. 2002. Energy Performance Assessment of Single Storey Multiple-Skin Facades. *Ph.D. Thesis*, Katholieke Universiteit Leuven, Leuven, Belgium.

Sandberg, M. 2004. An alternative view on the theory of cross-ventilation. *International journal of ventilation* 2(4): 409 – 418.

Safer, N., woloszyn, M., and Roux. JJ. 2005. Three-dimensional simulation with a CFD tool of the airflow phenomena in single floor double-skin façade equipped with venetian blind. *Solar Energy* 79: 193-203.

Shilkrot, E.O., and Zhivov, A.M. 1996. Zonal model for displacement ventilation design. *Roomvent 96* 2: 449-458.

Siegel, R., and Howell, J.R. 1992. Thermal Radiation Heat Transfer, 3rd Ed.,Hemisphere Publishing Corporation.

Stec, W.J., and Van Paassen, A.H.C. 2005. Symbiosis of the double-skin façade with the HVAC system. *Energy and Buildings* 37:461-469.

Stewart, J., and Ren, Z. 2003. Prediction of indoor gaseous pollutant dispersion by nesting sub-zones within a multi-zone model. *Building and environment* 38:635-643.

Stewart, J., and Ren, Z. 2005. COwZ—A subzonal indoor airflow, temperature and contaminant dispersion model. *Building and environment*, in press.

Tanimoto, J., and Kimura, K .1997. Simulation study on an airflow window system with an integrated roll screen. *Energy and Buildings* 26: 317-325.

Tannehill, J.C., Anderson, D.A., and Pletcher, R.H.1997. Computational Fluid mechanics and Heat Transfer. Second Edition. Series in Computational and Physical Processes in Mechanics and Thermal Sciences. Tayler and Frencis.

Teshome, E.J., and Haghighat, F. 2004. Zonal models for indoor airflow – a critical review. *International journal of ventilation* 3(2):119 –129.

Tian, Z.F., Tu, J.Y., Yeoh, G.H., and Yuen, R.K.K. 2005. On the numerical study of contaminant particle concentration in indoor airflow. *Building and Environment,* in press.

Togari, S., Arai, Y., and Miura, K. 1993. A simplified model for predicting vertical temperature distribution in large space. *ASHRAE Transactions* 99(1): 88-99.

Topp, C. 1999. Diffusion and evaporation-controlled emission in ventilated rooms. Ph.D. thesis, Aalborg University, Denmark

Topp, C., and Nielsen, P.V. and Heiselberg, P.2001. Influence of the local air flow on pollutant emission from indoor building surfaces. *Indoor air* 11(3): 162-170.

Versteeg, H.K., and Malalasekera, W. 1995. An introduction to computational fluid dynamics: the finite volume method. Longman Group Ltd.

Voeltzel, A., Carrie, F.R., and Guarracino G. 2001. Thermal and ventilation modeling of large highly glazed spaces. *Energy and Buildings* 33:121-132.

Von Grabe, J. 2002. A prediction tool for the temperature field of double facades. *Energy and Buildings* 34: 891-899.

White, F.M. 1991. Viscous fluid flow, McGraw-Hill series in mechanical engineering, New York.

Wright, J.L. 1996. A correlation to quantify convective heat transfer between vertical window glazings, ASHRAE Transactions 106: 940–946.

Wurtz, W., Musy, M., and Mora, L. 1999a. Introduction of specific laws in zonal model to describe temperature fields and airflow patters in mixed ventilated buildings. *Journal of the Human-Environment system* 3(1):43-59.

Wurtz, W., Nataf, J.M., and Winkelmann, F. 1999b. Two-and three-dimensional natural and mixed convection simulation using modular zonal models in building. *Int. J. Heat and mass transfer* 42: 923-940.

Xue, H., and Shu, C. 1998. Mixing characteristics in a ventilated room with non-isothermal ceiling air supply. *Building and environment* 34(3):245-251.

Zhang, Y. 2004. Indoor air quality engineering, CRC press LLC, Florida.

Zhang, J.S.1991. A fundamental study of two-dimensional room ventilation flows under isothermal and non-isothermal conditions. *PhD Thesis*, University of Illinois, Urbana USA.

Zhang, J.S., Wu, G.J., Chirstianson, L.L, Riskowski, G.L. 1992. Detailed measurements of room air distribution for evaluating numerical simulation models. *Transactions of ASHRAE* 98(2): 58-65.

Zhang, Y., and Haghighat, F.1997. The impact of surface air movement on material emission. *Building and Environment* 32(6): 551-556.

Zhao, L. 2000. Measurement and analysis of full-scale room airflow using particle image velocimetry (PIV) technique. *PhD Thesis*, University of Illinois, Urbana USA.

Zoller, A., Winter, E.R.F., and Viskanta, R. 2002. Experimental studies of combined heat transfer in turbulent mixed convection fluid flows in double-skin facades. *International Journal of Heat and Mass Transfer* 45: 4401-4408.